SANDIA REPORT

SAND93—0731 • UC—706
Unlimited Release
Printed March 1993

Spaceborne SAR Study: LDRD '92 Final Report

D. L. Bickel, B. C. Brock, C. T. Allen

Prepared by
Sandia National Laboratories
Albuquerque, New Mexico 87185 and Livermore, California 94550
for the United States Department of Energy
under Contract DE-AC04-76DP00789

Issued by Sandia National Laboratories, operated for the United States Department of Energy by Sandia Corporation.

Available to DOE and DOE contractors from
Office of Scientific and Technical Information
PO Box 62
Oak Ridge, TN 37831

Prices available from (615) 576-8401, FTS 626-8401

Available to the public from
National Technical Information Service
US Department of Commerce
5285 Port Royal Rd
Springfield, VA 22161

NTIS price codes
Printed copy: A06
Microfiche copy: A01

SAND93-0731
Unlimited Release
March 1993

Distribution
Category UC-706

Spaceborne SAR Study: LDRD '92 Final Report

D. L. Bickel
Radar Analysis Department
Sandia National Laboratories
Albuquerque, New Mexico 87185

B. C. Brock
Antenna Development Department
Sandia National Laboratories
Albuquerque, New Mexico 87185

C. T. Allen
Radar & Antenna Engineering & Manufacturing
Allied Signal Aerospace Company
Kansas City Division
Kansas City, Missouri 64141

ABSTRACT (U)

This is the final report for a study performed for the 1992 LDRD spaceborne SAR (Synthetic Aperture Radar) study. This report presents an overview of some of the issues that must be considered for design and implementation of a SAR on a spaceborne platform. The issues addressed in this report include: a survey of past, present, and future spaceborne SARs; pulse-repetition frequency (PRF); general image processing issues; transmitter power requirements; the ionosphere; antennas; two case studies; and an appendix with a simplified presentation on geometry and orbits.

This work performed at Sandia National Laboratories supported by the U. S. Department of Energy under contract DE-AC04-76DP00789.

This page intentionally left blank.

TABLE OF CONTENTS

1.0 Objective

The purpose of this report is to document the findings of the first year of the "Spaceborne SAR Study" LDRD. The objective of the study from is "...to understand spaceborne synthetic aperture radar (SAR) experimental and system-critical performance requirements, and to demonstrate a match of these requirements with technologies and capabilities that are unique to SNL." [30].

Reference [30] presents some of the topics to be investigated in the LDRD. This report describes a general study performed as a part of the LDRD which addresses many of these areas. It also outlines other important issues that were not studied and proposes follow-on work. It should be pointed out that this study is not the only result of the FY92 LDRD on spaceborne SAR. There were other specific studies conducted for other government agencies that are not included in this document.

SNL has a broad technology base including experience in designing and building experimental airborne SARs. It is felt that some of these technologies and experience would be valuable for future spaceborne SAR applications. This report attempts to point out many of the issues that are important for spaceborne SAR and how designing a spaceborne SAR is different than designing an airborne SAR.

2.0 Issues Considered

This report is organized as follows:

1) Section 1.0 gives the objective.

2) Section 2.0 are the issues considered in this report.

3) Section 3.0 gives a brief overview of the findings of the report.

4) Section 4.0 presents the results of a literature search concerning past, present, and future spaceborne SARs and trends in areas important to spaceborne SAR. This section also includes a list of spaceborne SAR articles.

5) Section 5.0 discusses general spaceborne SAR issues. These include PRF issues, general image processing issues, power requirements, the ionosphere, and antenna design issues.

6) Section 6.0 presents brief case studies investigating P-band and Ku-band SAR designs.

7) Section 7.0 is the summary.

8) Section 8.0 presents recommendations for future studies.

9) Section 9.0 is the bibliography of references used in this report.

10) Appendix A is a brief presentation of space geometry and orbits issues.

11) Appendix B is a table of symbols used in this report.

3.0 Overview

An overview of the findings of this report are summarized in this section. The basic finding is that designing and building a synthetic aperture radar (SAR) for spaceborne application has some significant differences when compared with airborne SAR. Some of those differences include:

1) PRF requirements are more stringent for spaceborne SAR and are often a limiting factor in the system design. PRF considerations limit the ratio of the range swath width to azimuth resolution. The causes of the PRF problem are higher platform velocities (roughly 50-150 times higher) and longer ranges to the target (roughly 50 times). Techniques to increase the range swath to azimuth resolution ratio involve much more complicated antenna and signal processing design. Techniques such as presumming are not practical in spaceborne SAR.

2) Average power requirements are higher than airborne SAR due to the much longer ranges. Current modest resolution (roughly 20 m) systems have an average transmitter power of 50-100 W and a peak power of 1-5 kW. There are a lot of trade-offs in power requirements but to a first order: a) power increases with increasing frequency for a fixed swath width; b) it increases roughly as the cube of altitude for a given look angle; c) it increases with look angle; d) it increases with required sensitivity; e) it decreases as the reciprocal of resolution (i.e., less power for coarser-resolution) for a distributed target; and f) it increases as roughly the square of the ground range swath width.

3) Reliability is a critical issue, due to the more severe environment and the essentially impossible task of repairing the SAR once it is in orbit.

4) Costs are much higher for spaceborne SARs than for somewhat equivalent airborne SARs. Weight concerns are very important since weight relates directly to cost. The higher the weight, the higher the launch costs. Also, increased power translates to increased weight in terms of solar collectors, batteries, and associated structure.

5) The processing of images is potentially different than for airborne SAR. Range processing is constrained by higher swath-time to pulse-length ratios. Azimuth processing must take into account a Doppler component due to the motion of the earth. This component changes with orbit location in a predictable manner. The Doppler is also affected by attitude errors and target elevation changes. Consideration should be given to the the trade-offs involved in patch versus line-by-line azimuth processing, as well as to the influence of the circular geometry. The motion environment is more stable, but it is still unclear what is required to estimate the satellite motion.

6) The ionosphere is a significant problem for low frequencies and wide bandwidth (fine range resolution). It also affects polarization significantly at low frequencies and large look angles.

7) The antenna is one of the most critical parts of the spaceborne SAR design. Antenna design becomes more complicated for space. Space antennas are larger and must transmit more power. These factors, along with techniques suggested in section 5.2, complicate the electrical design of the antenna array. Besides the electrical issues, there are many more mechanical issues to be concerned with, such as flatness of the antenna for higher frequencies, folding and deployment, the space environment including meteorites, etc.

8) Even though integration times for a given resolution are comparable to those for airborne SAR, the higher PRF and larger swaths for spaceborne SAR means much more data must be transmitted and/or processed in any given period of time.

The following sections of this report justify the comments made in this section.

4.0 Literature Search

This section describes information and trends found in current literature concerning spaceborne SAR missions and issues.

4.1 Past, Present, and Future Spaceborne SAR Systems

In this section the typical technologies, and parameters being used in past, current, and planned spaceborne SAR systems are discussed. Table 4.1.1 gives a listing of these systems and their parameters. Table 4.1.1a shows past systems, 4.1.1b shows systems currently operating, and 4.1.1c shows systems being planned.

There are a few general trends to note from these tables. All of these systems are for remote sensing of the earth and the environment. In these cases, very fine resolution is not as critical as large area coverage. Data collected from SEASAT and ERS-1 are capable of being processed to approximately 5 m resolution in azimuth, but are more typically processed using multilook to around 20-25m resolution. Swath sizes are 50 to 100 km. One of the planened modes of operation of RADARSAT will use very coarse resolution (100 m) along with the ScanSAR technique to achieve up to 500 km swath [56].

SIR-A, SIR-B, and JERS-1 have all borrowed from the design of SEASAT, so L-band is a popular frequency . The choice of L-band for SEASAT was made for three reasons: first, it required less spacecraft DC power for the required 100km swath than for higher frequencies (see section 5.4.4 for explanation); second, affordable solid-state amplifiers were available for L-band, whereas, higher frequencies required TWTs; and third, antenna stabilization tolerances were easily achievable at this lower frequency [62]. The Almaz satellite operates at S-band. Both ERS-1 and the planned RADARSAT are at C-band. In addition, SIR-C will have both L-band and C-band instruments. Also, the Germans supplied an X-band system. The apparent direction of the future satellite SAR missions is towards multiple frequencies and polarizations if they are affordable.

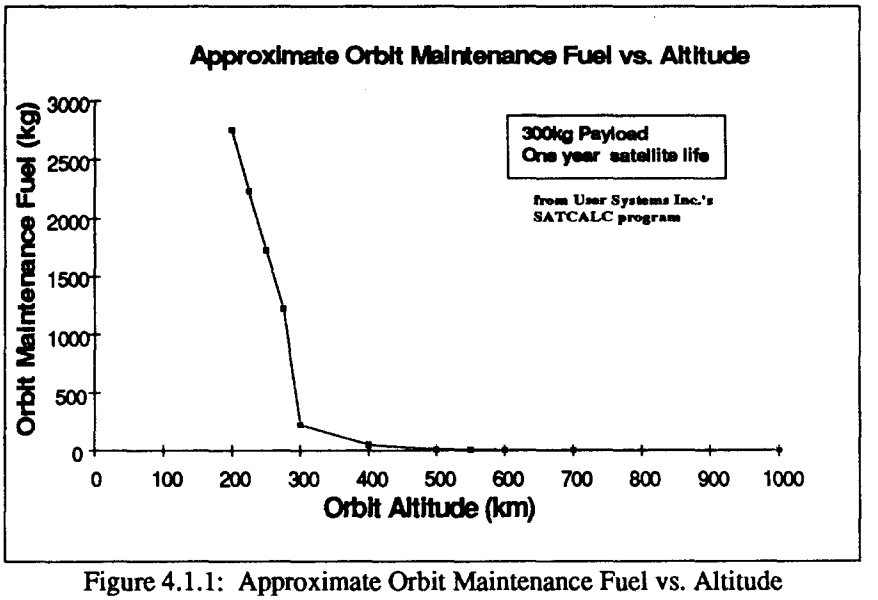

Figure 4.1.1: Approximate Orbit Maintenance Fuel vs. Altitude

Typical orbital altitudes range from 200 to 800 km. Satellites altitudes between 200 and 1000 km are considered to be low-earth orbit (LEO) satellites. The reason for the low orbit is to keep the radar transmitter power requirements (which vary as the cube of the range to the target) low. Except for

Table 4.1.1a: SPACE-BASED SAR SYSTEMS - PAST

PARAMETER	UNITS	SEASAT	SIR-A	SIR-B
Launch date		06/27/78[66]	11/12/81[66]	10/05/84[66]
Altitude	(km)	800[36]	252[1]	224[66]
Inclination	(deg)	108[66]	38[66]	57[66]
Frequency	(GHz)	1.275[36]	1.278[66]	1.282[66]
N looks		4[66]	6[66]	4[66]
Azimuth res	(m)	25[36]	40[66]	25[66]]
Look angle	(deg)	20.5[36]	47[66]	60[66]
Incidence angle (mid)	(deg)	23[66]	50[66]	64[66]
Swath width (ground)	(km)	100[36]	50[66]	60[66]
Ground range res	(m)	25[36]	40[66]	17[66]
Noise Equiv σ°	(dB)	-24[66]	-32[66]	-28[66]
Tx Pulse width	(μs)	33.8[36]	30.4[35]	30.4[64]
PRF (lower limit)	(Hz)	1464[36]	1463[35]	1464[64]
PRF (upper limit)	(Hz)	1647[36]	1640[35]	1824[64]
Noise figure	(dB)			
Noise temperature	(K)	550[15]		
Tx bandwidth	(MHz)	19[36]	6[66]	12[66]
Av Tx power	(W)	55[36]	55[35]	250
Peak Tx power	(W)	1000[36]	1000[66]	1000[66]
Antenna length	(m)	10.7[36]	9.4[66]	10.7[66]
Antenna width	(m)	2.16[36]	2.16[66]	2.16[66]
Azimuth beamwidth	(deg)	1.1[15]	1.4[15]	1.1[15]
Elevation beamwidth	(deg)	6.2[15]	6.2[15]	6.2[15]
Antenna gain	(dBi)	35[36]	32.4[35]	33.0[15]
Pointing error (roll)	(deg)	0.2[36]	1[21]	1[21]
Pointing error (pitch)	(deg)	0.5[36]	1[21]	1[21]
Pointing error (yaw)	(deg)	0.2[36]	1[21]	1[21]
Antenna weight	(kg)	113[15]	200[64]	324[64]
Polarization		HH[66]	HH[66]	HH[66]
Quantizer resolution	(bits)	5[35]	analog[66]	3-6[66]
Quantization Rate	(MHz)			
Buffered data rate	(Mbits/s)	110[66]		30[66]
Radar DC power	(W)	624[15]	785[64]	865[64]
Electronics dimensions	(cm)	120x30x30[48]	60x70x55[48]	60x70x55[48]
Electronics weight	(kg)	129[36]	198[64]	231[64]
RF Amplifier Type		solid-state[35]	solid-state	solid-state[21]

Table 4.1.1b: SPACE-BASED SAR SYSTEMS - PRESENT

PARAMETER	UNITS	ALMAZ II	ERS-1	JERS-1
Launch date		03/31/91[66]	07/17/91[48]	02/11/92[1]
Altitude	(km)	300[66]	777[48]	570[1]
Inclination	(deg)	73[66]	98.5[66]	97.7[66]
Frequency	(GHz)	3.0[66]	5.25[66]	1.275[66]
N looks		2[21]	4[66]	3[66]
Azimuth res	(m)	15[66]	28[2]	18[66]
Look angle	(deg)	30-60[66]	20[66]	35[66]
Incidence angle (mid)	(deg)	30-60[21]	23[66]	38[66]
Swath width (ground)	(km)	20-45[66]	100[66]	75[66]
Ground range res	(m)	15-30[66]	26[2]	18[66]
Noise Equiv σ°	(dB)	-33[JPL91]	-24[2]	-20.5[66]
Tx Pulse width	(μs)	0.07[39]	37.1[2]	35.2[50]
PRF (lower limit)	(Hz)	3000[39]	1680[2]	1505.8[50]
PRF (upper limit)	(Hz)	3000[39]	1700	1606[50]
Noise figure	(dB)	3[39]		3.4[50]
Noise temperature	(K)			
Tx bandwidth	(MHz)		15.5[66]	15[66]
Av Tx power	(W)	80[39]	300	
Peak Tx power	(W)	190000[39]	4800[48]	1268-1426[50]
Antenna length	(m)	15[66]	10[66]	11.9[66]
Antenna width	(m)	1.5[66]	1[66]	2.4[66]
Azimuth beamwidth	(deg)	0.33[44]	0.288[2]	0.99[50]
Elevation beamwidth	(deg)	3.3[56]	5.4[2]	5.51[50]
Antenna gain	(dBi)		40[2]	34.11[50]
Pointing error (roll)	(deg)		0.02[2]	0.16[50]
Pointing error (pitch)	(deg)		0.02[2]	0.13[50]
Pointing error (yaw)	(deg)		0.02[2]	0.24[50]
Antenna weight	(kg)			132.26[50]
Polarization		HH[66]	VV[66]	HH[66]
Quantizer resolution	(bits)	3[21]	5-6[2]	3[50]
Quantization Rate	(MHz)		18.96[2]	17.076[50]
Buffered data rate	(Mbits/s)	37[48]	105[66]	60[66]
Prime DC power	(W)		1800	1850
Electronics dimensions	(cm)		90x80x75[48]	120x80x30[48]
SAR weight	(kg)	4000[48]	512[48]	89.068[50]
RF Amplifier Type		tube	TWT[2]	solid-state[50]

Table 4.1.1c: SPACE-BASED SAR SYSTEMS - FUTURE

PARAMETER	UNITS	SIR-C(L/C)	SIR-C(X)	RADARSAT
Launch date(s)		93,94,96[66]	93,94,96[66]	Dec-94[66]
Altitude	(km)	225[66]	225[66]	793-821[56]
Inclination	(deg)	57[66]	57[66]	98.6[66]
Frequency	(GHz)	1.25(L),5.3(C)[66]	9.6[66]	5.3[66]
N looks		4[66]	4[66]	1-16[66]
Azimuth res	(m)	25[66]	25[66]	10-100[66]
Look angle	(deg)	15-55[66]	15-55[66]	20-59[66]
Incidence angle (mid)	(deg)			20-60[56]
Swath width (ground)	(km)	15-60[66]	15-40[37]	45-500[66]
Ground range res	(m)	60-10[66]	60-10[66]	10-100[66]
Noise Equiv σ°	(dB)	-48(L),-36(C)[66]	-28[66]	-23[66]
Tx Pulse width	(μs)	8.4,16.9,33.8[32]	40[37]	42.0[56]
PRF (lower limit)	(Hz)	1395[37]	1395[37]	1270[56]
PRF (upper limit)	(Hz)	1736[37]	1736[37]	1390[56]
Noise figure	(dB)			
Noise temperature	(K)	450(L),550(C)[37]		551[37]
Tx bandwidth	(MHz)	40(L),20(C)[66]	10[66]	30,17.3,11.6[66]
Av Tx power	(W)		220[48]	300[56]
Peak Tx power	(W)	3500(L),2200(C)[66]	3300[37]	5000[56]
Antenna length	(m)	12[66]	12[66]	15[66]
Antenna width	(m)	2.95(L),0.25(C)[66]	0.4[66]	1.5[66]
Azimuth beamwidth	(deg)	1.0(L),0.25(C)[37]	0.14[37]	
Elevation beamwidth	(deg)	4.9-16[37]	5.5[37]	
Antenna gain	(dBi)	36.4(L),42.7(C)[37]	44.5[37]	
Pointing error (roll)	(deg)	1[21]	1[21]	0.2[56]
Pointing error (pitch)	(deg)	1[21]	1[21]	0.2[56]
Pointing error (yaw)	(deg)	1[21]	1[21]	0.2[56]
Antenna weight	(kg)	900[15]	49[37]	
Polarization		quad[66]	VV[66]	HH[66]
Quantizer resolution	(bits)	8[32]	4-6[37]	4[56]
Quantization Rate	(MHz)	45[32]	45	
Buffered data rate	(Mbits/s)	90[37]	45[37]	74-105[66]
Prime DC power	(W)	2000[64]		2500[56]
Electronics dimensions	(cm)	65x70x60[48]	40x50x60[48]	80x60x60[48]
SAR weight	(kg)	408[64]		
RF Amplifier Type		T/R modules[37]	tube[37]	tube[56]

ALMAZ and the shuttle imaging radar (SIR) SAR systems, all of the satellites are above 500 km altitude. This is because atmospheric drag due to particle density is very significant below 500 km altitude. Figure 4.1.1 illustrates this problem. ALMAZ carries a very large amount of fuel to maintain its altitude, and the SIR missions are very short duration. One reason to go to higher orbits is that it gives a larger instantaneous field-of-view (IFOV). Generally this is not as important for SAR because pulse repetition frequency (PRF) and power issues dominate the choice of swath width.

Other than the shuttle missions, all of the orbits are highly inclined near-polar orbits of 73° to 108°. The polar orbits give a larger coverage of the earth, including the poles, required for earth monitoring. The shuttle missions are limited in latitudes because they are manned and this avoids the high radiation doses at the poles.

Typical peak transmitter powers are on the order of 1 to 5 kW, with the average powers around 50 to 300 W. The prime DC power (input power required) is 0.6 to 2.5 kW. Typical SAR electronic weights are on the order of 100 to 500 kg. Typical antenna weights are 100 to 350 kg. These SARs do not

TABLE 4.1.2: TRENDS IN SPACE-BASED SARS

Parameter	Past and Present Selections	Next Generation Selections
Altitude	225 - 800 km	225 - 800 km
Orbit Inclination	~98°	~98°
Number of Channels	1	single, multiple
Frequency	L-band, C-band	L-band, C-band, X-band
Resolution	20 - 40 m	10 - 100 m
Polarization	single, usually HH	single or quad
σ_n°	-20 to -30 dB	-20 to -50 dB
Swath Width	50 - 100 km	15 - 500 km
Incidence Angle	fixed, 20°- 60°	variable, 20°- 60°
Antenna Length	9 - 12 m	12 - 15 m
RF Amplifier Type	central, solid-state	solid-state and tubes
Prime Power	1 - 2 kW	2.5 kW
PRF	1400 - 1800 Hz	1300 - 1700 Hz
Pulse Width	30 - 40μs	8 - 40 μs
Quantizer Resolution	5 - 6 bits	4 - 8 bits
Processing	ground based	ground based

perform any on board signal processing. Buffered data rates are on the order of 30 to 110 Mbps.

Some of the trends that can be inferred from the data in the previous section and other literature are summarized in table 4.1.2.

4.2 Power and Weight

Two key parameters for determining launch vehicle type and launch costs are system power and weight. Increased power translates to increased weight due to larger solar panels and more batteries.

SAR system weight is very difficult to estimate without detailed design. A little information can be gleaned from the literature. From [40], it is apparent that SAR weight and average SAR transmitter power are strongly correlated. In that study, the SAR weight is approximately 6 to 7 kg/W of average power. From Table 4.1.1, this value is 1 to 3 kg/W of average power. Average and peak transmitter power requirements are discussed in section 5.4.

In addition, to the SAR weight, the SAR antenna weight and dimensions are important. Approximate antenna weights range from 4 to almost 20 kg/m^2.

Another important parameter is the power that must be delivered by the satellite, referred to as the prime or primary DC power. Each of the satellites in Table 4.1.1 have other instruments on the satellite bus; however, as a reference, they have prime DC power that is approximately 6 to 15 times the average SAR transmitter power.

Another question is how much power is it possible for the satellite to deliver? According to [16], Air Force studies indicate that spacecraft technology should be able to deliver 5 to 15 kW by the 1990's, with the possibility in the future of delivering 50 kW or more. Peak power to average powers of more than 10/1 are predicted also. The greater the power requirements, the greater the weight for the power system. Technology improvements may improve power system weights, also. Similar predictions are made in [47].

It should be pointed out that all of the numbers in this section provide only a "rule of thumb". Only detailed design will provide accurate weights and power requirements. Also, structure, bus, and power system weights are not included in these numbers.

4.3 Satellite Telemetry and Data Rates

Data rates required for spaceborne SAR are among the highest of any satellite application. As swath width and/or spatial resolution are increased, the corresponding data rate increases.

State-of-the-art microwave telemetry capacity, based on a literature search, appears to be about 300 Mb/s for the case of the NASA TDRSS (tracking and data relay satellite system) [8]. Near term performance trends are best demonstrated by the next generation advanced TDRSS (ATDRSS) which is anticipated to be in operation by the late-1990's will have one channel with capacity of about 650 Mb/s with second channel with capacity of 300 Mb/s. Factors prompting this increase in data rates include Space Station Freedom activities, Earth Observation System (EOS) requirements, and the Hubble space telescope.

Another emerging trend for high data rate systems is the use of optical data communications for intersatellite communications. Projected capacities for satellite-to-satellite systems range from 500 Mb/s to 1 Gb/s [14], [28]. Realization of these systems appear to be farther in the future.

Based on this limited investigation, it seems apparent that data rates below about 250 Mb/s should be manageable, data rates of up to 500 to 600 Mb/s are pushing the state-of-the-art, and systems requiring

data transmission rates of over 1 Gb/s will require significant technology development before they can be realized.

4.4 Other Issues Concerning Spaceborne SAR Systems

Other subjects important to spaceborne SAR systems include the orbit knowledge (ephimeral data) and the space environment. Since, as noted previously, spaceborne SARs are located in low-earth orbits, this section will concentrate on these orbits.

The orbit altitude and velocity are part of what is referred to as the ephimeral data. The process of determining the ephimeral data is called tracking.

Although the literature concerning the achievable accuracy in estimating ephimeral data is confusing, the trend toward using Global Positioning Satellite (GPS) receivers on low-earth orbit satellites is clear. LANDSAT 4 was the first satellite to use an onboard GPS receiver [7, 38]. The TOPEX experiment will implement a sophisticated GPS receiver, including using carrier phase and differential GPS to obtain altitude to better than 10 cm [68]. This same reference reports that for low-earth orbit satellites the results of using these techniques are not quite as good due to uncertainties introduced by drag at the lower orbits; however, altitude accuracies of just under 1m are achievable. Typical accuracies using other techniques appears to be on the order of 100 m when the satellite is near a ground station [51].

The motion compensation requirements for SAR are discussed in section 9-6.3 of [63]. Although the motion should be much more stable in the spacecraft environment than in the aircraft environment, it is unclear how predictable it is in the spacecraft environment. Some questions that arise include: 1) is some sort of motion measurement system required on the spacecraft? 2) is an autofocus technique accurate enough? and/or 3) are motion models accurate enough to be able to pre-(post-)calculate motion and motion correction terms ahead of (after) time?

The issues concerning the satellite environment are very important. This study did not focus on these issues. In general some of the important issues include:

1) A difficult thermal environment which must consider removal of heat generated by the on-board electronic systems, thermal cycling due to moving in and out of the sun, heating due to plasma and radiation, and freezing.

2) A difficult electrical environment, due to charging of the spacecraft from the surrounding plasma and magnetic fields. Equipment must be designed to prevent or handle arcing.

3) Cosmic and trapped ionized particles which cause degradation of semiconductor performance. In addition, particles from "outer-space" often carry enough energy to alter operation (single-event upsets or SEUs) or open circuit and damage electronics (single-event latchup or SELs). For the low-earth orbit environment, the radiation dose is low compared with geosynchronous orbits. The radiation dose may be 10 to 1000 rad/year. Radiation dose increases approximately as the 5th power of altitude [67] at the lower altitudes. For low-earth orbits, single-event phenomena (SEP), are very important.

4) Meteorite and man-made debris are a significant hazard especially for large exposed surfaces such as solar collectors or antennas.

5) Corrosion at low-earth orbits of exposed surfaces such as the antenna is important due to the highly corrosive atmosphere (mainly from the concentration of atomic oxygen).

4.5 Summary of Literature

The following bibliography lists articles and references on spaceborne SAR by subject category:

Ambiguity Issues

F. Li and W. Johnson, "Ambiguities in Spaceborne Synthetic Aperture Radar Systems", *IEEE Trans. on Aerospace and Electronic Systems*, Vol. AES-19, No. 3, May 1983, pp. 389-396.

R. Raney and J. Princz, "Reconsideration of Azimuth Ambiguities in SAR", *Proc. of IGARRS '86*, Sept. 1986, pp. 1175-1179.

Antennas

H. Braun and R. Wagner, "Antennas on the First ESA Remote Sensing Satellite ERS-1", *1989 IEEE Antennas and Propagation Symposium*, June 1989, pp. 511-514.

B. Gilchrist, N. Stacy, J. Daida and J. Vesecky, "A Conceptual Design for a Microwave Active Phased Array SAR", *IEEE EASCON '86*, Sept. 1986, pp. 181-190.

F. Sawyer, S. Hartley and M. Brown, "Versatile SAR for the First Polar Platform", *GEC Journal of Research*, Vol. 9, No. 1, 1991, pp. 13-22.

D. Zimcik, L. Martins-Camelo and P. Cowles, "Development of the RADARSAT SAR Antenna", *Canadian Aeronautics and Space*, Vol. 34, No. 2, June 1988, pp. 102-106.

Attitude Controls and Issues

B. Aster and P. Stasio, "Modelling Earth Rotation and Spaceborne Attitude Errors for Theor(et)ic Doppler Parameters Evaluation", *Proc. of IGARRS '91*, pp. 2409-2411.

R. Bamler and H. Runge, "A Novel PRF-Ambiguity Resolver", *Proc. of IGARRS '91*, pp. 1035-1038.

R. Bamler and H. Runge, "PRF-Ambiguity Resolving by Wavelength Diversity", *IEEE Trans. on Geoscience and Remote Sensing*, Vol. 29, No. 6, Nov. 1991, pp. 997-1003.

C. Chang and J. Curlander, "Attitude Steering for Space Shuttle Based Synthetic Aperture Radars", *Proc. of IGARRS '92*, May 1992, pp. 297-301.

T. Misra, A. Jha and N. Pillai, "Doppler Parameters Estimation Criteria for the Spaceborne SAR and Corresponding Attitude Determination Accuracy Limits", *Proc. of IGARRS '89*, July 1989, pp. 2604-2607.

J. Mohl, R. Dieter and A. Muckle, "Attitude Determination and Control for the RADARSAT Spacecraft", *Advances in the Astronautical Sciences*, Vol. 78, 1992, pp. 21-54.

H. Runge, "Benefits of Antenna Yaw Steering for SAR", *Proc. of IGARRS '91*, pp. 257-261.

C. Wu, J. Curlander and A. DiCenzo, "Determination of Spacecraft Attitude Using Synthetic Aperture Radar Data", *AIAA Sensor Systems for the '80s Conf.*, Dec. 1980, pp. 57-60.

Calibration

P. Hans, H. Braun, and H. Grobke, "ERS-1 System Simulation and Calibration", *Proc. of IGARRS '84*, Aug. 1984, pp. 841-846.

R. Cox and F. Sawyer, "Verification Techniques for Satellite-Borne Synthetic Aperture Radars", *Proc. of IGARRS '84*, Aug. 1984, pp. 847-852.

P. Seifert and H. Blostcher, "Preparatory Investigations Concerning the Calibration of Spaceborne SAR-Systems", *Proc. of IGARRS '91*, pp. 1381-1384.

Doppler from Space

E. Meier, C. Graf and D. Nuesch, "Generation of Geocoded Spaceborne SAR Image Products", *Proc. of IGARRS '89*, July 1989, pp. 2473-2477.

R. Raney, "A Comment on Doppler FM Rate", *International Journ. of Remote Sensing*, Vol. 8, No. 7, 1987, pp. 1091-1092.

R. Raney, "Doppler Properties of Radars in Circular Orbits", *International Journ. of Remote Sensing*, Vol. 7, No. 9, 1986, pp. 1153-1162.

Doppler Parameter Estimation

R. Bamler, "Ultimate Bounds for Doppler Centroid Estimators", *Proc. of IGARRS '90*, pg. 1337.

Carmine and Tarantino, "Comparison Between Different Doppler Centroid Estimation Methods for Spaceborne SAR Processing", *Proc. of IGARRS '91*, pp. 1047-1049.

F. Li, D. Held, J. Curlander, and C. Wu, "Doppler Parameter Estimation for Spaceborne Synthetic-Aperture Radars", *IEEE Trans. on Geoscience and Remote Sensing*, Vol. GE-23, No. 1, Jan. 1985, pp. 47-56.

General Space Issues

M. Cohen, E. Fornoles and T. Mahefkey, "Requirements and Technology Trends for Future Military Space Power Systems", *Proc. of the 16th Intersociety Energy Conversion Engineering Conference*, Aug. 1981, pp. 2122-2125.

J. Wertz and W. Larson (editors), *Space Mission Analysis and Design*, Kluwer Academic Publishers, 1991.

General Spaceborne SAR and Radar

L. Cantafio (editor), *Space-Based Radar Handbook*, Artech House, 1989.

J. Curlander and R. McDonough, *Synthetic Aperture Radar - Systems and Signal Processing*, John Wiley & Sons, 1991.

C. Elachi, *Spaceborne Radar Remote Sensing: Applications and Techniques*, IEEE Press, 1988.

R. Moore, "Some Trade-offs in Modest-Resolution Radars for Space", *Proc. of IGARRS '86*, Sept. 1986, pp. 703-708.

H. Kashihara, K. Tanaka, M. Fukai, et al., "A Case Study of Space-Borne Synthetic Aperture Radar System Design for the Earth Resources Satellite", *Proc. of IGARRS '84*, Aug. 1984, pp. 815-820.

R. Raney, "SNR Considerations for an Orbital SAR", *Proc. of IGARRS '90*, pg. 1125.

Image Formation

B. Barber, "Theory of Digital Imaging from Orbital Synthetic Aperture Radar", *Int'l. J. of Remote Sensing*, Vol. 6, No. 7, pp. 1009-1057, 1985.

M. Jin and C. Wu, "A SAR Correlation Algorithm which Accomodates Large-Range Migration", *IEEE Trans. on Geoscience and Remote Sensing*, Vol. GE-22, No. 6, Nov. 1984, pp. 592-597.

C. Wu, K. Liu, and M. Jin, "Modeling and a Correlation Algorithm for Spaceborne SAR Signal", *IEEE Trans. on Aerospace and Electronic Systems*, Vol. AES-18, No. 5, Sept. 1982, pp. 563-575.

Ionosphere Effects

S. Quegan and J. Lamont, "Ionospheric and Tropospheric Effects on Synthetic Aperture Radar Performance", *Int. J. Remote Sensing*, Vol. 7, No. 4, 1986, pp. 525-539.

Multi-Beam/Multi-Phase Center Techniques

C. Bosswetter, A. Wolframm, T. Pike and J. Hermer, "Concepts for High Resolution Space Based SAR/ISAR Systems - Preliminary Design Considerations", *Proc. Military Microwaves '90 Conf.*, July 1990, pp. 521-529.

A. Currie, "Synthetic Aperture Radar", *Electronics & Communication Engineering Journal*, Aug. 1991, pp. 159-170.

A. Currie and C. Hall, "A Synthetic Aperture Radar Technique for the Simultaneous Provision of High-Resolution Wide-Swath Coverage", *Proc. Military Microwaves '90 Conf.*, July 1990, pp. 539-544.

A. Currie and M. Brown, "Wide-Swath SAR", *IEE Proceedings-F*, Vol. 139, No. 2, April 1992, pp. 122-135.

Orbit Issues

W. Birmingham, B. Miller and W. Stein, "Experimental Results of Using the GPS for Landsat 4 Onboard Navigation, Global Positioning System", Vol. II, pp. 231-238.

E. Cutting, J. Born and J. Frautnick, "Orbit Analysis for SEASAT-A", *The Journal of the Astronautical Sciences*, Vol. XXVI, No. 4,Oct.-Dec. 1978, pp. 315-342.

P. Jorgensen, "Navigating Low Altitude Satellites Using the Current Four NAVSTAR/GPS Satellites", Global Positioning System, Vol. II, pp. 112-121, 1983.

T. Yunck, W. Melbourne and C. Thornton, "GPS-Based Satellite Tracking System for Precise Positioning", *IEEE Trans. on Geoscience and Remote Sensing*, Vol. GE-23, No. 4, July 1985, pp. 450-457.

Past, Present, and Planned SAR Systems

J. Cimino and D. Held, "The Earth Observing System (EOS) Synthetic Aperture Radar (SAR)", *IGARSS '86*, August 1986, pp. 94-107.

C. Elachi,"Spaceborne Imaging Radar Research in the 1990s: An Overview", *Johns Hopkins APL Technical Digest*, Vol. 8, No. 1, 1987, pp. 60-64.

B. Huneycutt, "Spaceborne Imaging Radar - C Instrument", *IEEE Trans. on Geoscience and Remote Sensing*, Vol. 27, No. 2, March 1989, pp. 164-169.

H. Jatsch, E. Langer, H. Ottl and K. Zeller, "Concept of an X-Band Synthetic Aperture Radar for Earth Observing Satellites", *Journ. of Electromagnetic Waves and Applications*, Vol. 4, No. 4, 1990, pp. 325-340.

R. Jordan, "Synthetic Array Radars in Space", *1980 WESCON Conf. Record*, pp. 1-8.

R. Jordan, "The Seasat-A Synthetic Aperture Radar System", *IEEE Journ. of Oceanic Engineering*, Vol. OE-5, No. 2, April 1980, 154-164.

H. Joyce, R. Cox, and F. Sawyer, "The Active Microwave Instrument for ERS-1", *IGARRS '84*, Aug. 1984, pp. 835-840.

T. W. Thompson and A. Lederman, "SEASAT-A Synthetic Aperture Radar: Radar System Implementation", *Oceans '76 Conference, IEEE*, Washington D. C., 1976.

Space Environment

J. C. Anderson, "Cost-Reduction Techniques for Low Earth-Orbit Signal Processors", *Proceedings from the International Conference on Signal Processing Applications and Technology*, Nov., 1992, Cambridge, MA, pp. 228-234.

E. Mahefkey, "Military Spacecraft Thermal Management: The Evolving Requirements and Challenges", in *Progress in Astronautics and Aeronautics*, M. Summerfield (editor-in-chief), Vol. 86, 1986, pp. 3-16.

J. McDonald, "A New Agenda for Rad-Hard IC Development", Military & Aerospace Electronics, pp. 25-27.

Telemetry Rates

D. L. Brandel, W. A. Watson, and A. Weinberg, "NASA's Advanced Tracking and Data Relay Satellite System for the Years 2000 and Beyond." *Proceedings of the IEEE*, v. 78, n. 7, July 1990, pp. 1141-1152.

S. J. Campanella and R. K. Garlow, "RF/optical design for optical intersatellite links", *Microwave Journal*, v.34, n. 10, Oct 1991, pp. 85-86, 88, 90, 93-94, 101, 103, 106.

J. Fischer, "Optical data communication for Earth observation satellite systems", *Proceedings of the Second European Conferecne on Satellite Communications*, ECSC-2 (ESA Sp-332) 1991, pp. 405-415.

5.0 General Spaceborne SAR Issues

This section goes into more of the details of several areas important to spaceborne SAR. The SAR areas discussed in this section include:

1) Spaceborne SAR PRF
2) Multiple Phase Center/Multibeam SAR systems
3) SAR image processing
4) Transmitter power (the Radar Equation)
5) Propagation
6) Antennas

5.1 Spaceborne SAR PRF Issues

For a spaceborne SAR, PRF (pulse repetition frequency) is an important parameter that influences many other system parameters. Factors that affect PRF availability include radar velocity, antenna length, swath width, incidence angle, transmitter pulse length, and altitude. System parameters affected by PRF selection include peak transmitter power, duty factor, and raw data rate. In addition, due to PRF constraints, some combinations of swath width and antenna length may be incompatible as the Nyquist requirement and the ambiguity constraints may conflict.

Figure 5.1.1 illustrates the basic spaceborne radar geometry used for this section of the report. Concepts and guidance for this section were extracted from the [53], [40], and [26].

5.1.1 SAR PRF Introduction

As a brief introduction, a greatly simplified presentation of the PRF issue is now offered. This presentation is originally given in [53]. In an ideal situation, the radar transmits pulses of infinitely small duration and receives a pulse of time duration, τ_w, corresponding to the slant range swath width of W_r. The maximum PRF would be determined by continous reception of back to back pulses, i.e.:

$$PRF_{max} \leq \frac{1}{\tau_w} = \frac{c}{2 \cdot W_r} \qquad (5.1.1.1)$$

The minimum PRF is determined by the Nyquist sampling of the azimuth beamwidth. Assuming all of the beamwidth is used for azimuth integration, this can be stated as:

$$PRF_{min} \geq \frac{V_{st}}{\rho_a} \qquad (5.1.1.2)$$

where:
V_{st} - is the satellite velocity
ρ_a - is the azimuth resolution

We know that the maximum PRF must be greater than or equal to the minimum PRF and that the actual PRF must lie somewhere between these values. Combining equations (5.1.1.1) and (5.1.1.2) and rearranging leads to the following limit on the ratio of the range swath to azimuth resolution:

$$\frac{W_r}{\rho_a} \leq \frac{c}{2 \cdot V_{st}} \qquad (5.1.1.3)$$

For low earth orbit satellites, the velocity is approximately 7.5 km/sec. so that equation (5.1.1.3) becomes approximately:

$$\frac{W_r}{\rho_a} \leq 20000 \qquad (5.1.1.4)$$

In general practice, this bound is not achievable. Exceeding this bound requires sophisticated techniques such as those described in section 5.2. The following sections elaborate on the factors which determine the usable PRFs.

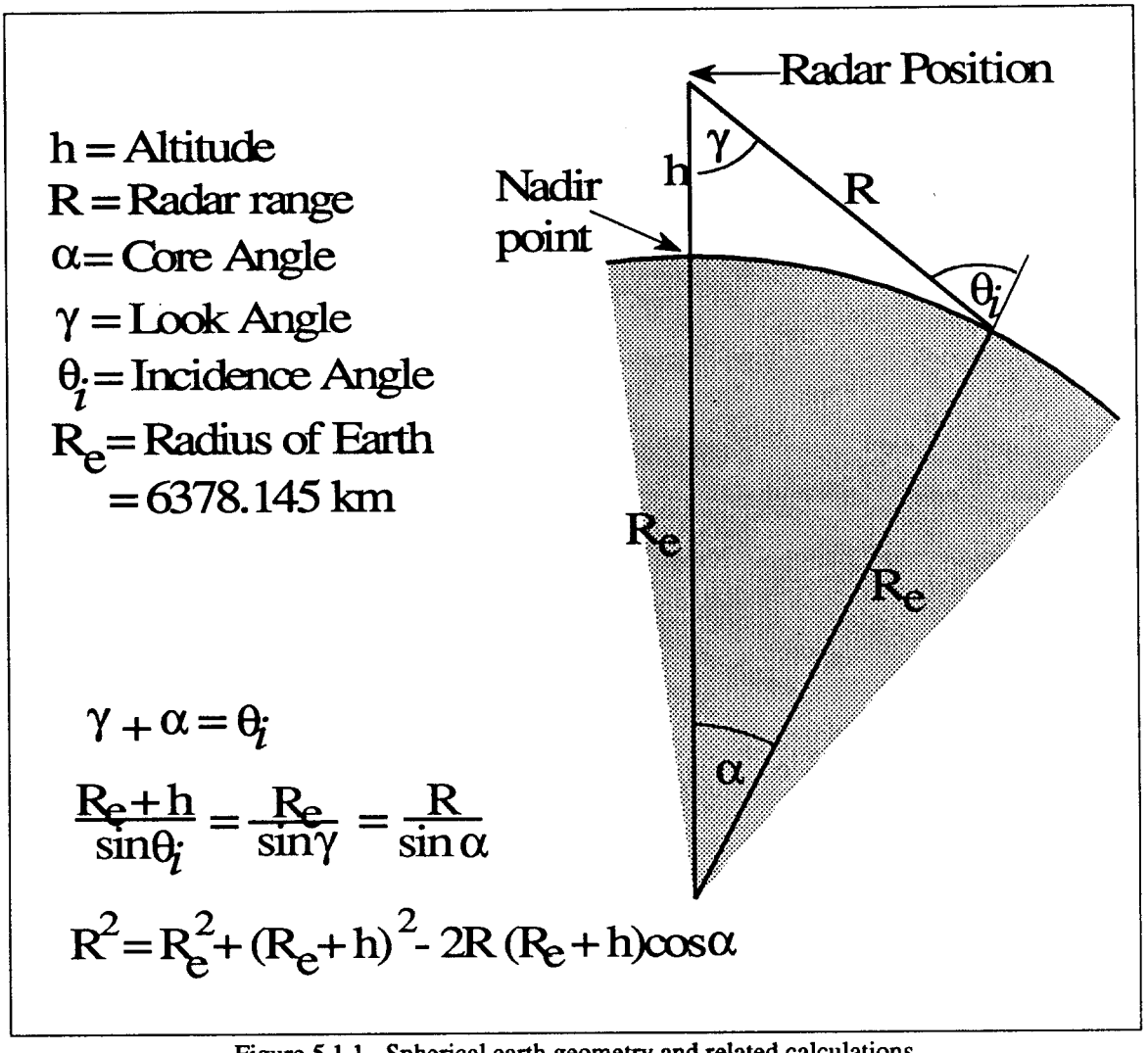

Figure 5.1.1. Spherical earth geometry and related calculations.

One final general comment on PRF before looking at the details, concerns a common term referred to as the "minimum antenna area". The minimum antenna area can be derived from the ratio of the maximum to minimum PRFs (ignoring pulse length). The details of the derivation are given in [15]. The resulting equation is:

$$A_{min} = \frac{4 \cdot V_{st} \cdot \lambda \cdot R \cdot \tan(\theta_i)}{c} \qquad (5.1.1.5)$$

where:

A_{min} - is the minimum antenna area

Refer to section 6.2 for a discussion of the impact of the minimum antenna area.

5.1.2 Minimum PRF

To satisfy the Nyquist sampling criteria in a stripmap mode SAR, the PRF must exceed the Doppler bandwidth of the imaged scene. The Doppler bandwidth, BW_{Dop}, is:

$$BW_{Dop} = \frac{2 \cdot \beta_{az} \cdot V_x}{\lambda} \qquad (5.1.2.1)$$

where:

β_{az} - is the antenna's azimuthal (or along-track) half power beamwidth
V_x - is the radar velocity
λ - is the radar wavelength

For a diffraction limited antenna the half power beamwidth, β_{az}, and wavelength, λ, are related by:

$$\beta_{az} = \frac{\lambda}{D_a} \qquad (5.1.2.2)$$

where:

D_a - is the along-track (azimuth) length of the real antenna

Note that in stripmap mode the finest along-track resolution (ρ_a) is $D_a/2$ (refer to section 5.3.3).

For a satellite in circular orbit, the velocity is given in Appendix A, equation (A.1). For a SAR on a satellite in a circular earth orbit operating in stripmap mode, the minimum PRF is determined by the orbit altitude, and the antenna length. Combining (5.1.2.1), (5.1.2.2), and (A.1) we get the lower bound for the PRF of:

$$PRF_{min} = \frac{2}{D_a} \cdot \sqrt{\frac{G}{R_s}} \qquad (5.1.2.3)$$

where:

G - is the universal gravitational constant, 3.983e5 km^3/sec^2
R_s - - is the radius of the satellite to the center of the earth, $R_s = R_e + h$

It is significant to note that PRF_{min} does not depend on the wavelength, λ. That is, PRF_{min} is frequency independent.

5.1.3 Maximum PRF

The upper bound on the PRF is a result of the fact that the maximum echo duration must be less than the interpulse period (IPP), i.e., the length of time between transmit pulses or the reciprocal of the PRF. For a system with a transmit pulse length τ_p and a scene echo duration τ_w, the maximum PRF is

$$PRF_{max} = \frac{1}{\left(2 \cdot \tau_p + \tau_w\right)} \qquad (5.1.3.1)$$

where:

$$\tau_w = \frac{2 \cdot W_r}{c} \tag{5.1.3.2}$$

W_r - is the slant range extent of the swath, $W_r = R_f - R_n$
R_f - is the slant range to the far edge of the swath
R_n - is the slant range to the near edge of the swath
c - is the speed of light

Figure 5.1.3.1 illustrates this geometry.

The swath width, W_r, is approximately related to the swath width on the ground, W_{gr}, by:

$$W_r \approx W_{gr} \cdot \sin(\theta_i) \tag{5.1.3.3}$$

where:
θ_i - is the incidence angle

This is an approximation only due the curvature of the earth.

An exact relationship between W_r and W_{gr} requires spherical geometry as follows. Given a desired ground swath width, W_{gr}, a desired incidence angle at the swath center, $\theta_{i,m}$, and an altitude, h:

$$\gamma_m = \sin^{-1}\left[\frac{R_e \cdot \sin(\theta_{i,m})}{R_s}\right] \tag{5.1.3.4}$$

$$\alpha_m = \theta_{i,m} - \gamma_m \tag{5.1.3.5}$$

$$\alpha_s = \frac{W_{gr}}{R_e} \tag{5.1.3.6}$$

$$\alpha_n = \alpha_m - \alpha_s/2 \tag{5.1.3.7}$$

$$\alpha_f = \alpha_m + \alpha_s/2 \tag{5.1.3.8}$$

$$R_n = \sqrt{R_e^2 + R_s^2 - 2 \cdot R_e \cdot R_s \cdot \cos(\alpha_n)} \tag{5.1.3.9}$$

$$R_f = \sqrt{R_e^2 + R_s^2 - 2 \cdot R_e \cdot R_s \cdot \cos(\alpha_f)} \tag{5.1.3.10}$$

where:
γ_m - is the look angle to the middle of the swath
α_m - is the interior (core) angle at the middle of the swath
α_s - is the interior (core) angle subtended by the desired ground swath, W_{gr}

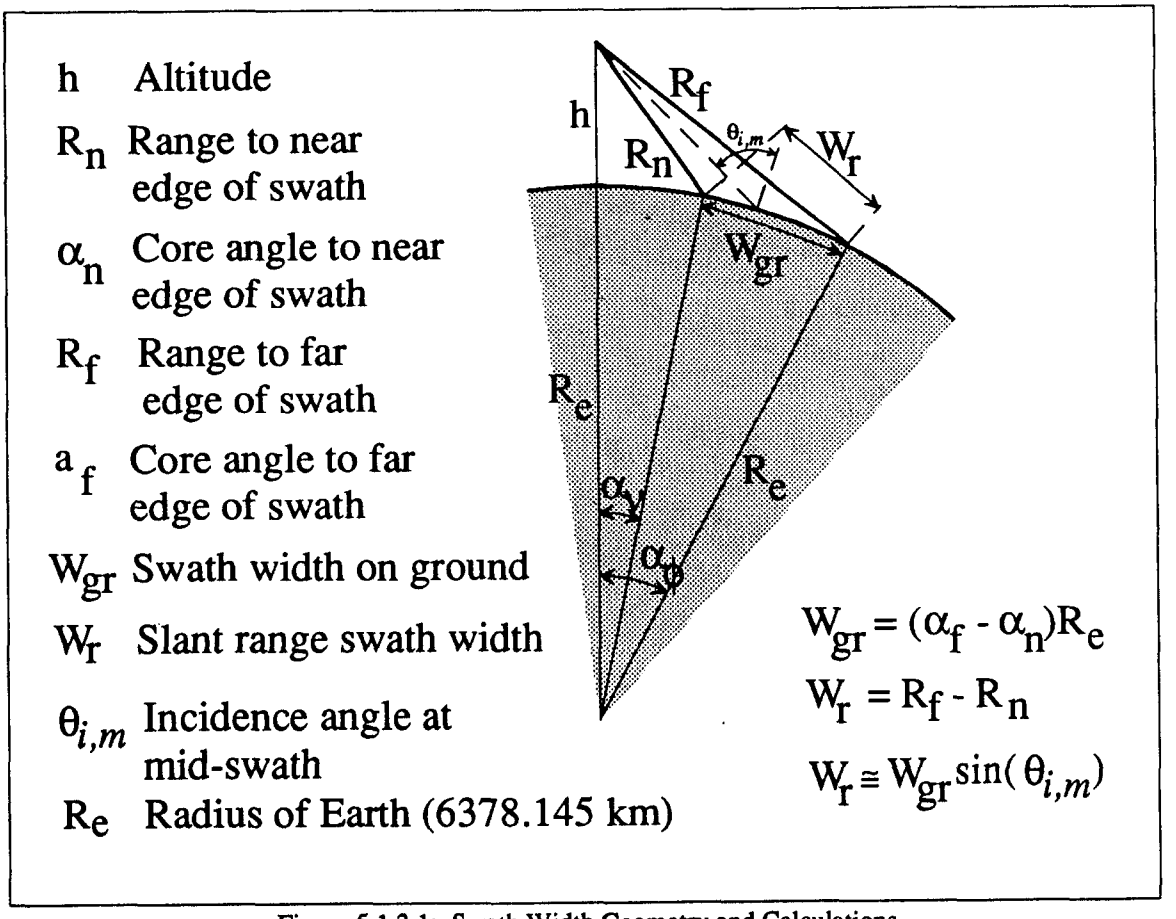

Figure 5.1.3.1: Swath Width Geometry and Calculations

The round trip propagation time to the near edge of the swath, τ_{near}, is:

$$\tau_{near} = \frac{2 \cdot R_n}{c} \tag{5.1.3.11}$$

and the round trip propagation time to the far edge of the swath, τ_{far}, is:

$$\tau_{far} = \frac{2 \cdot R_f}{c} \tag{5.1.3.12}$$

Note that τ_{far} does not include the effect of transmitter pulse width, τ_p. That is, the elapsed time from the beginning of the transmit pulse to the end of the scene echo is $\tau_{far} + \tau_p$. The maximum PRF is:

$$PRF_{max} = \frac{1}{\left(2 \cdot \tau_p + \tau_p - \tau_{near}\right)} \tag{5.1.3.13}$$

5.1.4 Avoiding Eclipsing (Blind Ranges)

Not all *PRF*s between PRF_{min} and PRF_{max} are available. Due to isolation problems inherent in radar systems, the receiver is "blind" during the transmit event. When the returning scene echo coincides with a transmit event, the received signal is said to have been eclipsed. PRFs that will result in eclipsing must be avoided. To avoid this condition the PRF must satisfy the inequality:

$$\frac{(N-1)}{(\tau_{near}-\tau_p)} < PRF < \frac{N}{(\tau_{far}+\tau_p)} \qquad (5.1.4.1)$$

where:

N - are whole numbers (1, 2, 3, ...) corresponding to pulses

*PRF*s which result in eclipsing depend on slant range to the near and far swath edges and the transmitter pulse width, T_{tx}. Figure 5.1.4.1 illustrates these transmitter blinding events with timing diagrams.

5.1.5 Avoiding Nadir Returns

For every transmitted pulse, an echo from nadir will result. These occur at a time τ_{nadir} from the beginning of the transmit pulse:

$$\tau_{nadir} = \frac{2 \cdot h}{c} \qquad (5.1.5.1)$$

where:

h - is the altitude over the nadir point

The nadir echo is significantly stronger than the imaged scene echo since the backscattering coefficient (σ°) is larger for incidence angles near 0°. The duration of the nadir echo is at least the length of the transmit pulse (τ_p) and for some terrain will last longer.

The situation to be avoided is when energy from the nadir echo is coincident in time with the energy from the scene echo. One solution to this approach is to avoid PRFs which cause a nadir echo to arrive at the receiver at the same time as the scene echo. Like the situation of the transmitter pulse eclipsing the scene echo, the PRFs which avoid nadir echoes coinciding with the scene echo are described by an inequality:

$$\frac{(M-1)}{(\tau_{near}-\tau_p-\tau_{nadir})} < PRF < \frac{M}{(\tau_{far}+\tau_p-\tau_{nadir})} \qquad (5.1.5.2)$$

where:

M - are whole numbers (1, 2, 3, ...) corresponding to pulses

PRFs which result in nadir echoes occurring during scene echo reception are determined by slant range to the near and far swath edges, the transmitter pulse width, τ_p, and the altitude of the radar over the nadir point.

Figure 5.1.4.1 illustrates these nadir echo eclipsing events with timing diagrams.

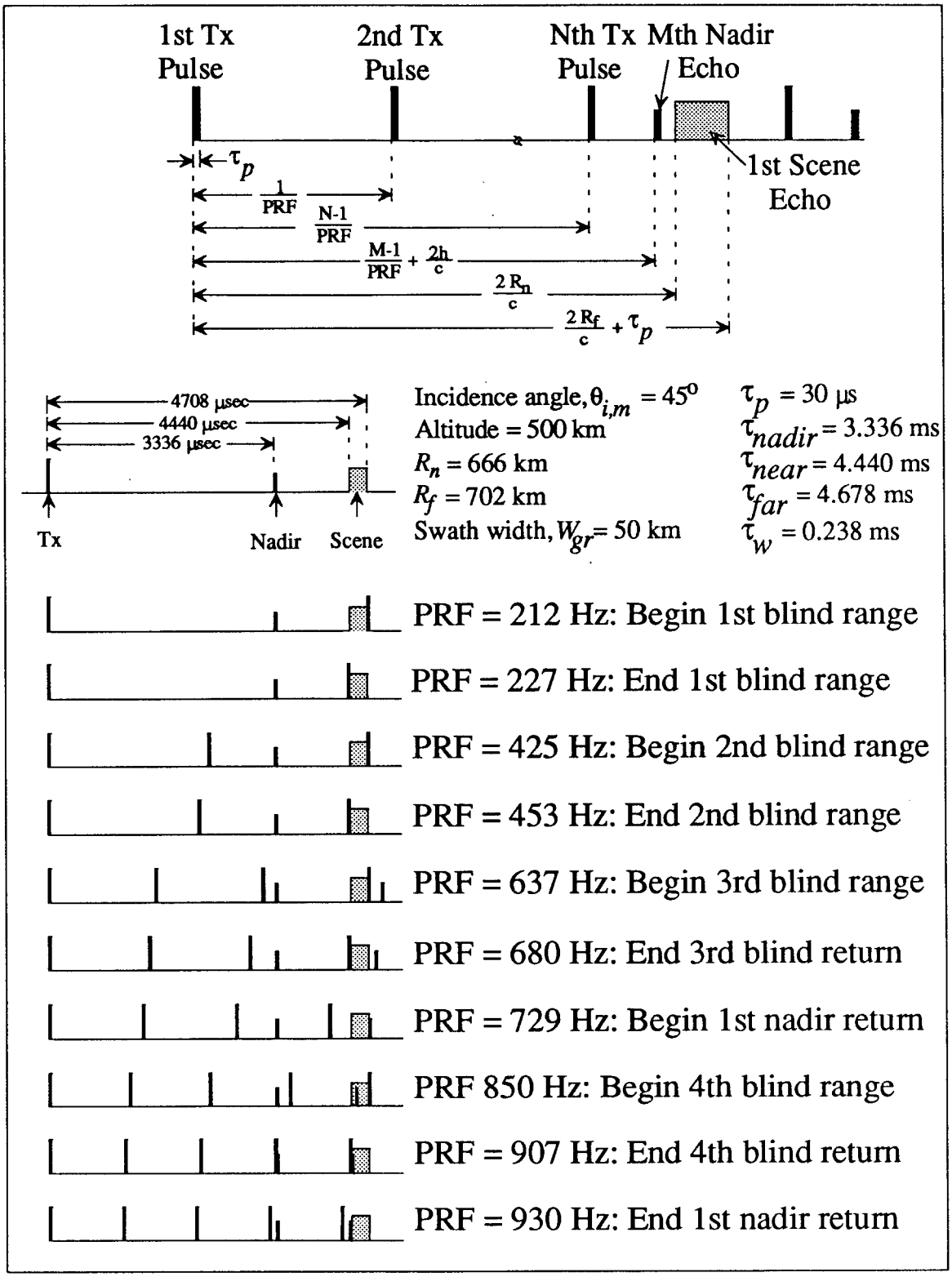

Figure 5.1.4.1: Radar Timing Relationships Between Transmit and Receive

5.1.6 Other Approaches to Avoiding Nadir Echo Effects

Nadir echoes occurring during scene echo reception degrade image quality. This occurs because either the energy from the nadir echo appears as a bright point or blob in the image, or as an increased background noise in the image due this energy having been smeared in range and azimuth throughout the image, or it may drive the receiver RF electronics into saturation. However it manifests itself, these effects are undesirable.

There are other approaches to avoid this energy from the nadir echo from corrupting the SAR image. These include:

(a) relying on the antenna to have a very low amount of gain in the direction of nadir;
(b) phase coding the transmit signals so that energy from different transmit pulses can be filtered at the receiver;
(c) changing the slope of the chirp waveform from positive to negative on an interpulse basis so that energy from different pulses will be smeared in the receiver.

Other schemes probably exist. A combination of these approaches e.g., time domain filtering (PRF selection), antenna angle filtering (null steering), and frequency filtering (phase coding/chirp slope flipping) could be used if the demands of avoiding PRFs which result in nadir echoes corrupting the image are too severe. One reference that discusses using a couple of these techniques is [20].

5.1.7 PRF Design Space

As presented above, the SAR system parameters which determine PRF availability include (1) radar altitude, (2) radar velocity, (3) antenna length, (4) incidence angle, (5) swath width, and (6) transmitter pulse length. No convenient means is available to present how PRF availability varies with regard to all of these parameters simultaneously in a 2-dimensional graph. Therefore a series of graphs representing how PRF availability varies versus a single SAR parameter will be used.

An example is shown in Figure 5.1.7.1. Shown here are the available values for PRF as the incidence angle varies from 15° to 70°. The scale on the PRF axis varies from 0 to 2500Hz. All contributing system parameters are listed in the figure caption. For example, swath width (on the ground) is shown to be 50 km. A vertical line is drawn on the graph indicating an incidence angle of 45° so that an easy comparison with the example shown in Figure 5.1.4.1 can be made. Note that system parameters in Figure 5.1.4.1 are the same. Antenna length and radar velocity are not shown in the Figure 5.1.4.1 example, as these parameters only effect PRF_{min}, and that was not addressed in Figure 5.1.4.1.

For each incidence angle, transmitter pulse eclipsing of the received signal occurs over a ranges of PRFs that represent bands of unavailable PRFs. These are depicted by solid lines with the interval between being filled with a cross-hatched pattern. Similarly, ranges of PRFs that represent bands unavailable due to nadir echo eclipsing of the received signal are depicted by dashed lines with a dashed cross-hatched fill pattern. The remaining zones outside these bands in the graph represent potentially available PRFs. Not shown are the limits PRF_{min} and PRF_{max}. For this particular example, due to the short antenna length, the PRF_{min} is 2500Hz so none of these PRFs shown in Figure 5.1.7.1 are available.

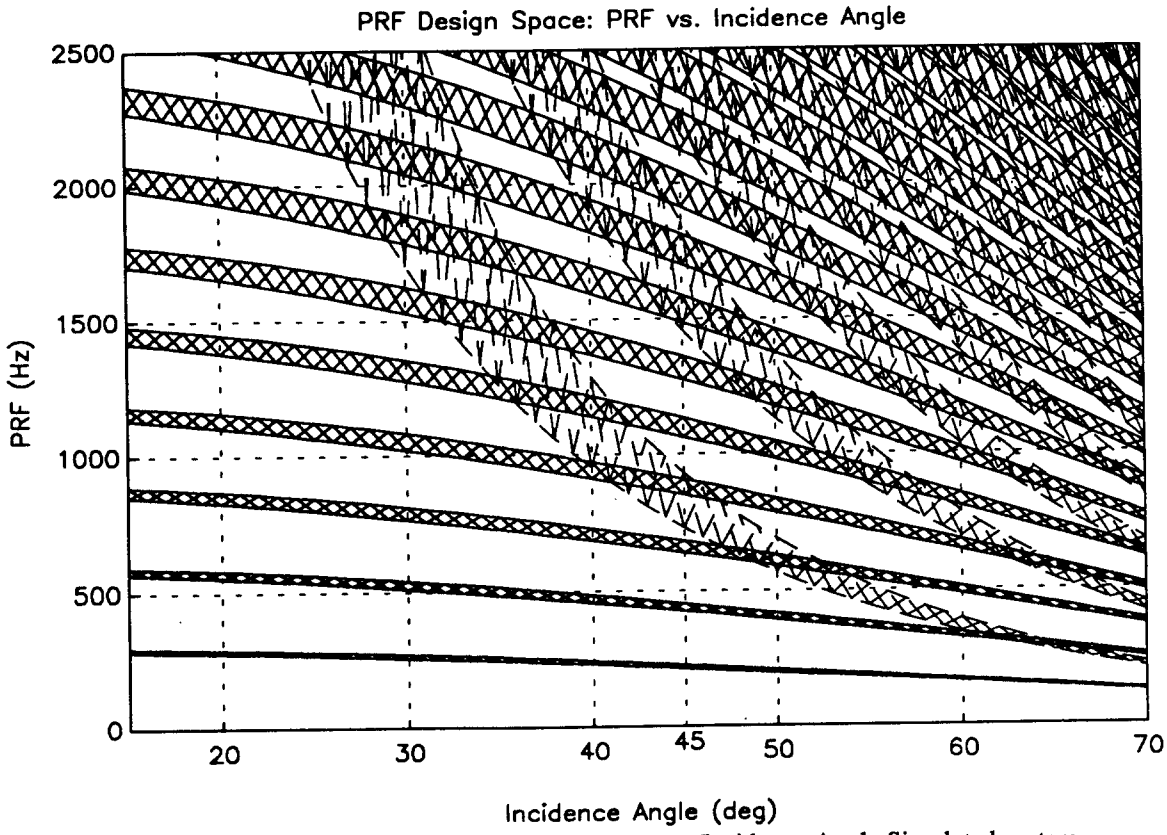

Figure 5.1.7.1: PRF design space example: PRF vs. Incidence Angle.Simulated system parameters: Altitude: 500 km, Velocity: 7613 m/s, Antenna Length: 6.0 m, Tx Pulse Length: 30.0 μs, Swath Width: 50 km

5.1.8 Spaceborne SAR Baseline Parameters

To proceed with a parametric evaluation of PRF availability for a spaceborne SAR, baseline system parameters must be selected. Some parameters, such as altitude, center frequency, and resolution, are fixed in this baseline study. Others, such as transmitter pulse length, incidence angle, antenna length, and swath width, are left as variables.

Some guidance is inherently available for these unspecified parameters. For example, antenna length must be no longer than twice the desired one-look, azimuthal resolution. Transmitter pulse length and PRF should be as large as possible to minimize peak transmitter power. It is desirable to make the swath width as large as possible, from a user's point of view. Incidence angle is strongly tied to system application - in some cases steep incidence angles (near nadir) may be desirable, in others near grazing (shallow incidence angles) are desirable.

With this reasoning, the following baseline system parameters were selected for an initial PRF parametric analysis.

Parameter	**Value**
Altitude	500 km
Velocity	7613 m/s
Resolution	3 m
Antenna Length	6 m
Incidence Angle	45°
Tx Pulse Length	30 μs
Swath Width (on ground)	10 km

With these baseline parameters, the following PRF parametric analysis was done.
It should be noted that for the analysis which follows, no guard bands have been included, i.e., realistic designs include some margins for safety which have not been factored into the graphs that follow.

5.1.9 PRF versus Antenna Length

Figure 5.1.8.1 shows the variation in PRF availability as antenna length varies from under 3m to 10m. The PRF values that result in transmitter pulse eclipsing and nadir echo eclipsing are constant for all antenna lengths. The only PRF design constraint that varies with antenna length is PRF_{min} which relates to the requirement on adequately sampling the Doppler bandwidth of the signal.

The vertical axis (*PRF*) of Figure 5.1.9.1 varies from 0 to 10 kHz. This range of values was chosen to illustrate several points. As the PRF increases, the ranges of available PRFs shrinks to nothing. This figure also shows the upper bound on usable PRFs for the baseline system (PRF_{max} = 9331 Hz). The lower bound varies as a function of antenna length. For an antenna length of 6 m, PRF_{min} = 2538 Hz. Only the range of PRFs from 2500 Hz to about 5000 Hz is of interest, so subsequent graphs will be limited to this range which should make the graphs more readable. Figure 5.1.9.2 plots *PRF* versus antenna length with these new limits.

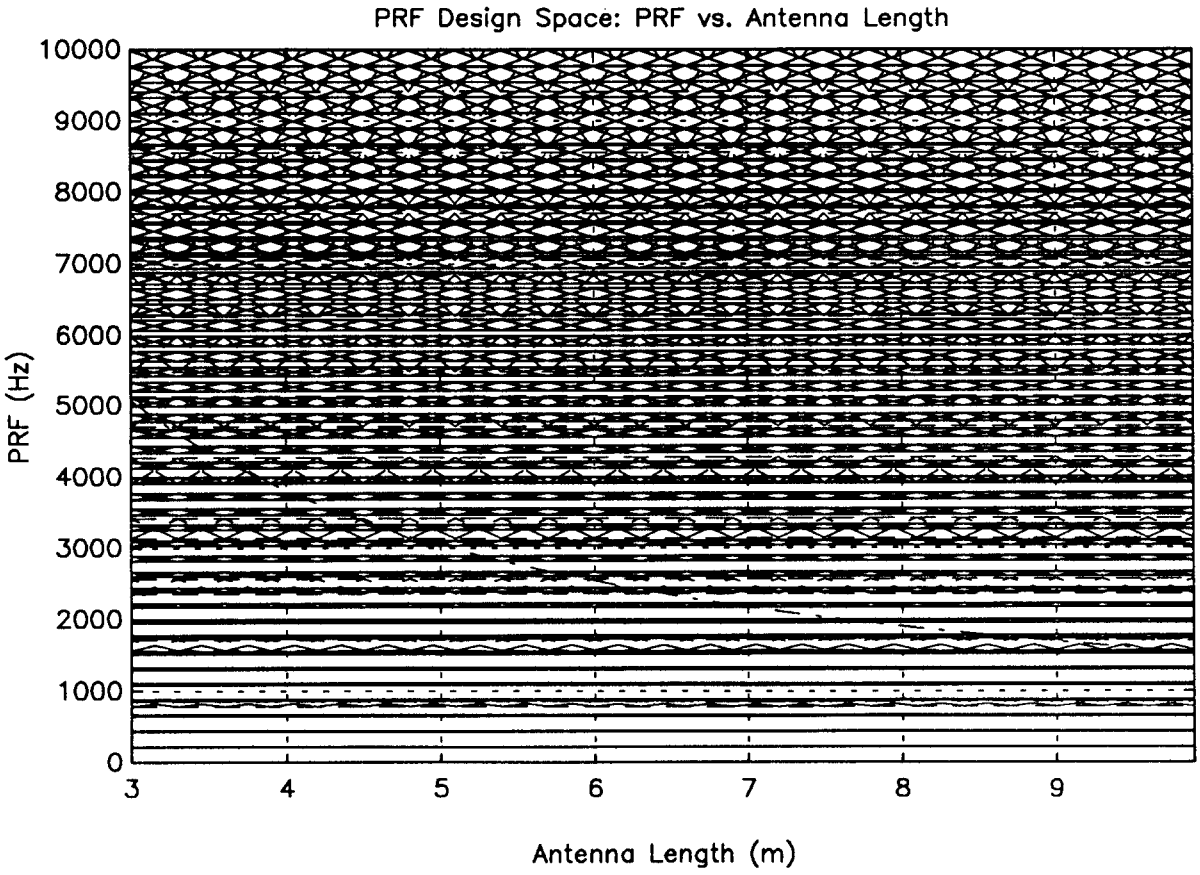

Figure 5.1.9.1 PRF vs. Antenna Length (full PRF range). Simulated system parameters: Altitude: 500 km, Velocity: 7613 m/s, Tx Pulse Length: 30.0 μs, Incidence Angle: 45°, Swath Width: 10 km.

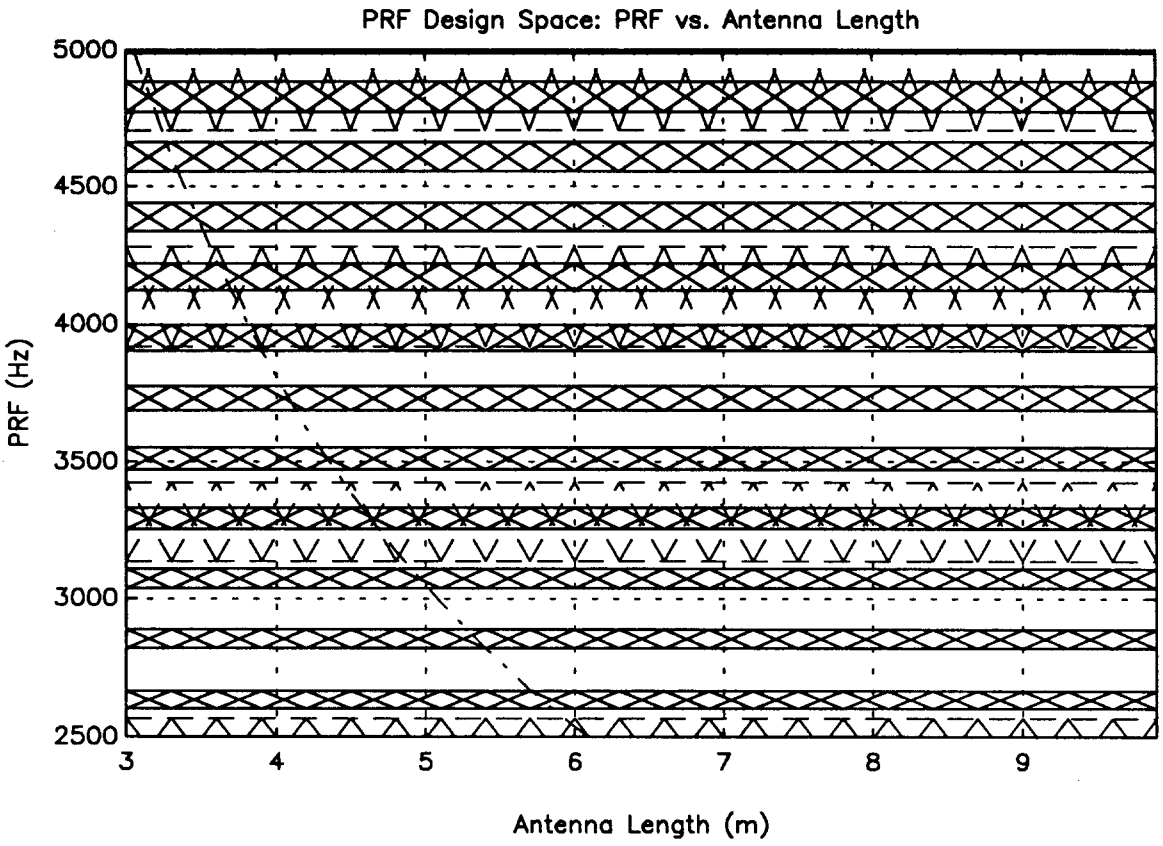

Figure 5.1.9.2: PRF vs. Antenna Length (reduced PRF range). Simulated system parameters: Altitude: 500 km, Velocity: 7613 m/s, Tx Pulse Length: 30.0 μs, Incidence Angle: 45°, Swath Width: 10 km.

5.1.10 PRF versus Transmitter Pulse Length

Figure 5.1.10.1 is a plot of PRF availability versus transmitter pulse length. Note that the upper bound (PRF_{max}) decreases with increasing transmitter pulse length. The bands of PRF unavailability due to transmitter pulse eclipsing and nadir echo eclipsing broaden with increasing transmitter pulse length. It is clear that pulse lengths larger that 100 μs are unusable.

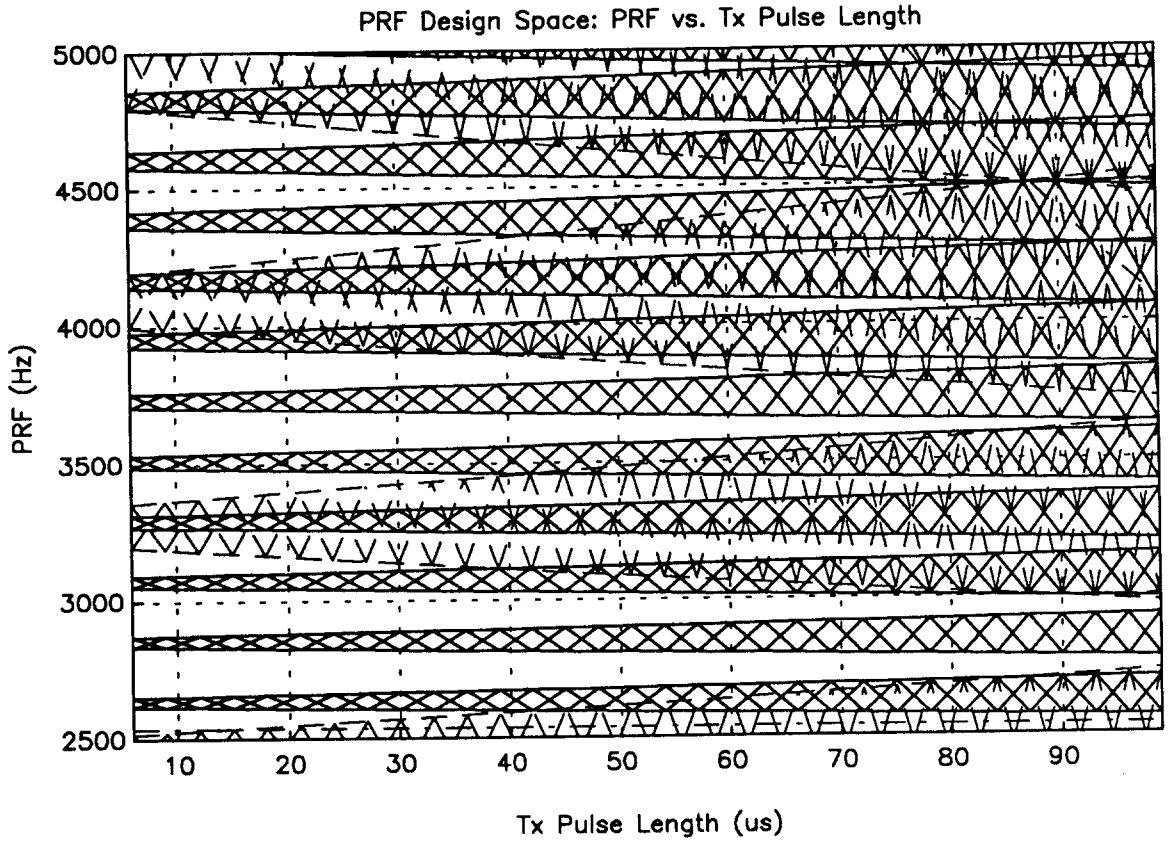

Figure 5.1.10.1: PRF vs. Transmitter Pulse Length. Simulated system parameters: Altitude: 500 km, Velocity: 7613 m/s, Antenna Length: 6.0 m, Incidence Angle: 45°, Swath Width: 10 km.

5.1.11 PRF versus Swath Width

Figure 5.1.11.1 shows the relationship between PRF availability and swath width on the ground. As in the case of transmitter pulse length, PRF_{max} decreases with increasing swath width. Also, the bands identifying unusable PRFs due to eclipsing by the transmitter pulse and the nadir echo broaden with increasing swath width. It is clear that there are no PRFs available to support swath widths of 50 km and larger.

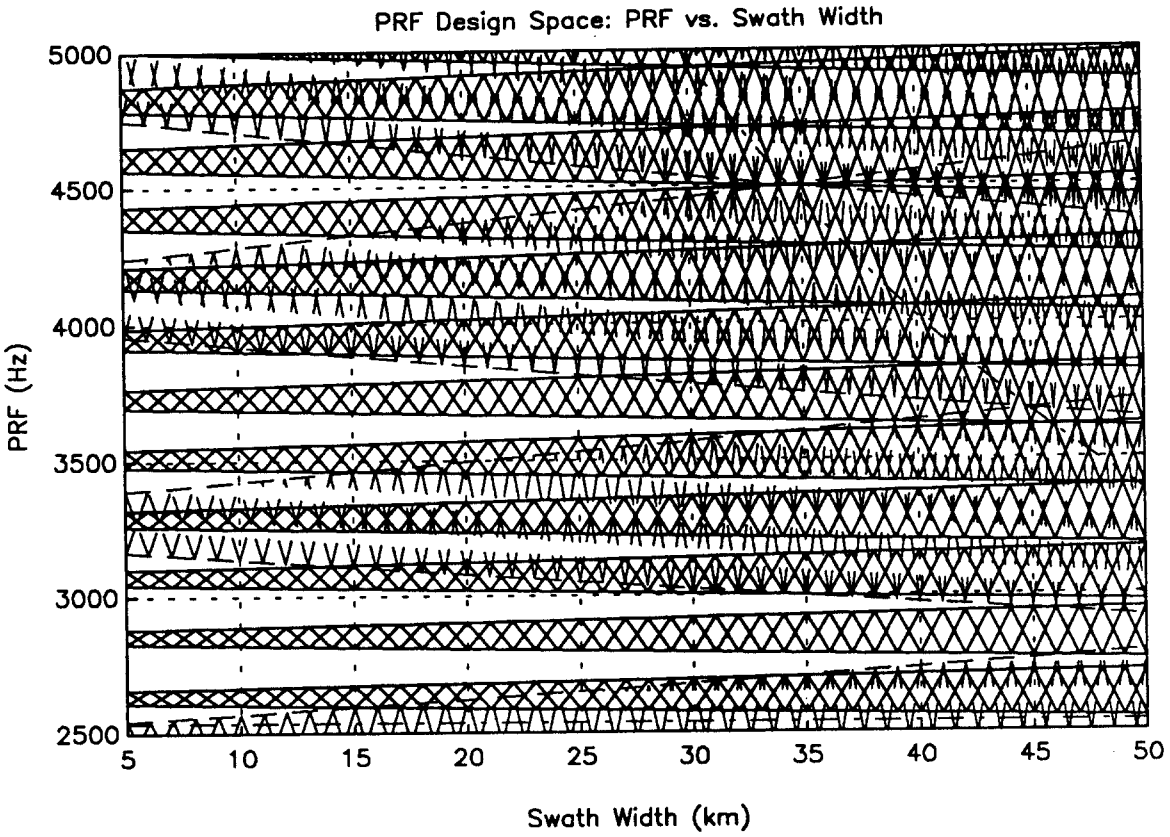

Figure 5.1.11.1: PRF vs. Swath Width (on ground). Simulated system parameters: Altitude: 500 km, Velocity: 7613 m/s, Antenna Length: 6.0 m, Tx Pulse Length: 30.0 μs, Incidence Angle: 45°.

5.1.12 PRF versus Altitude

Figure 5.1.12.1 shows how variations in radar altitude effects PRF availability. What is significant about this plot is that a useful PRF for an altitude of 500 km (3625 Hz, for example) is not appropriate for an altitude of 480 km. So if altitude variations occur (due to non-circular orbit, orbit decay, variations in elevation of the target) a new PRF would have to be implemented.

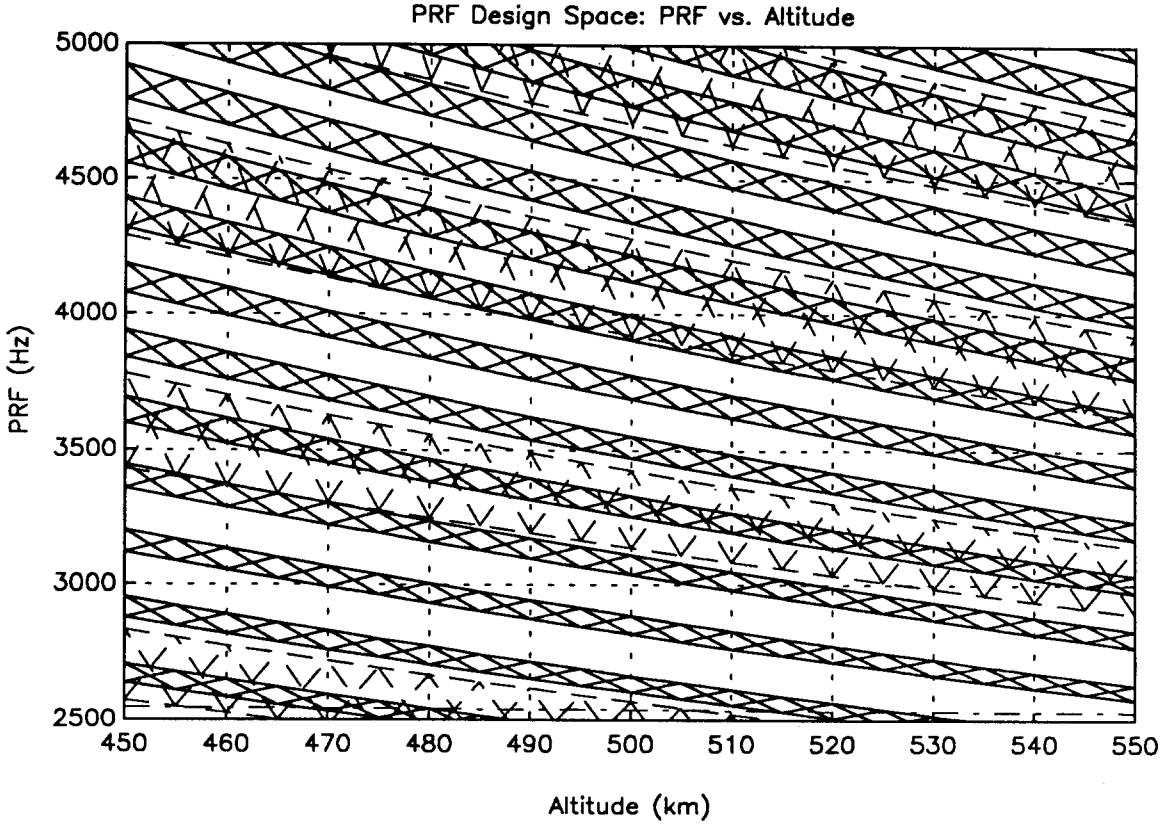

Figure 5.1.12.1 PRF vs. Altitude. Simulated system parameters: Antenna Length: 6.0 m, Tx Pulse Length: 30.0 μs, Incidence Angle: 45°, Swath Width: 10 km.

5.1.13 PRF versus Incidence Angle

Figure 5.1.13.1 illustrates the effect on PRF availability of changing incidence angles. Smaller incidence angles constrain the available PRFs less. There are no PRFs available to support incidence angles much larger than 70 degrees. Another bit of information that can be extracted from Figure 5.1.13.1 has to do with sensitivity to variations in incidence angle. The incidence angle is the angle from which the microwave energy arrives at the target as measured from vertical. Incidence angle variations would result from pointing errors at the radar. The margin for error is larger for smaller incidence angles.

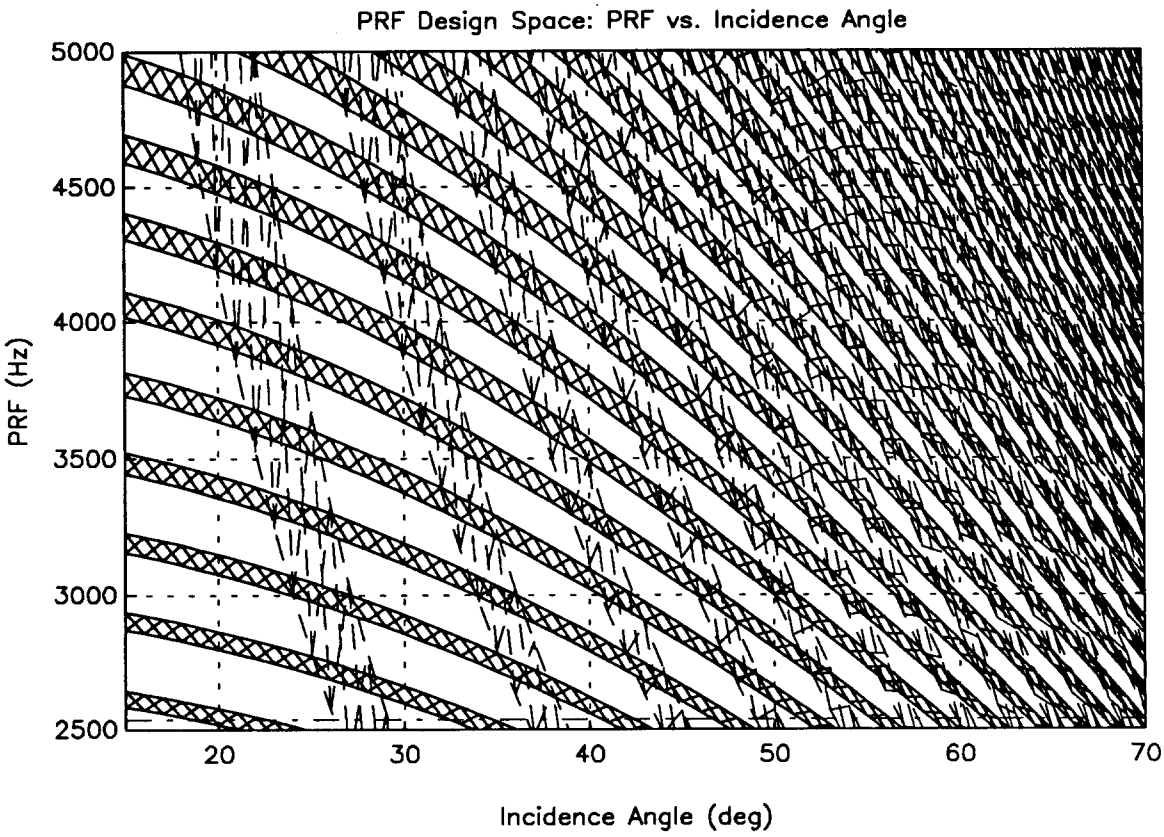

Figure 5.1.13.1: PRF vs. Incidence Angle. Simulated system parameters: Altitude: 500 km, Velocity: 7613 m/s, Antenna Length: 6.0 m, Tx Pulse Length: 30.0 μs, Swath Width: 10 km.

5.1.14 PRF versus Look Angle

Figure 5.1.14.1 shows how PRF availability varies with look angle. Look angle is the pointing angle of the antenna measured from nadir at the radar. Figure 5.1.43.1 would be more useful than Figure 5.1.13.1 for evaluating the effect of antenna pointing errors since the relationship between look angle and incidence angle is a function of altitude. Figure 5.1.14.2 shows this relationship.

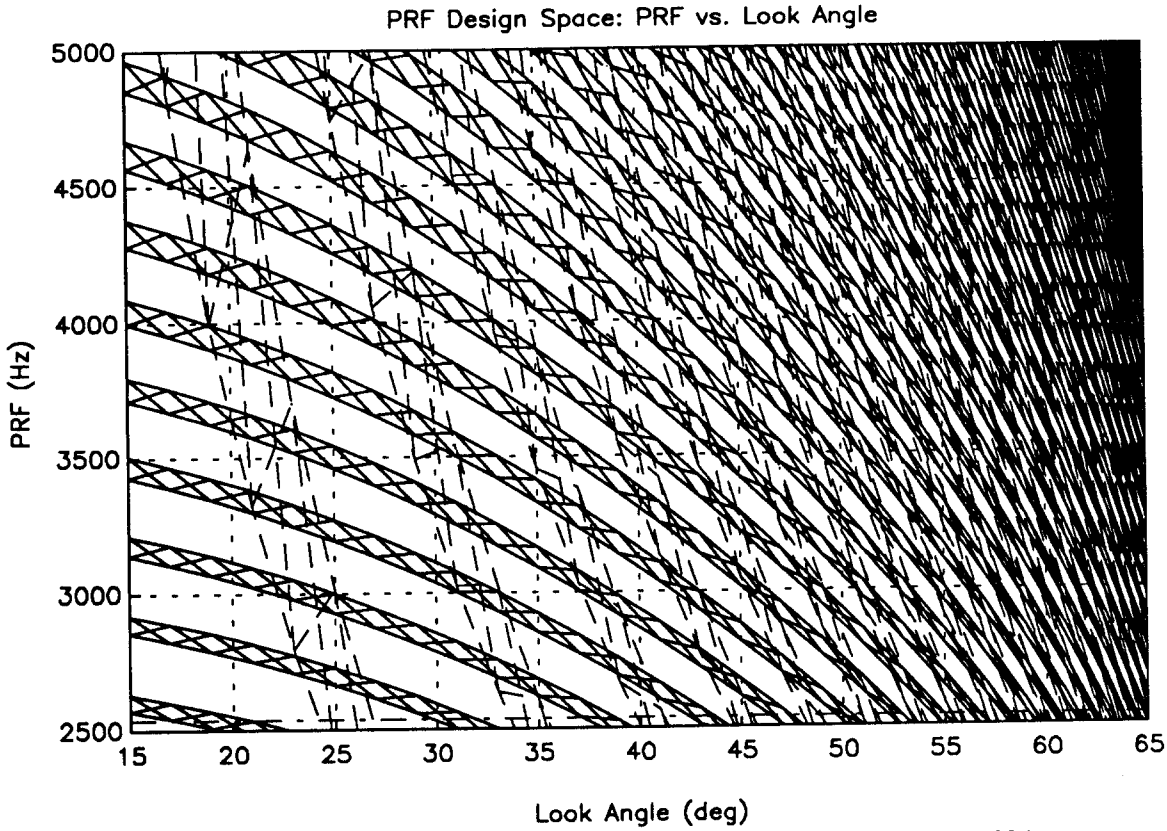

Figure 5.1.14.1: PRF vs. Look Angle. Simulated system parameters: Altitude: 500 km, Velocity: 7613 m/s, Antenna Length: 6.0 m, Tx Pulse Length: 30.0 μs, Swath Width: 10 km.

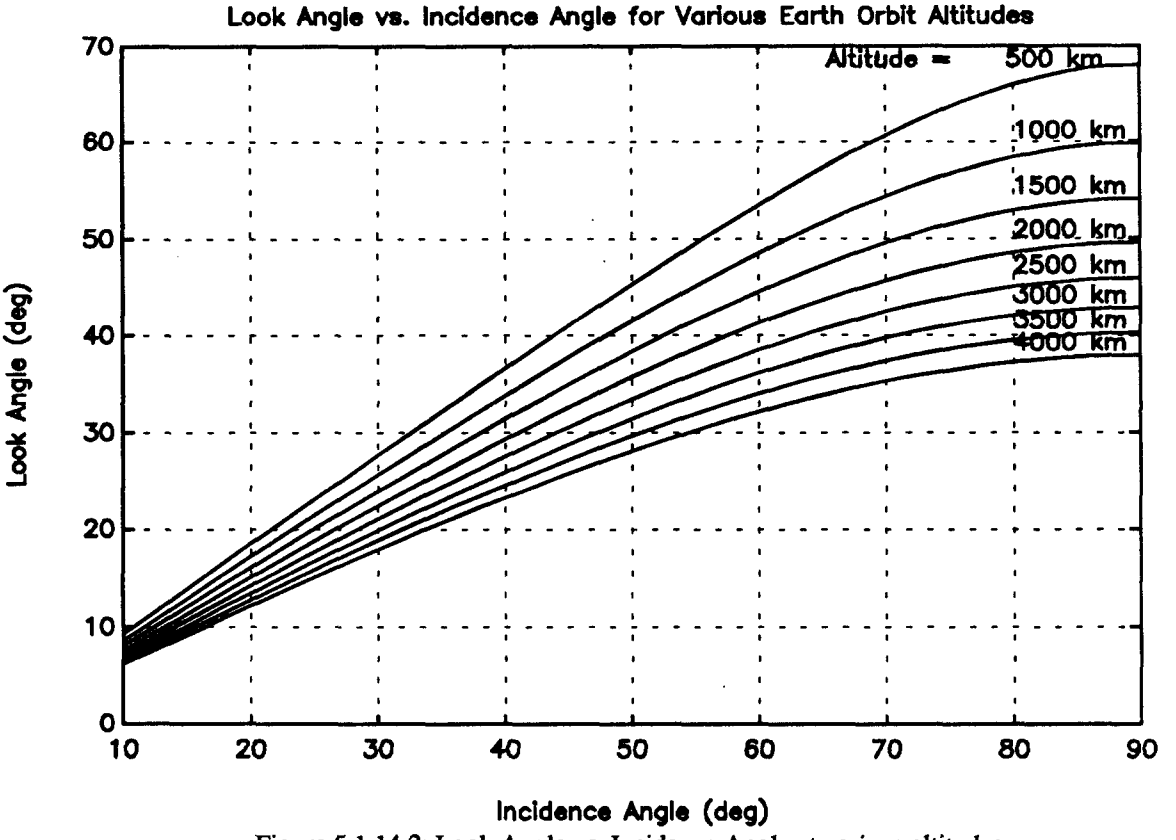

Figure 5.1.14.2: Look Angle vs. Incidence Angle at various altitudes

5.1.14 Discussion and Summary

From the information presented above, a reasonable choice for PRF would appear to be 3625 Hz. This is avoids eclipsing of the scene echo signal by the 17th and 18th transmitter pulses, avoids the nadir echo from the 5th and 6th transmitter pulses, and oversamples the Doppler bandwidth of the scene echo by a factor of 3625/2538 or 1.43.

From the baseline incidence angle of 45° (look angle of 40.97°), a maximum roll angle error of ± 1° could be tolerated. From the nominal 500 km altitude, variations of ± 10 km could be tolerated. If these error budgets are too restrictive, then compromises in transmitter pulse length or swath width would need to be made. Another alternative would be to decrease the incidence angle, but incidence angle affects the usefulness of the sensor in viewing various classes of targets. Therefore, this compromise would require an analysis of the impact on target/image characteristics.

The dependency of usable PRFs on the radar system parameters has been presented. It was shown that the lower bound on the PRF needed to adequately sample the Doppler bandwidth is radar frequency independent, but is dependent on antenna length, which is related to azimuth resolution in stripmap operating mode.

To analyze eclipsing of the scene echo by the transmitted pulse and the nadir echo, timing calculations were presented and the results were shown graphically. The effects of variations of each of the various system parameters were presented.

A PRF of 3625 Hz was recommended based on the assumed system baseline parameters and a number of compromises. For this choice of PRF, an antenna pointing error in roll of ± 1° could be tolerated. Similarly, a variation in altitude of ± 10 km could be tolerated.

5.2 Multiple Phase-Center/Multi-Beam SAR Systems

Conventional SAR theory requires a high PRF for fine azimuth resolution and a low PRF for wide swath widths. These requirements constitute a SAR design trade-off, particularly in the case of satellite borne SAR. Currie and Hall [22] propose a technique that allows "simultaneous wide-swath high-resolution SAR imagery" using "a combination of low PRF and multiple azimuth beams to provide the high Doppler sampling rate needed for high resolution imaging." System implications of using this (these) technique(s) for a satellite borne SAR will be explored.

In conventional SAR, a long synthetic array antenna (length L_a) is composed of many individual elements. What is unique about SAR is that this synthetic antenna is not realized simultaneously, rather it is a mathematical construct composed of a single real antenna (length D_a) whose output is coherently sampled as it moves along the synthesized antenna length. At each position along the array a pulse is transmitted and the returning energy is sampled. Samples are collected along the synthetic array at spatial intervals of $D_a/2$ (or less). Therefore the lower bound on pulse repetition frequency (PRF) is related directly to the platform velocity, V_{st}, as:

$$PRF \geq \frac{2 \cdot V_{st}}{D_a} \tag{5.2.1}$$

Additional constraints on the PRF are imposed to avoid blind ranges (transmitting while receiving) and to avoid energy from the nadir return, which would corrupt the desired return signal. These constraints were given in the previous section in equations (5.1.3.13), (5.1.4.1), and (5.1.5.2).

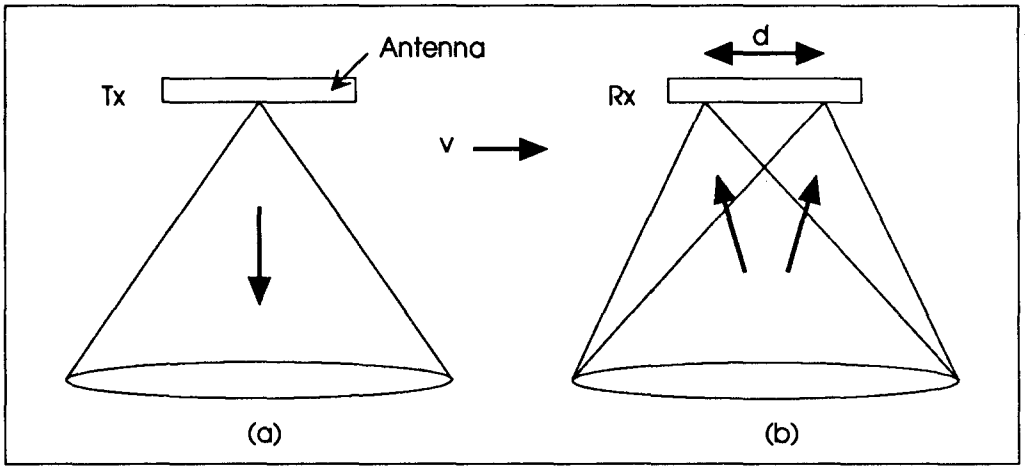

Figure 5.2.1: Multiple azimuth beam SAR: (a) transmit into single broad beam; (b) receive beams with two phase centers ($N_B = 2$) displaced by d.[23]

In the technique proposed by Currie and Hall [22], referred to as the Multiple Phase Centre Multi-Beam System, the system PRF is reduced by a factor N_B by simultaneously sampling a pulse return on N_B beams having phase centers that are displaced in the along-track direction (see Figure 1). The receive beams are assumed to be coincident in the far-field region.

According to [22], after combining the N_B sets of returns "a properly sampled phase history will be obtained."
This variation on the conventional SAR approach will introduce additional phase components for the samples from the displaced phase centers that must be corrected prior to combining into a single phase history record. Satellite borne SAR system implications relating to this technique, including this phase correction, will be explored.

Some assumptions were made to facilitate the analysis that follows. These are:

- a simple straight-line flight path is assumed;
- the transmit pulse is sufficiently short in duration so that phase variations during transmit and receive intervals are negligible;
- the squint angle is 90°, i.e., the antenna beam is pointed perpendicular to the velocity vector;
- the effects of Earth rotation are ignored.

5.2.1 Aperture Synthesis Geometry

Aperture synthesis occurs over the interval $-T_a/2 \le t \le T_a/2$ where T_a is the aperture integration period and L_a is the synthetic aperture length. The range to the target at mid-aperture is R. Figure 2 illustrates the basic aperture synthesis geometry.

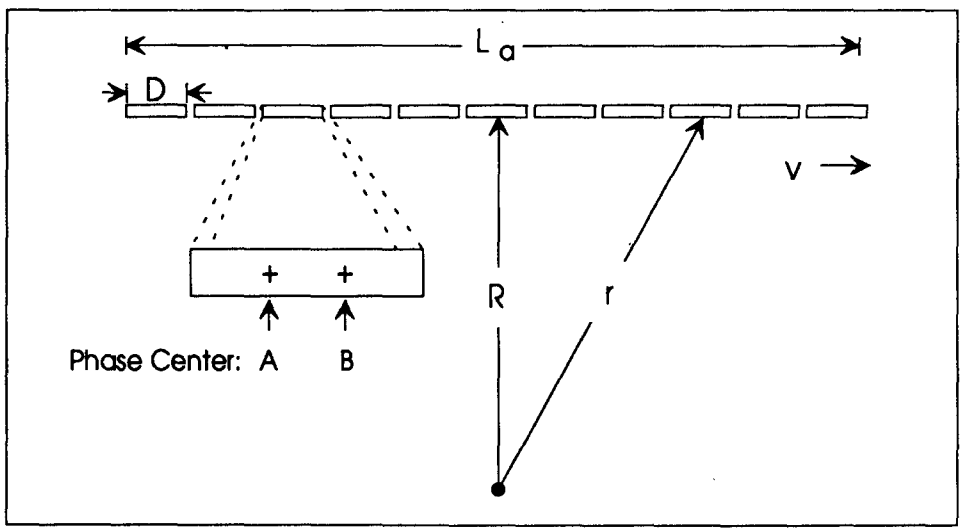

Figure 5.2.1.1 Data collection geometry for synthetic aperture formation. Also shown are the displaced phase centers on the real antenna aperture.

5.2.2 Phase History of Single Phase Center Beam

For a conventional SAR with a single antenna phase center, the one-way range from the antenna phase center to the target is:

$$r(V_{st} \cdot t) = \sqrt{R^2 + (V_{st} \cdot t)^2} \qquad (5.2.2.1)$$

where:

$r(x)$ - is the range to the to mid-aperture target as a function of x

x - is the distance along the aperture (from the center of the aperture)

Recognizing that $R \gg L_a/2$, this expression may be simplified using a series expansion to yields:

$$r(V_{st} \cdot t) \approx R + \frac{(V_{st} \cdot t)^2}{2 \cdot R} \qquad (5.2.2.2)$$

The phase associated with this one-way travel (ignoring the constant phase term) is:

$$\phi_{1-way}(V_{st}\cdot t)=\frac{\pi\cdot(V_{st}\cdot t)^2}{\lambda\cdot R} \tag{5.2.2.3}$$

The position of the real antenna phase center moves during the interval between transmit and receive as the speed of light is not infinite. For a system transmitting and receiving from a single antenna phase center (phase center A), the received phase during aperture synthesis is:

$$\phi_{AA}(V_{st}\cdot t)=\phi_{tx}(V_{st}\cdot t-V_{st}\cdot\tau_D)+\phi_{rx}(V_{st}\cdot t)=\frac{\pi\cdot\left[(V_{st}\cdot t-V_{st}\cdot\tau_D)^2+(V_{st}\cdot t)^2\right]}{\lambda\cdot R} \tag{5.2.2.4}$$

which simplifies to:

$$\phi_{AA}(V_{st}\cdot t)=\frac{2\cdot\pi\cdot\left[V_{st}^2\cdot t^2-V_{st}^2\cdot t\cdot\tau_D+V_{st}^2\cdot\tau_D^2/2\right]}{\lambda\cdot R} \tag{5.2.2.5}$$

Here τ_D is the two-way propagation time ($\tau_D = 2\cdot R/c$) which is nominally constant over the aperture. In azimuth sampling at the PRF, samples are collected at spatial intervals of X, where $X = V_{St}/PRF$, (m). Note: to satisfy the Nyquist criteria, X must be constrained such that $X \le D_a/2$, where D_a is the real antenna length. The received phase of the next azimuth sample, referenced to the same time as before, is:

$$\phi_{AA}(V_{st}\cdot t+X)=\phi_{tx}(V_{st}\cdot t-V_{st}\cdot\tau_D+X)+\phi_{rx}(V_{st}\cdot t+X) \tag{5.2.2.6}$$

or:

$$\phi_{AA}(V_{st}\cdot t+X)=\frac{2\cdot\pi\cdot\left[V_{st}^2\cdot t^2-V_{st}^2\cdot t\cdot\tau_D+V_{st}^2\cdot\tau_D^2/2+2\cdot V_{st}\cdot t\cdot X-V_{st}\cdot\tau_D\cdot X+X^2\right]}{\lambda\cdot R} \tag{5.2.2.7}$$

5.2.3 Phase History of Displaced Phase Center Beams

Now consider the case with two phase centers A and B displaced by a distance d. Let phase center A be used for transmit and phase center B be used for receive. The received phase during aperture synthesis is:

$$\phi_{AB}(V_{st}\cdot t)=\phi_{tx}(V_{st}\cdot t-V_{st}\cdot\tau_D)+\phi_{rx}(V_{st}\cdot t+d) \tag{5.2.3.1}$$

or:

$$\phi_{AB}(V_{st}\cdot t)=\frac{2\cdot\pi\cdot\left[V_{st}^2\cdot t^2-V_{st}^2\cdot t\cdot\tau_D+V_{st}^2\cdot\tau_D^2/2+V_{st}\cdot t\cdot d+d^2\right]}{\lambda\cdot R} \tag{5.2.3.2}$$

Comparing expressions for $\phi_{AA}(V_{st} \cdot t)$ and $\phi_{AB}(V_{st} \cdot t)$, letting $d = 2 \cdot X$, the two expressions are similar. Taking the difference we see that:

$$\Delta\phi(X) = \phi_{AA}(V_{st} \cdot t + X) - \phi_{AB}(V_{st} \cdot t) = -\frac{2 \cdot \pi \cdot \left[V_{st} \cdot \tau_D \cdot X + X^2\right]}{\lambda \cdot R} \qquad (5.2.3.3)$$

which is a constant phase difference during the aperture integration period. By adding a phase offset to the data collected at this offset phase center, the two sets of data can be combined to form a single "properly sampled phase history."

Therefore, prior to combining these two azimuth samples to form a complete phase history, a constant phase shift must be applied to samples collected from the displaced phase center.

Example:

To illustrate the concepts described above, consider the following scenario. A satellite borne SAR is desired to operate with the following system parameters:

Example Satellite SAR System Parameters

altitude = 500 km	SAR mode = strip map	incidence angle = variable
velocity = 7613 m/s	swath width = 100 km	azimuth resolution = 3 m

Figure 5.2.3.1 shows PRF availability versus incidence angle for the parameters listed. The shaded bands represent unavailable PRFs due to transmitter eclipsing (solid lines) or nadir echo (dashed lines). PRFs outside these bands are usable provided they satisfy the Nyquist criteria.

According to conventional SAR theory, to operate in strip map mode, the antenna length should be less than or equal to twice the desired azimuth resolution. Let the antenna length be 6.1 m. To satisfy the Nyquist criteria the PRF must be greater than 2496 Hz but less than 2367 Hz to adequately sample the returning pulse. This inequality clearly prohibits operation of a conventional SAR with these parameters. Alternatives would be to reduce the swath width (and increase the upper limit on the PRF) or to degrade the azimuth resolution (and decrease the lower limit on the PRF). Also, it is seen in Figure 3 that PRF availability disappears as PRFs approach 3000 Hz but for PRFs below about 2000 Hz, PRF availability expands substantially. By using the displaced phase center antenna scheme, this otherwise impossible system is realizable.

Let the effective PRF be 3000 Hz. A sample spacing of 2.538 m (X) represents a 20% over sampling beyond the Nyquist requirement of $D_a/2$ or 3.05 m. By utilizing a two-phase-center antenna, the PRF could be reduced by two to a value of 1500 Hz. A longer antenna with phase centers separated by 5.075 m is required to emulate the conventional SAR implementation. Prior to combining the two sets of azimuth samples to form a complete phase history, a constant phase shift, $\Delta\phi$, must be applied to the data collected from phase center B. For a radar frequency of 1.275 GHz (SEASAT) the value of $\Delta\phi$ is 0.0038 radians or 0.22° and for a radar frequency of 15 GHz the value of $\Delta\phi$ is 0.044 radians or 2.52°.

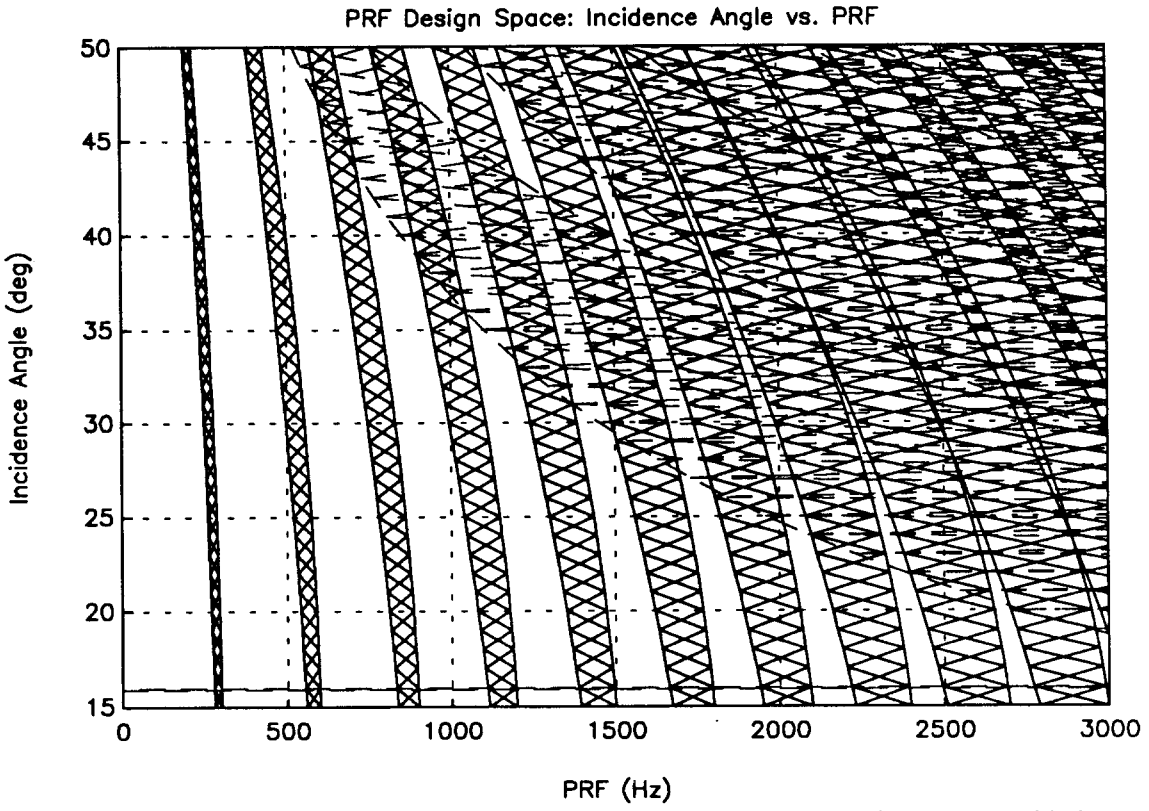

Figure 5.2.3.1: PRF availability diagram as a function of incidence angle for a system with the following parameters: altitude = 500 km, velocity = 7613 m/s, swath width = 100 km, Tx pulse length = 40 μs. The shaded bands represent unavailable PRFs due to transmitter eclipsing (solid lines) or nadir echo (dashed lines).

5.2.4 Implementation Challenges

Disadvantages associated with this multi-phase center scheme include:

- requires an antenna that is physically longer;
- requires that a separate receiver channel (from the antenna to the A/D converter) be provided for each phase center;
- requires separate processing of data from each phase center prior to combining into a complete phase history.

5.2.5 Antenna Design

The antenna length is directly driven by the need for displaced phase centers. This disadvantage is unavoidable and is the price to be paid for the added capability of wide-swath imaging at fine resolution. In the example given above, the single-phase-center antenna had a length of 6 m, and the displacement required for the dual-phase-center antenna was 5.075 m. Figure 5.2.5.1 is a sketch of each of these arrays, showing that to implement the dual-phase-center system, the two receive apertures must overlap to maintain the same aperture area as before. The along-track antenna length grew from 6.1 m to approximately 11 m, not quite doubling.

As shown in Figure 5.2.5.1, the subarrays overlap by about 1 m. The elements in this overlapped region are shared by both subarrays. RF output from elements in this common region will be used in both

beamforming networks that connect all of the elements in each subarray to form the desired receive antenna patterns.

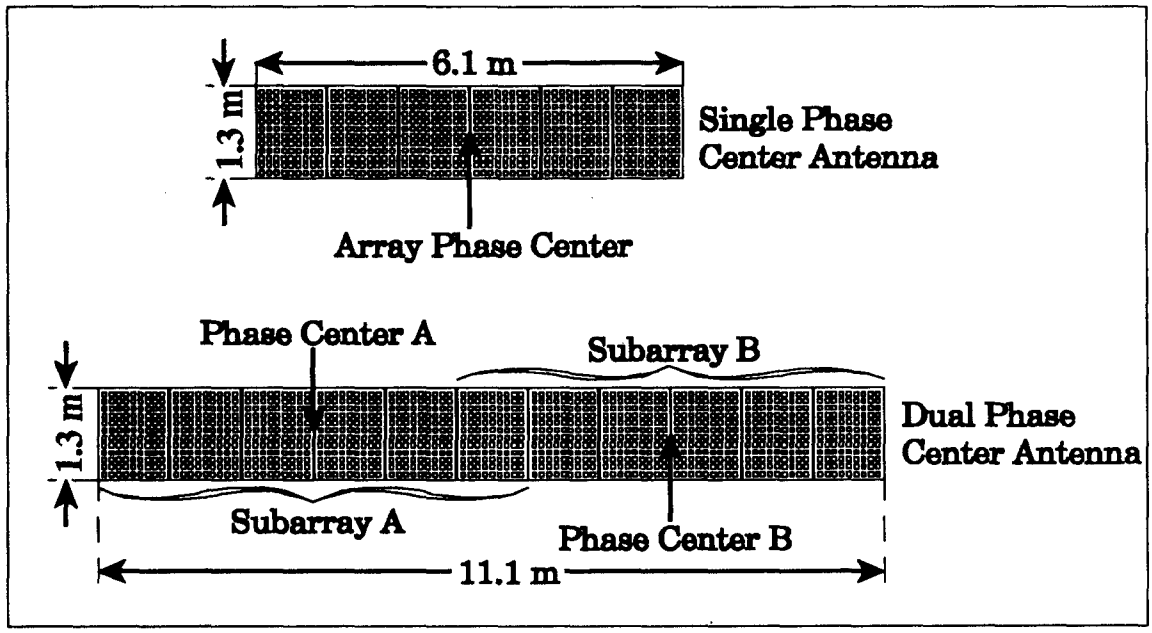

Figure 5.2.5.1: Sketch comparing the size of a single phase antenna with a two phase center antenna.

If T/R modules are used in the antenna design, it is desirable to use the entire array for transmit to output as much RF energy as possible. With this longer antenna, steps must be taken to defocus the transmit beam to broaden the beamwidth so the region of interest is properly illuminated. This defocusing of the entire array means that separate beamforming networks are necessary for transmit and receive. If the entire antenna is used during transmit, then the phase center of the transmit antenna will be at the mid-point of the full antenna.

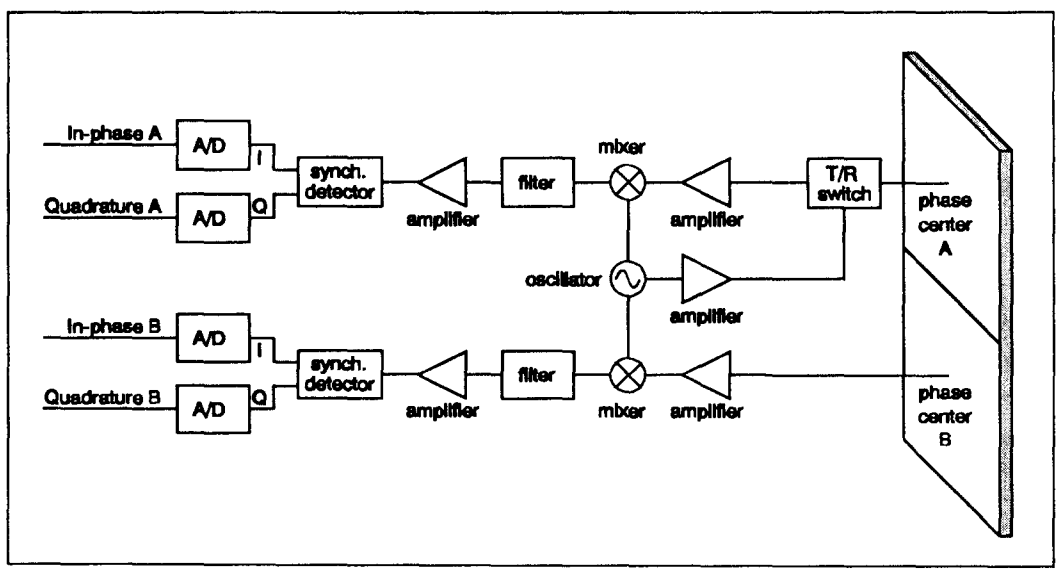

Figure 5.2.5.2: Simplified system block diagram for a two phase center SAR system using only one subarray during transmit.

If instead of T/R modules, a single power amplifier (e.g., a TWTA) was used to provide the transmitter output, then just one of the subarrays could be used. The desired transmit antenna pattern would result. Figure 5.2.5.2 illustrates this situation.

In either case, the requirement for a longer antenna does not result in higher gain for either the transmit or the receive antennas.

5.2.6 Receiver Design

As mentioned above, separate receiver channels (from the antenna port to the output from the A/D converters) are required to process data from each phase center simultaneously. The amplitude and phase characteristics of each receiver channel must be closely matched to produce good quality images. Mismatches in amplitude or phase will result in anomalous image components appearing at f_S/N_B (f_S is the azimuth sample frequency and N_B is the number of phase centers and receiver channels). Image quality requirements will dictate the level of mismatch in amplitude and phase that can be tolerated

One approach for matching the channels is to actively monitor the amplitude and phase characteristics of each channel through the use a calibration signal. As the receiver is idle during the transmit interval, this time is available for calibration purposes. A signal could be injected into the receiver front end as close to the antenna as possible without affecting the transmit operation. This signal would then be sampled in the signal processor and the output from each channel compared with a reference. Any variation could then be corrected in the digital processing. As mentioned earlier, each channel must have a phase term applied to it to remove the effects introduced by the displaced phase center geometry. A complex amplitude and phase correction term could simply be added with this complex phase term prior to multiplication with the data.

The challenge would be to calculate the amplitude and phase correction term in the time available. Assuming the characteristics of the receiver channels do not rapidly vary, then a calibration sample need only be collected and processed periodically.

An approach that incorporates commutation between the receiver channels on a pulse-to-pulse basis or on a random basis was investigated for the case of two phase centers. Figure 5.2.6.1 shows the results for three cases (a) no commutation, (b) simple pulse-to-pulse commutation, and (c) random commutation. What is shown is the result of an FFT of a single complex tone. An amplitude error of -0.3 dB and a phase error of 1° are applied to one of the two channels for each sample. For the case of no commutation, the same channel always has the errors in its samples, e.g., the odd numbered samples are "ideal" and the even numbered samples have errors In simple pulse-to-pulse commutation, in the first pair of samples the error is in the even numbered sample, for the next pair of samples the error is in the odd numbered sample, etc. For random commutation, for each pair of samples, the one that has the error applied is determined randomly. In each plot the spectrum of an "ideal" waveform is plotted as a dotted line for reference and each plot is normalized to this reference.

In the simulation that was performed, the simulated PRF was 3000 Hz (f_S) and the sinusoid had a frequency of 403 Hz. No window function was applied to reduce the sidelobes.

For the case of no commutation (a), a spur of -25.16 dB appears at -1093 Hz and the mainlobe has a peak of -0.16 dB relative to the ideal case.

For simple pulse-to-pulse commutation (b), a spur of -6.32 dB appears at -1093 Hz and the mainlobe has a peak of -6.32 dB relative to the ideal case.

In random commutation (c), the energy is distributed across the spectrum with the peak spur being about -22.22 dB and the mainlobe has a peak of -6.32 dB relative to the ideal case.

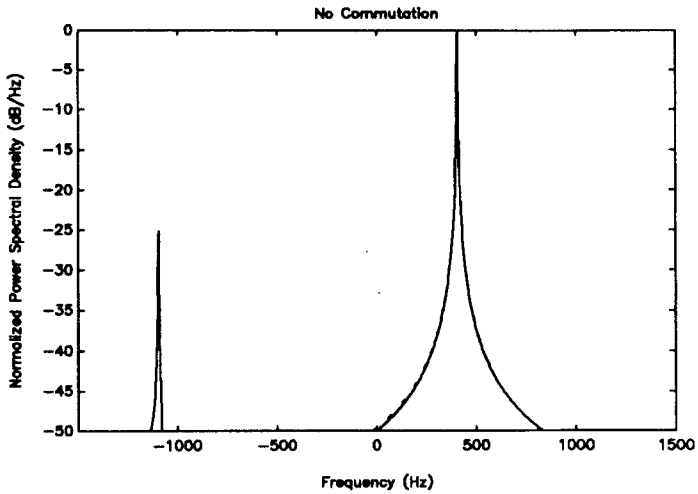

Figure 5.2.6.1 (a)

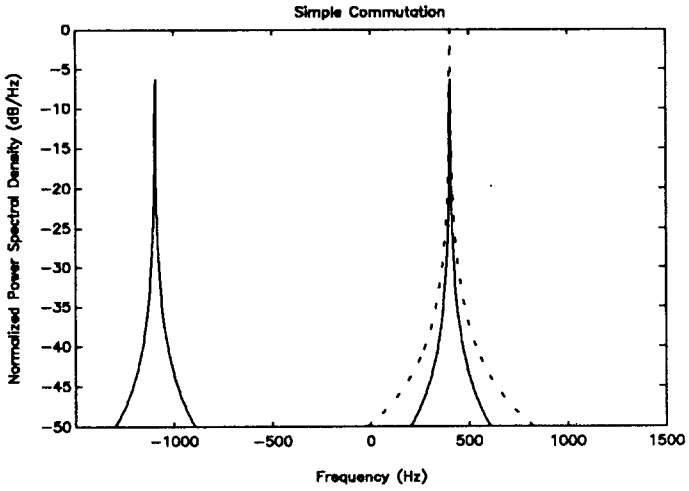

Figure 5.2.6.1 (b)

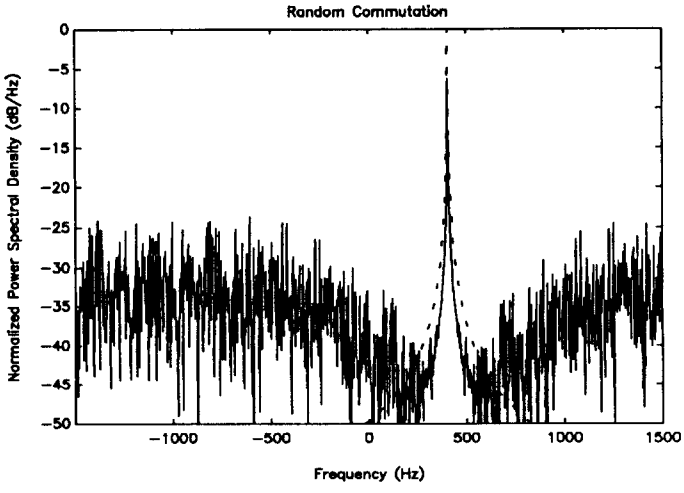

Figure 5.2.6.1 (c)

Figure 5.2.6.1: Simulation results for two receiver channel system with an amplitude difference of -0.3 dB and a phase difference of 1°. Three cases shown: (a) no commutation, (b) simple pulse-to-pulse commutation, and (c) random commutation. Dotted line represents performance for system with no errors.

System performance is better if no commutation is involved.

5.2.7 Effect on Transmitter Peak Power

The goal of this effort is to effectively reduce the system PRF to allow imaging of wide swaths. Since the transmitter pulse width is not being increased, the transmitter peak power must increase accordingly. If T/R modules are used in the antenna design, the transmitter peak power is directly coupled to the number of T/R modules. Therefore, if the PRF is effectively halved, then the number of T/R modules must double to maintain a constant average transmitter power. Fortunately, the antenna length almost doubles at the same time so that the T/R module spatial density does not dramatically increase. For more details refer to section 5.4.3.

5.2.8 Summary of Multiple Phase-Center/Multi-Beam SAR Systems

The multiple-phase-center approach will permit simultaneous wide-swath and high-resolution SAR imagery from a spaceborne system. The system PRF is effectively reduced by the number of antenna phase centers used. Prior to combining data collected from each phase center to form a complete phase history, a constant phase shift must be applied to the data. The amount of phase shift depends on the system geometry (range, R, and the displacement between the phase center and the reference), the system velocity, and the radar wavelength.

Implementation in system hardware requires a physically longer antenna and a complete receiver channel for each antenna phase center. To achieve a greater reduction in system PRF (to image a wider swath) the antenna must be longer. Longer antennas are more difficult to assemble and to calibrate. All of the receiver channels must have the same amplitude and phase characteristics to prevent image degradation. A calibration technique involving sampling and digitally processing a reference signal to obtain a digital compensation factor for each channel may be necessary.

A greater transmitter peak power will be necessary to compensate for the reduced PRF. This translates into more T/R modules if T/R modules are utilized.

This solution to the problem involves additional system complexity. However, when viewed as perhaps the only way to achieve simultaneous wide-swath and high-resolution SAR imagery from a satellite borne SAR, for the added complexity, an invaluable capability is gained.

5.2.9 Further Study

This brief look into this multiple phase center multi-beam SAR system is not exhaustive. Examined was the feasibility of the concept and the implications for hardware complexity. Not addressed were operation in squint mode; practical limits on antenna length and data rates; and image formation processing challenges for wide-swath, high-resolution satellite borne imagery. Each of these topics deserves analysis to confirm feasibility.

5.3 SAR Processing Issues

This section discusses some issues that are important to consider when processing SAR data from a spaceborne platform. This section is meant to point out issues which are important in spaceborne SAR that may not be as important in airborne SAR. In particular, the following topics are covered:

1) pulse length vs. swath width issues for range processing
2) Doppler for spaceborne SAR
3) a rough outline of line-by-line processing and why it is often used
4) azimuth resolution considerations for a circular geometry

5.3.1 Range Processing

This section discusses some of the range processing issues involved in spaceborne SAR and describes why JPL and others sample the demodulated chirp signal directly rather than sampling the deramped video signal. In particular, it is noted in this that deramp processing has problems with large range-swath time to transmitter pulse time ratios. However, an important feature of deramp processing is that the A/D sample rate can be less than that of the demodulated chirp signal, by sacrificing range-swath.

Typically, in airborne platforms, the range-swath times are nearly the same as the transmitter pulse time. In spaceborne SARs, the range-swath times are typically much larger than the pulse times. Figure 5.3.1.1a-b illustrates the received linear frequency modulated (LFM or "chirp") waveforms for each case. In the figure τ_p is the transmitted pulse length, γ_{RF} is the chirp rate, and τ_w is the time it takes the pulse to travel across the range swath and back:

$$\tau_w = \frac{2 \cdot (R_f - R_n)}{c} \qquad (5.3.1.1)$$

where:
- c - is the speed of light
- R_f - -is the far range
- R_n - is the near range

One technique that is used for range processing when an LFM signal is transmitted is referred to as "deramping", "dechirping", or sometimes "stretch radar" processing (see Chapt. 10 in [21], [17], or [65]). This processing involves mixing the return signal with a delayed version of the transmitted chirp and taking the Fourier transform of the difference frequency portion of the resulting signal. Figure 5.3.1.2a-b illustrate the results after "dechirping" the received pulse.

For the deramp processing, the minimum required A/D sample spacing is given as:

$$T_F = \frac{1}{BW_{DR}} = \frac{1}{\gamma_r \cdot \tau_w} \qquad (5.3.1.2)$$

where:
- T_F - is the A/D sample spacing for Nyquist rate sampling
- BW_{DR} - is the bandwidth of the deramped signal
- γ_r - is the radar signal chirp rate
- τ_w - is the swath width time given in equation (5.3.1.1)

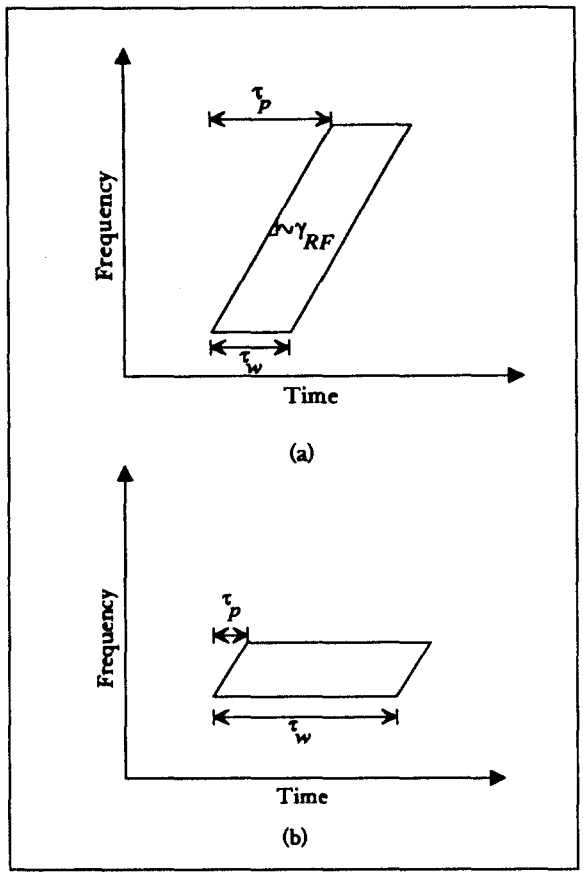

Figure 5.3.1.1: Received Chirp Waveforms
(a) airborne, (b) spaceborne

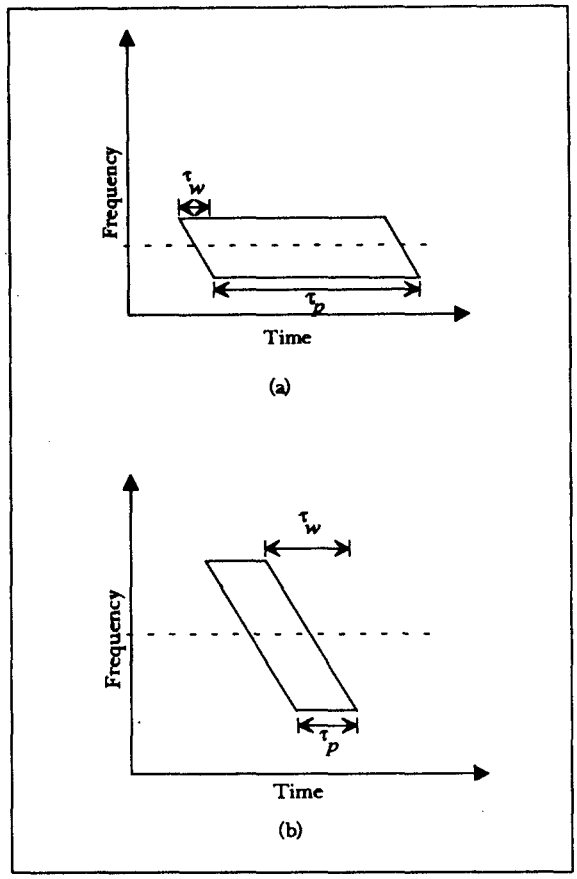

Figure 5.3.1.2: Received Dechired Waveforms
(a) airborne, (b) spaceborne

It should be noted that the single-sided bandwidth is being used in this section, which assumes quadrature (I and Q) sampling. If the real video signal is sampled, then the bandwidth must at least double and the A/D sample time would be cut in half.

A problem in deramp range processing, pointed out in [17] and [21], is that a signal-to-noise (SNR) penalty is paid if the same integration period is used for all ranges. According to [17], the processing loss is given by:

$$Loss = \left(\frac{\tau_p}{\tau_I}\right) \cdot \left[1 - \frac{\tau_n}{\tau_I}\right]^{-2} \qquad (5.3.1.3)$$

where:

τ_p - is the pulse length

τ_I - is the integration time

τ_n - is the portion of time that noise (rather than signal) is integrated in during processing

Figure 5.3.1.3 illustrates the problem. As the ratio of the pulse length to the swath time gets smaller the loss becomes worse due to the fact that more noise is included during integration. The loss is a function of range. In addition, a window is typically applied to the data for the full integration time. Since data may not be present during this whole time, the impulse response can suffer distortion (typically higher sidelobes). This distortion is worse at the far and near ranges.

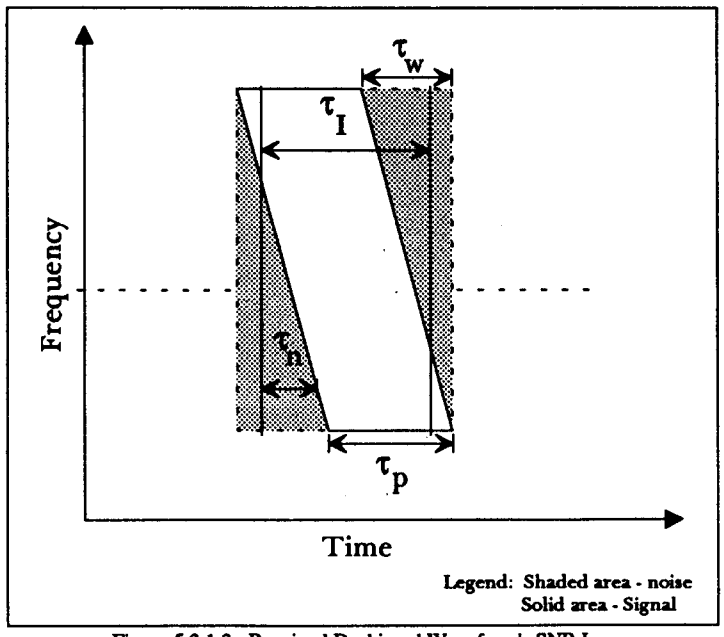

Figure 5.3.1.3: Received Dechirped Waveform's SNR Loss

An alternative to deramp processing is matched filter (or correlation) processing. Often this is implemented as a fast convolution. Matched filtering permits the full pulse length to be used for integration improving the SNR. However, the A/D sampler must run at the full bandwidth of the chirped waveform for Nyquist sampling, i.e.,

$$T_F = \frac{1}{BW_{MF}} = \frac{1}{\gamma_r \cdot \tau_p} \qquad (5.3.1.4)$$

where:

BW_{MF} - is the matched filter bandwidth
γ_r - is the chirp rate
τ_p - is the pulse length
T_F - is the A/D sample time

As an example, SEASAT used had an approximate chirp rate of γ_r = 0.56 MHz/μsec, a pulse length of 33.8 μs,and a 37 km slant-range swath width i.e., τ_p=33.8 μs, and τ_w=(2·37 km)/c, or τ_w=246.7 μs. The A/D sample rate for the deramp case is 138.35 MHz and for the matched filter case is 19 MHz. Figure 5.3.1.4 shows the SNR loss versus integration time at the far range.

From the above equations, it is evident that consideration must be given to the pulse length vs. the range swath width. In the cases where the swath time is small relative to the pulse length, the problems with deramp processing are minimized so that matched filtering and deramp processing are nearly equivalent. An effect similar to reducing the swath time can be obtained by using video filters and separate channels.

Another option in range processing is indicated in [17]. After deramping, the integration (Fourier transform) could be performed with different delays. In theory there are an infinite number of delays. However, this can be implemented practically using the "step transform" processing technique (see Chapter 10 in [21]).

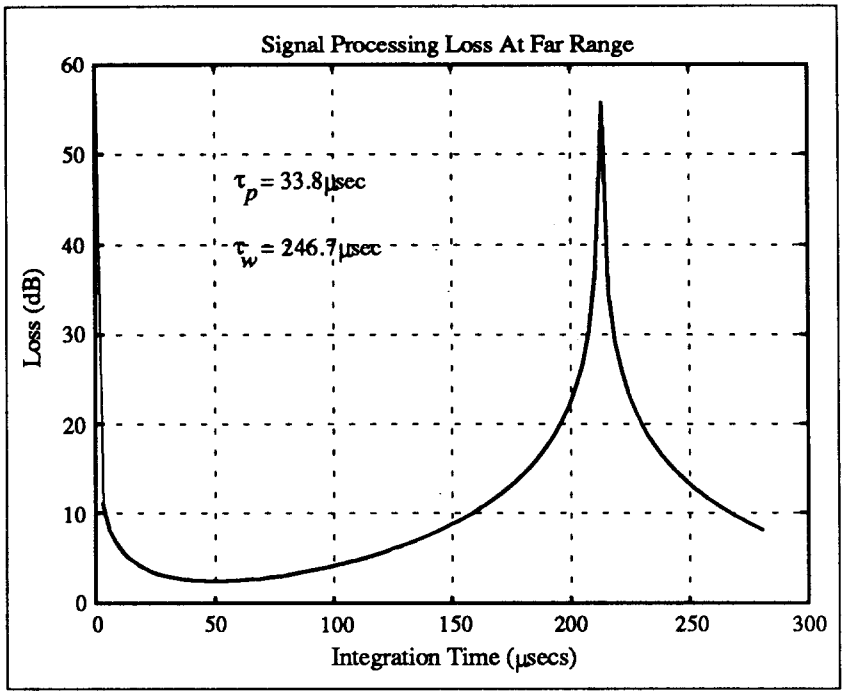

Figure 5.3.1.4: Potential Signal Processing Loss for Deramped Signal

Finally, other issues affect the range pulse length and range swath size. The most important are the PRF (see section 5.1), and power considerations (see section 5.4).

5.3.2 Doppler from Space

The Doppler frequency equation changes for spaceborne operation when compared with airborne SAR. This is due to the fact that the earth and the satellite orbit are rotating. The relative range velocity between targets on the surface of the earth and the satellite is a function of satellite velocity, earth rotation rate, and the orbit type and position. In this document, we will limit the discussion to the case of a circular orbit. However, the more general case of elliptical orbit is considered in [21]. An elliptical orbit adds another velocity term dependent upon where the satellite is in its orbit, similar to the motion of the earth, which is described below [26].

The Doppler frequency for a radar in circular orbit is given in [RANE86] as follows:

$$f_{Dop} = \left(\frac{2V_{st}}{\lambda}\right)\cdot\sin(\gamma)\cdot\cos(a)\cdot\left\{1-\left(\frac{\omega_e}{\omega}\right)\cdot\left[\varepsilon\cdot\cos(\beta)\cdot\sin(\psi)\cdot\tan(a)+\cos(\psi)\right]\right\} \tag{5.3.2.1}$$

where:

V_{st} - is the satellite velocity
λ - is the wavelength
γ - is the elevation angle (angle from nadir to target range vector)
a - is the squint (called "yaw") angle from spacecraft velocity vector to target on ground
ω_e - is the angular rotation rate of the earth
ω - is the angular rotation rate of the satellite
ε - is -1 if the radar is looking out the left side of the satellite (from velocity vector), otherwise 1
β - is the argument of the latitude (see section on orbit and coordinate systems)
ψ - is the orbit inclination angle (see section on orbit and coordinate systems)

There are many important things to note from this equation. If we ignore the rotation of the earth (i.e., ω_e is zero), we get the standard form of the Doppler equation:

$$f_{Dop} = \frac{2 \cdot \left(\vec{V}_{st} \cdot \vec{u}_r \right)}{\lambda} = \frac{2 V_{st} \cdot \sin(\gamma) \cdot \cos(a)}{\lambda} \tag{5.3.2.2}$$

So, the second term in the braces accounts for the rotation of the earth.

The differences between equation (5.3.2.1) and (5.3.2.2) are the changing velocity of the earth with latitude. Equation (5.3.2.2) can be used if we substitute an equivalent squint angle as follow:

$$a_{equiv} = \arccos\left\{ \cos(a) \cdot \left[1 - \left(\frac{\omega_e}{\omega} \right) \cdot \cos(\psi) \right] - \left(\frac{\omega_e}{\omega} \right) \cdot \cos(\beta) \cdot \sin(\psi) \cdot \sin(a) \right\} \tag{5.3.2.3}$$

Note that in equation (5.3.2.3) the squint is altered to all targets and not just the targets at the beam center.

This equivalent squint angle is a function of the actual squint angle and the orbit position in terms of altitude (indirectly through ω), inclination, and argument of the latitude. As an important example of equation (5.3.2.3), zero Doppler frequency does not necessarily occur at broadside. The antenna can be steered to point at zero Doppler according to the equation (6) in [54]:

$$\tan(a_0) = \varepsilon \cdot \left[\frac{\left(\frac{\omega_e}{\omega} \right) - \cos(\psi)}{\cos(\beta) \cdot \sin(\psi)} \right] \tag{5.3.2.3}$$

where:

a_0 - is the yaw (squint) angle for zero Doppler

Notice that the zero Doppler yaw angle changes as a function of orbit position only and that it is independent of the look angle...The orbit position is included in the altitude (indirectly through ω); inclination, argument of the latitude, β; and the inclination of the orbit, ψ. In general, only the argument of the latitude is changing significantly. Figure 5.3.2.1 illustrates the squint angle value that yields zero Doppler vs. the argument of the latitude. This has led to a technique of "yaw steering", where the satellite or the antenna beam pointing is varied with the orbit to maintain zero Doppler at the beam center. The European SAR satellite ERS-1 is using yaw steering for controlling the satellite pointing and the Germans are considering using electronic beam steering in a follow-on mission to X-SAR [57].

The benefits of yaw steering are the same as the benefits of imaging the target at broadside in the airborne SAR. These include simpler image formation and less distortion in the final image. In particular, yaw steering removes the problems associated with range-walk for line-by-line processing, as described in section 5.3.3.

To further illustrate equations (5.3.2.1) and (5.3.2.3), Figure 5.3.2.2 shows plots of the isorange and isoDoppler lines. Figures 5.3.2.2d-g illustrates how the the isoDoppler lines vary with the orbit position, i.e, the argument of the latitude. Notice from Figure 5.3.2.2f that when the argument of the latitude is either 90° or 180° we obtain the isoDoppler lines similar to what we would expect from an airborne SAR looking broadside. This is because at these points in the orbit, the orbit velocity and earth (target)

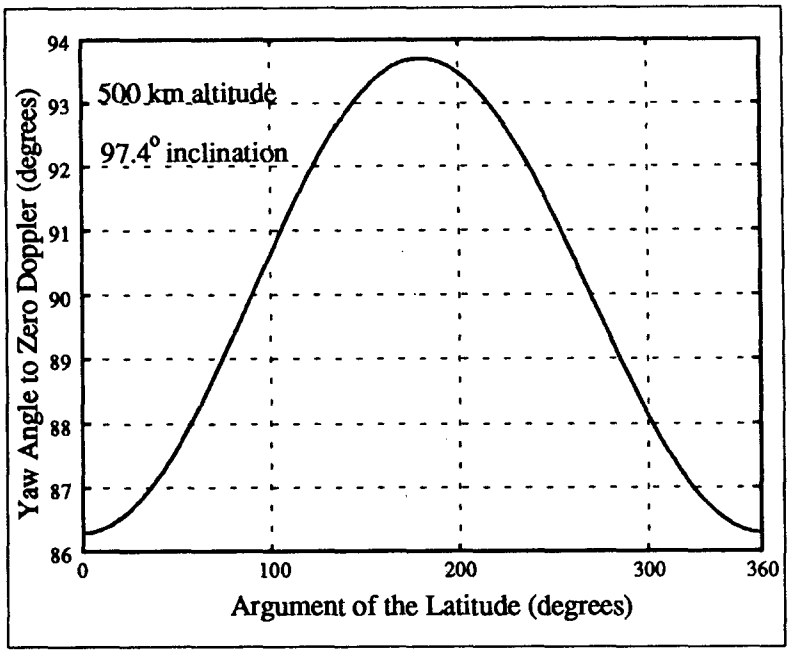

Figure 5.3.2.1: Yaw Angle to Zero Doppler vs. Orbit Position

velocity are parallel to each other, i.e., little to no Doppler caused by the earth's rotation. Also, notice from Figure 5.3.2.2e and Figure 5.3.2.2g that the apparent squint of the isoDops has the opposite sign when the argument of the latitude differs by 90°.

Figures 5.3.2.2h and 5.3.2.2i depicts the "yaw-steering" mentioned above. From Figure 5.3.2.1, above, we see that the yaw (squint) angle to zero Doppler is at 86.3° at an argument of the latitude of 0°. Figure 5.3.2.2h shows the isoDoppler lines centered at broadside. Figure 5.3.2.2i shows that we get the standard (i.e., similar to an airborne SAR flying a parallel line path) isoDoppler lines centered about zero Doppler when squinted to 86.3° just as predicted.

Figures 5.3.2.2a-c point out an interesting paradox. The only difference in these figures is the look angles. As stated previously, the yaw angle to zero Doppler is independent of the look angle. These figures appear to contradict this statement, however, these figures are deceptive. To avoid making the figures "busy", the values of the Doppler have been neglected. Although the isoDoppler lines for the 60° look angle case appear to be "less squinted" than the 20° look angle, the opposite is in fact true. The isoDoppler lines for the 60° case are actually at a much higher Doppler frequency than those in the 20° case. Figure 5.3.2.3 shows what is happening. The result of the motion of the earth relative to the satellite is to slightly rotate the typical hyperbolic lines of the isoDoppler contours as in Figure 5.3.2.3.

The degree of rotation varies with the argument of the latitude. Boxes are drawn around the regions in Figure 5.3.2.3 corresponding to Figures 5.3.2.2a-c. It is apparent that the lines appear less skewed in the upper box (nealy 60° look angle) than those in the lower box (nearly 20 look° angle).

A similar "skewing" of the isoDoppler lines occurs in an airborne SAR if the antenna phase center has a velocity component which deviates slightly from the path parallel to the target. We could mimic the spaceborne SAR with an airborne SAR by flying a slowly varying sinusoidal trajectory. The angle of the trajectory is given by the complement of the angle given in equation (5.3.2.3). It should be pointed out that we cannot exactly mimic the spaceborne SAR for range and azimuth locations.

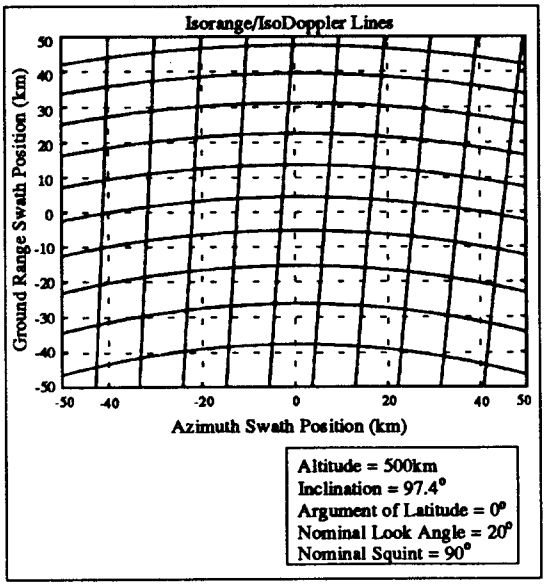

Figure 5.3.2.2a

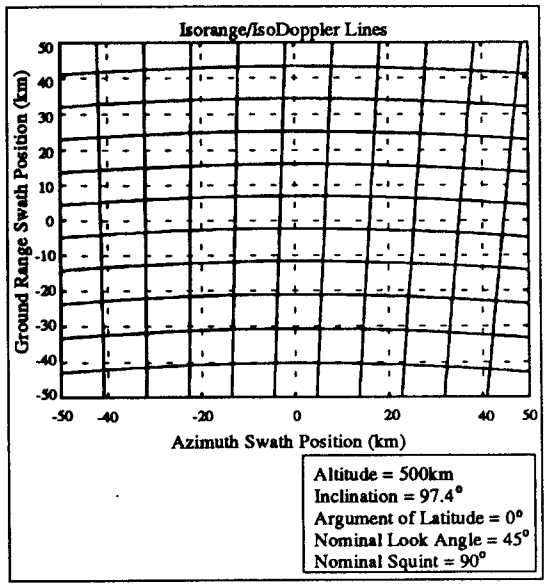

Figure 5.3.2.2b

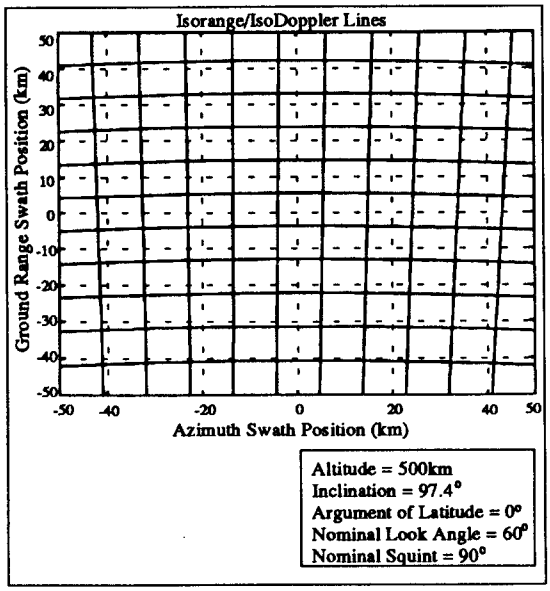

Figure 5.3.2.2c

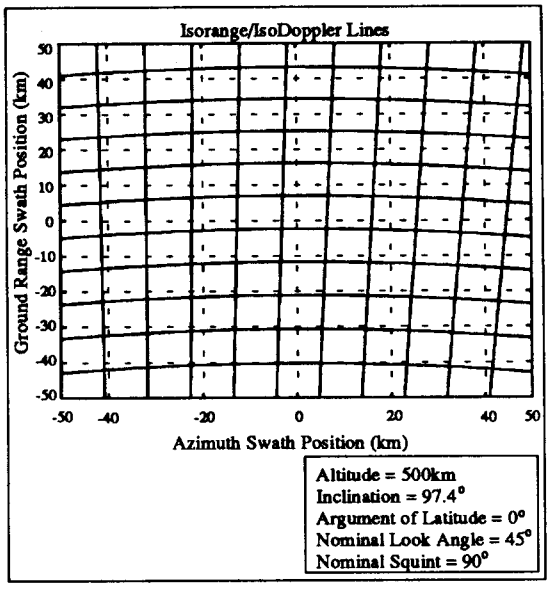

Figure 5.3.2.2d

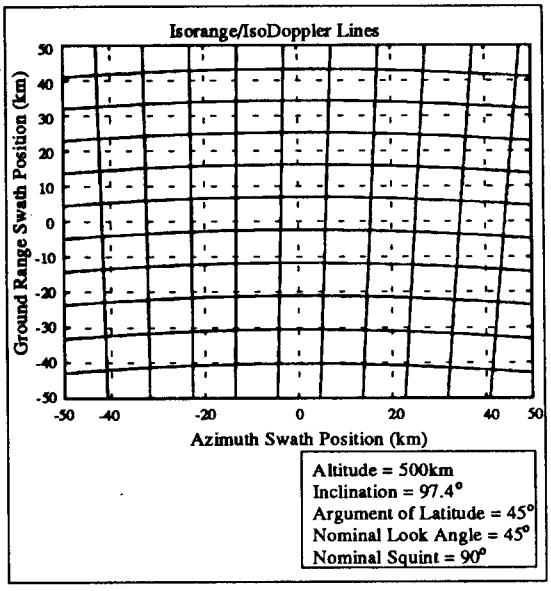

Figure 5.3.2.2e

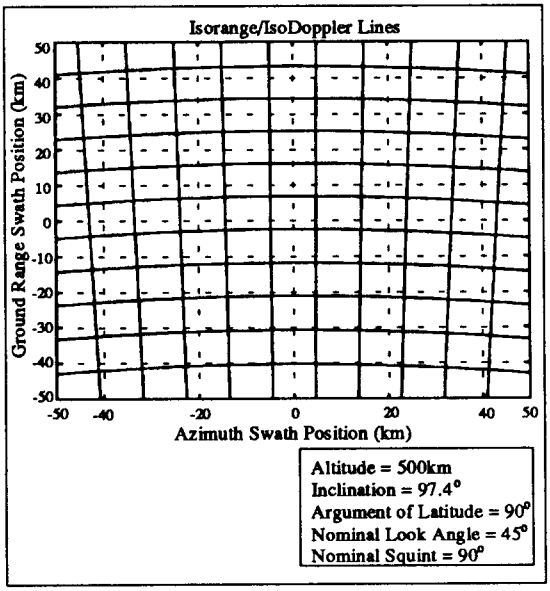

Figure 5.3.2.2f

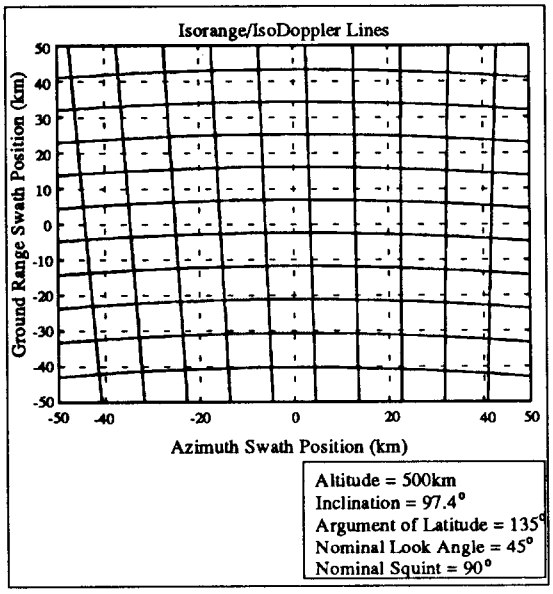

Figure 5.3.2.2g

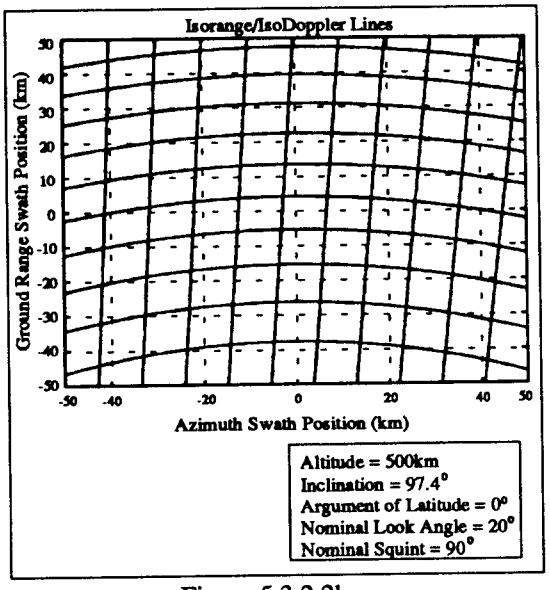

Figure 5.3.2.2h

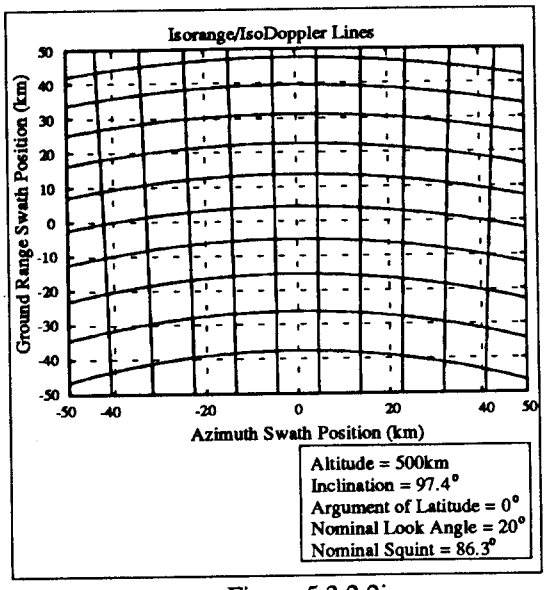

Figure 5.3.2.2i

Another interesting inference from equation (5.3.2.1) is that there is a range-walk component due to the earth's rotation. This component of range walk also changes with satellite location and oscillates in a sinusoidal manner as does the zero-Doppler yaw angle. It even changes directions as a satellite passes over the poles.

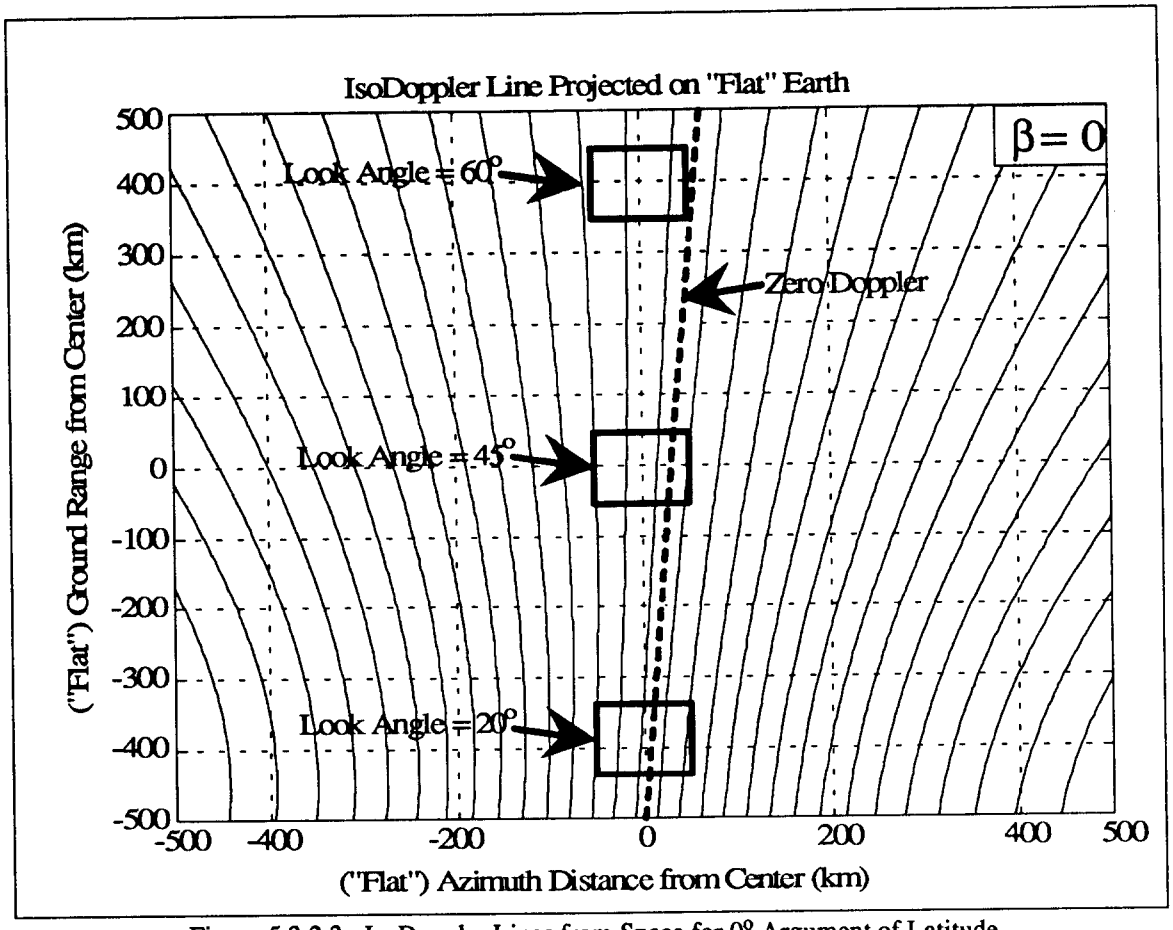

Figure 5.3.2.3: IsoDoppler Lines from Space for 0° Argument of Latitude

In this section, up until this point, we have shown that the velocity of the earth relative to the satellite is important and needs to be taken into account even though for an altitude of 500 km, the factor ω_e/ω is less than 7%. For purposes of simplicity in the rest of the report it will generally be omitted.

The Doppler rate (derivative of the Doppler frequency) is slightly different from the Doppler rate for an airborne system. For the airborne case:

$$\dot{f}_{Dop} \approx \frac{2V_x^2}{\lambda \cdot R} \tag{5.3.2.4}$$

whereas for the spaceborne case, ignoring earth rotation, it is:

$$\dot{f}_{Dop} \approx \frac{2V_{st}V_g}{\lambda \cdot R} \tag{5.3.2.5}$$

where:

V_g - is the velocity of the footprint of the satellite (ignoring the earth's velocity)

The footprint velocity, V_g,can be represented as:

$$V_g = \omega_s \cdot R_e \cdot \cos(\alpha) = V_{st} \cdot \left[\frac{R_e \cdot \cos(\alpha)}{R_s}\right] = V_{st} \cdot \left[1 - \frac{R \cdot \cos(\gamma)}{R_s}\right] \tag{5.3.2.6}$$

where:

α - is the earth interior angle

Equation (5.3.2.6), and hence (5.3.2.5), includes a term due to ratio of the earth radius to the satellite radius to the center of the earth and the radius of the beam path along the earth. This term accounts for the circular geometry of the earth and the satellite path [53]. Notice that it provides a slight, but perhaps significant, benefit in terms of integration time, and parameters as opposed to airborne SAR. In some respects it can be thought of as a "pseudo-spotlight" effect, since the aperture length flown by the satellite is longer than the patch of ground covered on the earth due to the circular geometry. From Figure 5.3.2.4, we see that the satellite travels a distance of $2 \cdot \pi \cdot R_s$ in the same time it takes the footprint line on the ground to travel a distance of $2 \cdot \pi \cdot R_e \cdot \cos(\alpha)$. So the footprint velocity on the earth travels much slower than the velocity of the satellite by the ratio:

$$\frac{V_g}{V_{st}} = \frac{R_e \cdot \cos(\alpha)}{R_s} \tag{5.3.2.7}$$

The important question is: which velocity, V_g or V_{st}, determines *PRF*, resolution, antenna dimensions, power requirements, etc.? We have already noted that the Doppler bandwidth, equation (5.3.2.2), is determined by the relative motion of the satellite to the earth. This says that Doppler bandwidth and hence *PRF* are determined by the satellite velocity, V_{st}. We also notice from equation (5.3.2.5) that the derivative of the Doppler, often referred to as the Doppler rate, is proportional to the product of the satellite and footprint velocities.

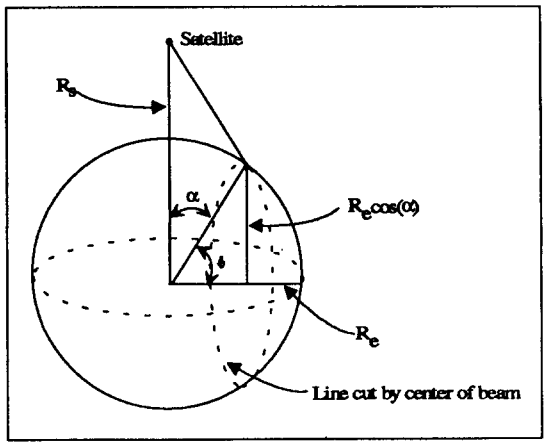

Figure 5.3.2.4: Geometry of Satellite Footprint Velocity

Section 5.3.6 will discuss velocity and resolution issues, and section 5.4.2 will discuss the power requirements issues and velocity.

5.3.3 Attitude Errors and Doppler

Attitude (pointing) errors are important for spaceborne SAR. The main effect of attitude errors is to decrease the SNR and increase the ambiguities in the image. There is a secondary effect which has to do with the azimuth PRF ambiguity, which will be discussed briefly, also.

To maximize the SNR and minimize the ambiguity ratio, it is desirable to center the antenna beam on the target area being imaged. If there is an error in the knowledge of the antenna beam pointing direction (resulting from satellite attitude errors or any other cause), the target area being imaged will be shifted with respect to the antenna beam. From figure 5.3.3.1, this means that the image being formed is not centered about the center of the antenna beam, i.e., the antenna beam is shifted with respect to the Doppler center frequency, f_C. The image formed will not be illuminated as well resulting in a loss in SNR.

In addition to decreased SNR there is a decrease in the signal to ambiguity ratio as well. The ambiguity referred to here results from aliased energy due to sampling. The reference [42] gives a good discussion of these ambiguity issues, so the discussion in this document is kept to a minimum. It should be pointed out that these ambiguities occur in both range and azimuth. Also, bright targets, such as nadir return, are particularly troublesome.

Currently, to solve these problems in azimuth, it is common to determine where the antenna was pointing after the fact using Doppler centroid techniques. The image is then formed at the position where the antenna was pointing. There is a fair amount of literature on Doppler centroid techniques as they pertain to spaceborne SAR, e.g. [43].

In some situations, the attitude error may cause the antenna beam to be shifted in azimuth by greater than or equal to half the PRF. This results in an ambuity which Doppler centroid techniques cannot resolve. Was the beam shifted forward or backward or greater than a PRF away? In other words, from figure 5.3.3.1, the Doppler centroid technique could select one of the aliased beams. Other processing techniques are required to resolve this problem ([3], [4] and [21]) otherwise, the range-walk will not be properly corrected for. It is desirable to limit pointing errors such that this ambiguity does not occur. These limits are approximately (ignoring the rotation of the earth) given by:

$$\varepsilon_y \leq \frac{PRF \cdot \lambda}{4 \cdot V_{st} \cdot \sin(\gamma) \cdot \sin(a)} \qquad (5.3.3.1)$$

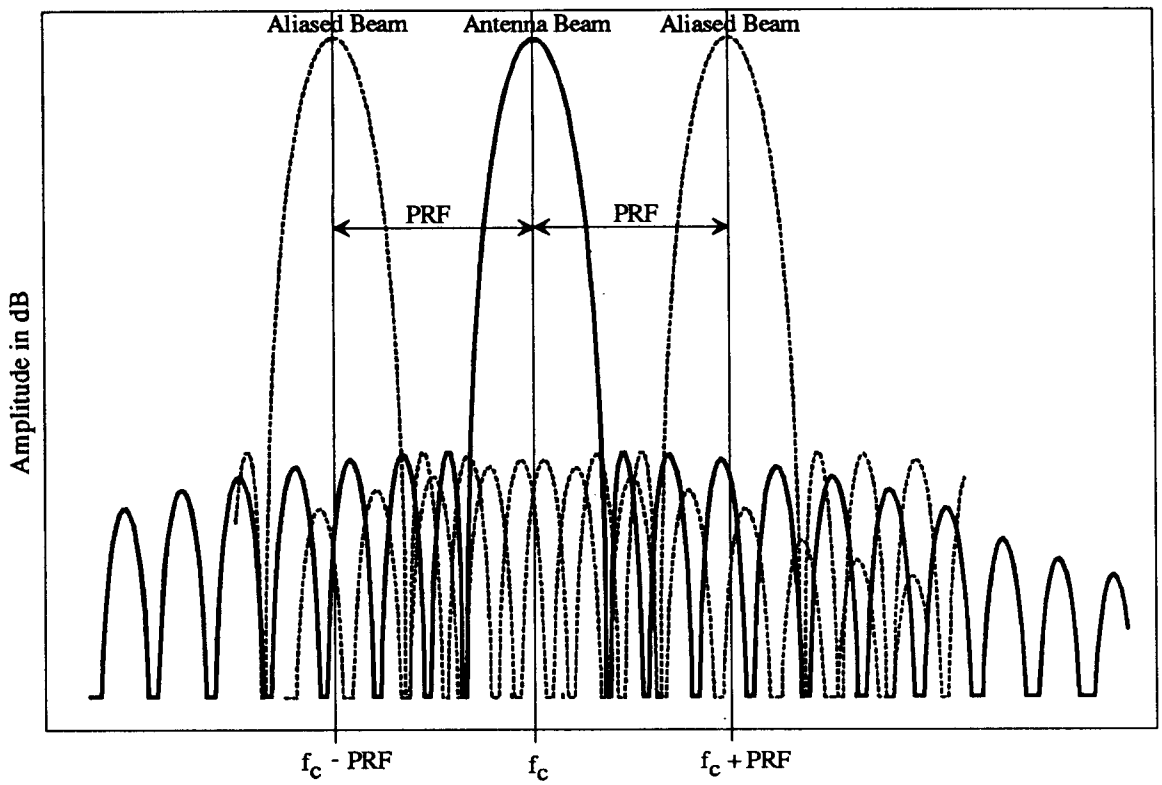

Figure 5.3.3.1: Illustration of Doppler Centroid and Ambiguity Problems

and

$$\varepsilon_p \leq \frac{PRF \cdot \lambda}{4 \cdot V_{st} \cdot \cos(\gamma)} \qquad (5.3.3.2)$$

where:

ε_y - is the satellite yaw angle error

ε_p - is the satellite pitch angle error

Figure 5.3.3.2 illustrates these limits for a satellite at 500 km altitude. Notice from the above equations and the figure that attitude errors are more important at higher frequencies. Also, it should be pointed out that the roll angle does not affect the Doppler significantly, so it is not part of this Doppler ambiguity limit.

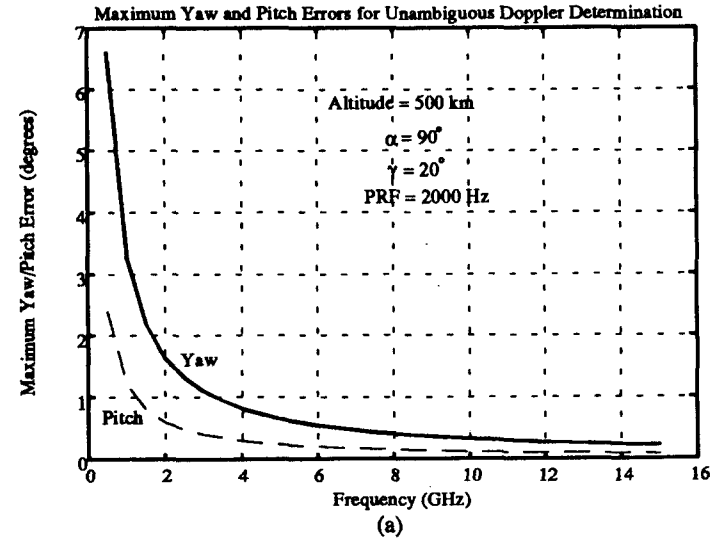

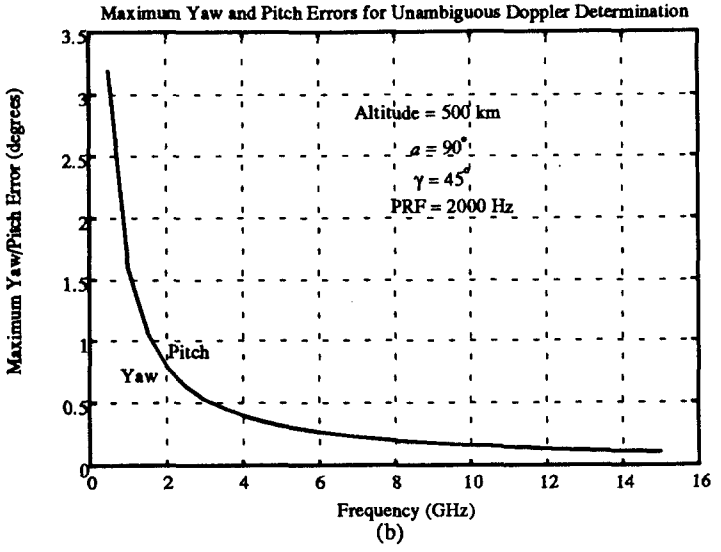

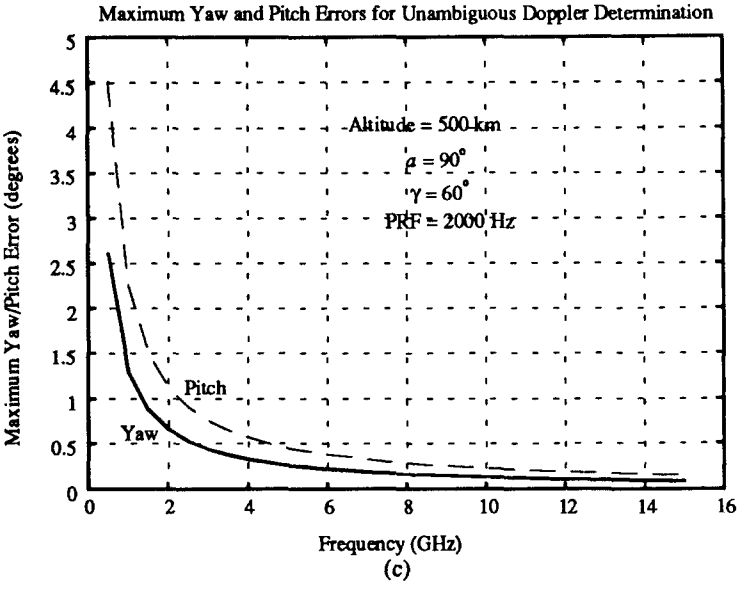

Figure 5.3.3.2: Maximum Yaw and Pitch Errors for Unambiguous Doppler Determination

5.3.4 Elevation/Earth Oblateness and Doppler

As mentioned in Appendix A, the earth is really an oblate sphere. It has a larger mean radius through the equator than it has through the poles by about 20 km. This combined with other topologic features, cause a change in the earth radius, R_e. This shows up in equation (5.3.2.1) in the look angle, γ. The look angle as a function of the earth radius is given in equation (A.4) in Appendix A. The consequence of the change in the look angle is to alter the shift in the Doppler spectrum. Since the sine of the look angle is a multiplier in the equation, the shift is worse the farther away from the zero Doppler the target gets. This is another reason for yaw steering or some similar counterpart.

Figure 5.3.4.1 shows the effects of elevation/earth radius changes. This figure illustrates that this Doppler shift due to elevation is influenced by the same things that influence Doppler in equation (5.3.2.1), namely, frequency, look angle, yaw (squint) angle, and satellite orbit position. Figures 5.3.4.1a and 5.3.4.1c shows that the shift is larger for angles farther away from the zero Doppler yaw steering angle. This shift is also larger for larger elevations, higher frequencies and smaller look angles.

This shift is similar to the shift mentioned above due to yaw and pitch angle uncertainties. It can be compensated for if the elevation of the target is known. If the elevation is unknown, Doppler centroid techniques can be used to compensate for this problem if all of the terrain is at the same elevation; however, Doppler centroid techniques cannot distinguish between yaw, pitch, and/or terrain elevation errors. Also, the same ambiguity issue potentially arises, although, typically Doppler shifts due to terrain elevation uncertainties are much smaller than those due to yaw and pitch errors. The exception to this is that the oblateness of the earth must be accounted for in some fashion.

A final note on elevation and Doppler is that if there are tall objects (such as mountains) in the image, this Doppler shift distorts the azimuth position of the object. This is the azimuth effect of layover [49].

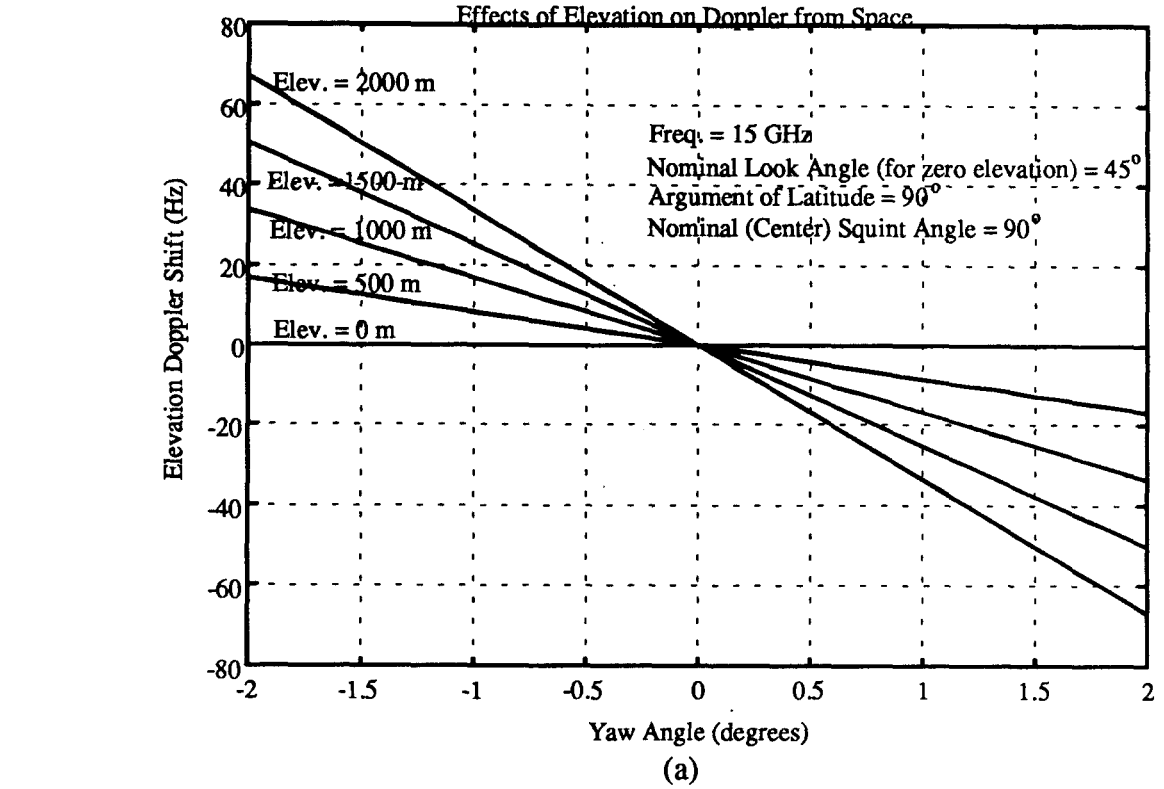

(a)

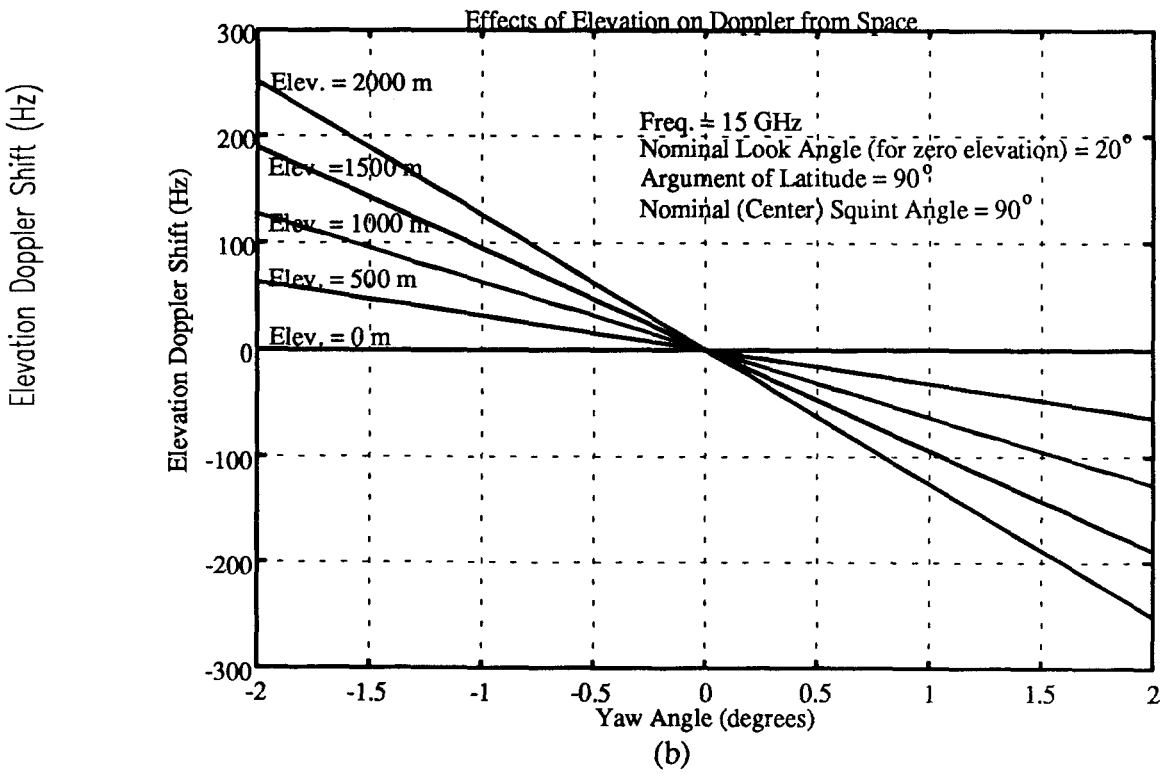

(b)

Elevation Doppler Shift (Hz)

Figure 5.3.4.1: Doppler Shift Due to Elevation

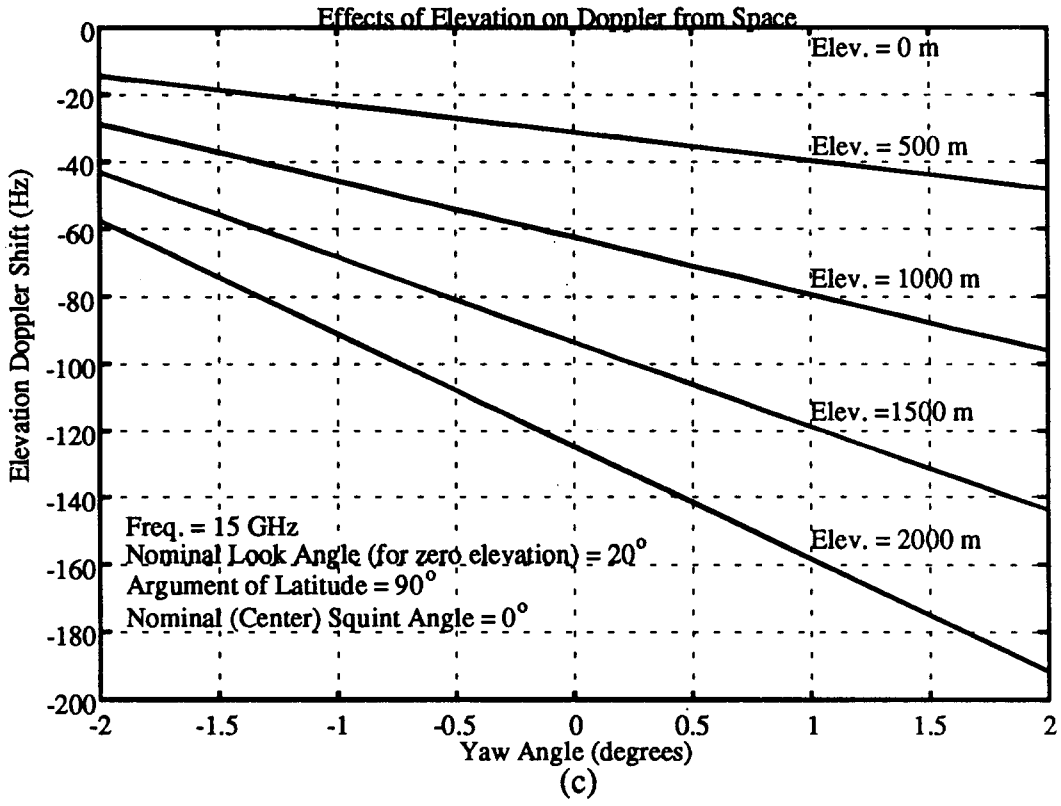

(c)

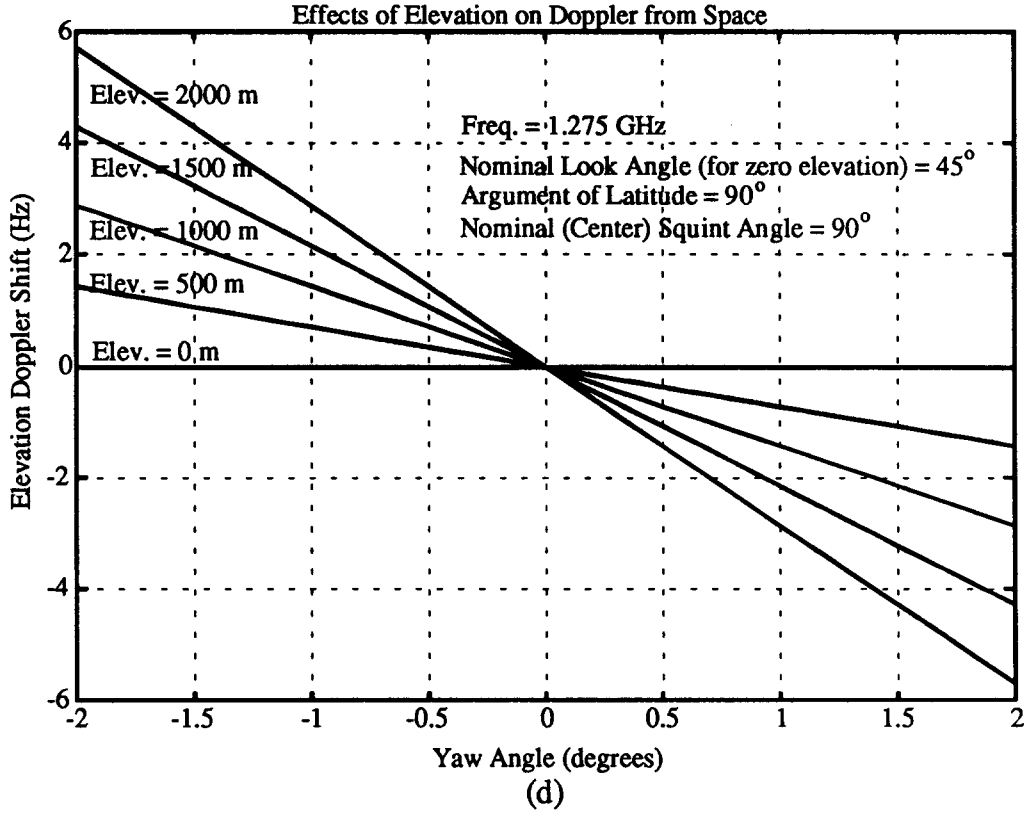

(d)

Figure 5.3.4.1: Doppler Shift Due to Elevation

5.3.5 Azimuth Processing

As with airborne SAR, spaceborne SAR data can be processed as patches or "line-by-line". In patch processing, images are formed by processing in "batch mode". In other words, the image resulting from a single aperture contains many azimuth pixels. In "line-by-line" processing, the aperture continuously slides by one azimuth sample, and only one azimuth pixel is generated per aperture. Patch processing is much more computationally efficient; however, there are some additional trade-offs which make "line-by-line" processing important for satellite SARs. The details for various patch processing can be found in other references (Chapter 10 of [21], [18], [19], [13]) so they will not be described here. "Line-by-line" processing will be discussed in a little more detail in this section.

There are several references describing "line-by-line" processing ([5], Chapter 4 of [21], perhaps the clearest [60]). "Line-by-line" processing can be thought of at one extreme as a single Doppler filter, and at the other extreme as a 2-D correlation. The simplest way (I believe) to think of "line-by-line" processing is as applying a phase correction vector such that a single pixel is produced by summing the resulting azimuth vector in phase. This is a similar process to phased-array antennas, except that "line-by-line"processing focuses at a specific range and the aperture is a synthetic aperture.

The reason for using "line-by-line" processing is that it can achieve the full theoretical resolution of $D_a/2$, where D_a is the azimuth dimension of the antenna (subject to the implementation which will be described later). What this says is that for a given desired azimuth resolution, D_a is the largest the azimuth antenna dimension can be. The larger the azimuth antenna dimension is, the narrower is the beamwidth, which in turn reduces power and the maximum Doppler frequency. The latter determines the minimum *PRF* possible. One way to think of this is that the full Doppler bandwidth is used to form an image. Another way is that the full beamwidth of the antenna is used in the processing. This constraint is illustrated in Figure 5.3.5.2. Note from the figure that the aperture length is equal to the beamwidth on the ground. Both are ($\lambda R/D_a$).

It should be pointed out that the azimuth beamwidth (β_{az}) of λ/D_a is only approximate, and typically a taper is applied to the antenna beam causing the beamwidth to be larger than λ/D_a. This should be included in an actual design. For the rest of this section the approximation of λ/D_a is used.

The implementation of "line-by-line" processing can be either as a correlation or as a matched filter. In [21] these are referred to as "time-domain" and "frequency-domain" algorithms, respectively.

The implementation requires some consideration. First of all, the azimuth resolution is really a function of the range according to the equation (ignoring the spreading of the impulse response caused by the processing window):

$$\rho_a = \left(\frac{\lambda \cdot R}{2 \cdot L_a} \right) \qquad (5.3.5.1)$$

where:

L_a - is the synthetic aperture length

This equation implies that the aperture length must change linearly with the slant range. We can see this from the figure as well when we use the full aperture length as follows:

$$L_a = \left(\frac{\lambda \cdot R}{D_a} \right) \qquad (5.3.5.2)$$

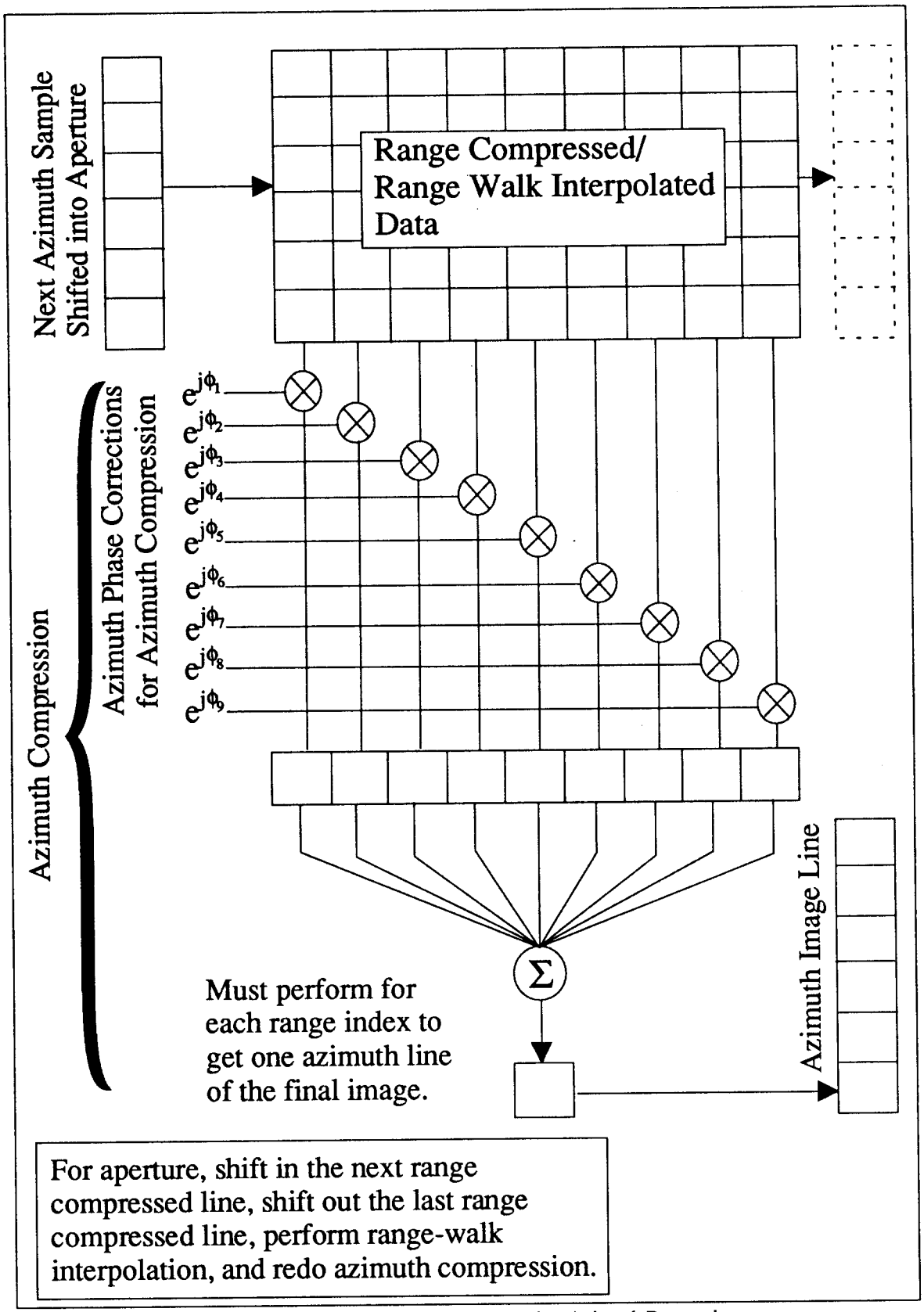

Figure 5.3.5.1: Overview of Line-by-Line Azimuth Processing

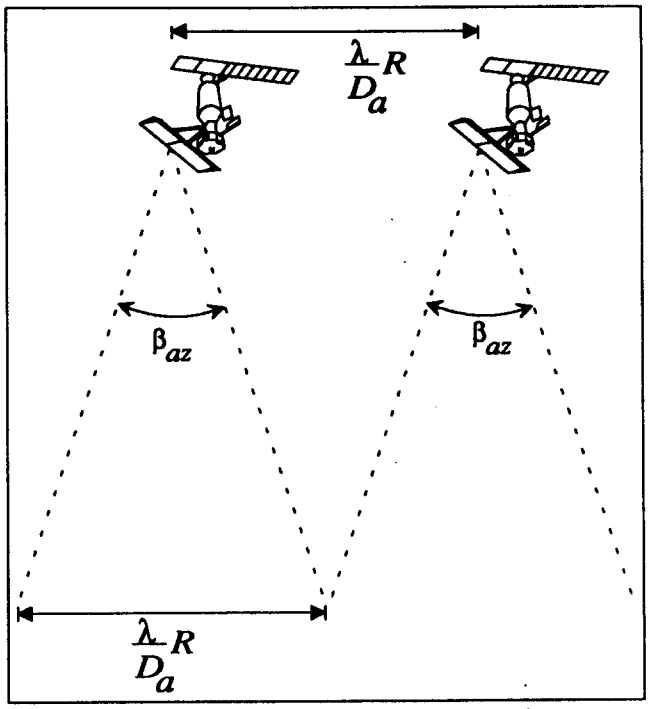

Figure 5.3.5.2: Full Theoretical Resolution

This is achievable but may not be practical since it requires processing a different number of azimuth points for each range.

Notice that in order to obtain the full $D_a/2$ resolution, the output azimuth line is delayed by half the aperture length for a broadside pointing antenna. Also, as with all processing algorithms, range migration must be accounted for. Typically this is performed by an interpolation step after range processing.

The disadvantage of patch processing is that the Doppler bandwidth must be larger than that of "line-by-line" processing. The two-sided Doppler bandwidth for an image at broadside using "line-by-line" processing is approximately:

$$BW_{Dop} \geq \left(\frac{V_x}{\rho_a}\right) \tag{5.3.5.3}$$

For patch processing this becomes:

$$BW_{Dop} \geq \left(\frac{V_x}{\rho_a}\right) + \left(\frac{2 \cdot V_x \cdot P_a}{\lambda \cdot R}\right) \tag{5.3.5.4}$$

where;

P_a - is the azimuth patch width in meters

The main problem with this is that the lower limit on the *PRF*, as well as power, must be increased according to this equation. This can be avoided somewhat by using spotlight mode processing or a scanning mode at the possible expense of continuous coverage and/or more sophisticated antenna design.

Another note is on the complexity of the "line-by-line" processing. It requires processing an entire aperture's worth of data for a single azimuth line. This is as opposed to generating hundreds to thousands of azimuth lines with patch processing from a similar amount of data. "Line-by-line" processing has a 100% duty cycle, as opposed to 10 to 30% for patch processing. In other words, for "line-by-line" processing, every azimuth sample is used. For patch processing, the processor can "rest" for a while.

An interesting example of the "duty cycle" trade-off mentioned in the previous paragraph is that the Magellen SAR processor uses patch processing (referred to as "burst mode") to reduce the data transmission rate [34]. In other words, data is not collected continuously but only over each aperture. This technique means that patch processing must be used and "line-by-line" processing cannot be used.

There are some techniques for speeding up the the "line-by-line" processing, by recognizing the fact that it is just a correlation. If it is assumed that the same correlation filter can be used for processing several consecutive azimuth lines, then "batch" processing can be performed. Batch processing implements the azimuth compression using the fast correlation technique, i.e., the FFT. The assumption for batch processing is that Doppler parameters, namely the first, second, etc., derivatives of range for the azimuth line being processed change slowly with time. As an example, in the ideal case, the azimuth line being processed is broadside with the Doppler being zero. As the radar passes by, it is assumed that antenna phase center stays pointed at the zero Doppler line for several azimuth lines.

It is important to notice that patch processing and batch processing are not the same. Patch processing uses the the same aperture to generate several azimuth lines. Batch processing is a "sliding" correlation, so it uses different apertures for each of the several azimuth lines that it generates.

The problems that must be overcome for batch processing include depth-of-focus issues, changing Doppler parameters, and range migration. Of these, the most severe problem for spaceborne systems is range-walk.

5.3.6 Resolution and Orbital Geometry

As mentioned in section 5.3.2, the circular geometry gives rise to a satellite velocity, V_{st}, and a footprint velocity, V_g. The question was posed as to which velocity affects the resolution. The answer is that the azimuth resolution is provided by the time the beam dwells upon a target, i.e., the integration time. Using the maximum aperture size, this aperture time is given by:

$$T_{ap} = \frac{R \cdot \beta_{az}}{V_g} \tag{5.3.6.1}$$

where:

T_{ap} - is the aperture time using the full beamwidth
β_{az} - is the beamwidth of the antenna

The maximum aperture length is given as:

$$L = V_{st} \cdot T_{ap} = \frac{V_{st}}{V_g} \cdot R \cdot \beta_{az} \tag{5.3.6.2}$$

This means that the azimuth integration time is longer than for airborne SAR by the ratio given in equation (5.3.2.7). Notice that we are ignoring the affect of the earth's rotation.

Again assuming no taper on the antenna pattern we get the relationship between the azimuth resolution and the azimuth dimension of the antenna to be:

$$\rho_a = \left(\frac{D_a}{2}\right)\cdot\left(\frac{V_g}{V_{st}}\right) \qquad (5.3.6.3)$$

The implication of equation (5.3.6.3) is that we can make the antenna slightly longer which gives us a little relief on the lower limit of the *PRF* and on power considerations.

Note that this section does not address actual spotlight processing for which the integration time could be longer than equation (5.3.6.1).

5.3.7 General Processing Issues

It is interesting to compare some typical processing parameters for spaceborne SAR versus an airborne SAR. The first parameter to consider is azimuth integration time. The ratio of the spaceborne to airborne integration time is given by the ratio of the respective ranges divided by the respective velocities. For a satellite at 500 km altitude, the velocity is approximately 7.6 km/second and range to the target for a 45° look angle is approximately 740 km. This yields the same azimuth integration time for a given resolution and frequency as an airborne SAR flying 55 meters/second at a range of 5350 meters.

Even though the azimuth integration times might be comparable, the azimuth sample rates are significantly higher for a spaceborne SAR with the same resolution. This is because the velocities are much higher in equation (5.3.5.3). If we use the same example as above, the spaceborne SAR will require roughly 138 times as many samples as the airborne SAR.

Similarly, because swath sizes are typically larger for the spaceborne SAR than the airborne SAR, the processing load in range will increase by a factor of the ratio of the swath sizes. This might add another factor of ten to the processing bandwidth. The conclusion is that the spaceborne SAR is a more challenging system in terms of image processing.

5.3.8 Summary Comments

In summary we have found the following main points:

1) The larger swaths and limits on pulse width due to PRF constraints mean that the range processing is more constrained than for typical airborne SAR.

2) The motion of the earth must be accounted for in spaceborne SAR. Its affect on the Doppler frequency changes with the satellite's position in orbit. It also adds to geometric distortion in the resulting image.

3) It is important to remove the satellite attitude errors and large altitude variations due to the oblateness of the earth. This can add to processing complexity.

4) Line-by-line azimuth processing permits a larger azimuth antenna dimension than does patch processing. This is important for PRF and power considerations. However, line-by-line azimuth processing is computationally expensive.

5) In design, care must be taken when considering whether to use the satellite velocity or the footprint velocity. For azimuth integration time the circular orbit acts as "pseudo-spotlight".

5.4 Transmitter Power Requirements

This section derives the basic radar equation for SAR and discusses the transmitter power issues for spaceborne SAR.

5.4.1 SAR Radar Equation

The derivation for the radar equation for SAR is presented in this section so that all of the assumptions are apparent. This derivation can be found in many references (e.g., [21]). The standard radar equation can be written as:

$$P_R = \frac{P_t \cdot G_T \cdot \sigma \cdot A_e}{\left(4 \cdot \pi \cdot R^2\right)^2} \qquad (5.4.1.1)$$

where:

P_R - is the power at the receiver
P_t - is the power transmitted
G_T - is the transmitter gain
σ - is the radar cross-section (RCS) of the target
$A_e = e_a \cdot A$, is the effective area of the antenna
A - is the actual area of the antenna
e_a - is the efficiency of the antenna, the ratio of incident power on antenna to power transferred to the receiver (usually 0.5-0.7, due to reflections, etc.)
R - is the range to the target

By using reciprocity and the following equation for the effective area of the antenna:

$$A_e = \frac{\lambda^2 \cdot G_R}{4 \cdot \pi} \qquad (5.4.1.2)$$

we get another form of the radar equation:

$$P_R = \frac{P_t \cdot \lambda^2 \cdot G^2 \cdot \sigma}{(4 \cdot \pi)^3 \cdot R^4} \qquad (5.4.1.3)$$

Equation (5.4.1.3) is the basic form of the radar equation.

Noise power is given by:

$$N = k \cdot F \cdot T_s \cdot B_n \qquad (5.4.1.4)$$

where:

N - is the noise power
k - is Boltzman's constant
F - is the noise figure to account for receiver noise
T_S - is the source equivalent noise temperature, typically 290° K (noise equivalent temperature of the earth)
B_n - is the noise bandwidth

Including the gains from coherent processing and expressing (5.4.1.3) in terms of signal-to-noise ratio, we obtain:

$$SNR_I = \frac{N_p \cdot N_R \cdot N_a \cdot P_t \cdot \lambda^2 \cdot G^2 \cdot \sigma}{(4 \cdot \pi)^3 \cdot R^4 \cdot k \cdot F \cdot T_s \cdot B_n} \qquad (5.4.1.5)$$

where:

SNR_I - is the SNR including the coherent gain
N_p - is the presum integer
N_R - is the number of range samples processed
N_a - is the number of azimuth samples processed

The following equations can be substituted into equation (5.4.1.5):

$$N_a = \frac{\lambda \cdot R \cdot PRF}{2 \cdot \rho_a \cdot V_{st} \cdot N_p} \qquad (5.4.1.6)$$

where:

PRF - is the pulse repetition frequency
V_{st} - is the velocity of the satellite
ρ_a - is the azimuth resolution

and:

$$N_R \approx B_n \cdot \tau_p \qquad (5.4.1.7)$$

where:

τ_p - is the pulse length

Note in this last equation that we have assumed that the receiver bandwidth is the same as the noise bandwidth.

The SAR radar equation for a point target becomes:

$$SNR_I = \frac{P_t \cdot \lambda^3 \cdot G^2 \cdot \sigma \cdot PRF \cdot \tau_p}{2 \cdot (4 \cdot \pi)^3 \cdot R^3 \cdot k \cdot F \cdot T_s \cdot V_{st} \cdot \rho_a} \qquad (5.4.1.8)$$

Another form of equation (5.4.1.8) is found by using the equation for the average power:

$$P_{avg} = P_t \cdot \tau_p \cdot PRF \qquad (5.4.1.9)$$

Then (5.4.1.8) becomes:

$$SNR_I = \frac{P_{avg} \cdot \lambda^3 \cdot G^2 \cdot \sigma}{(4 \cdot \pi)^3 \cdot R^3 \cdot k \cdot F \cdot T_s \cdot 2 \cdot V_{st} \cdot \rho_a} \qquad (5.4.1.10)$$

In addition, other losses need to be considered:

$$SNR_1 = \frac{P_t \cdot \lambda^3 \cdot G^2 \cdot \sigma \cdot PRF \cdot \tau_p \cdot L_{tot}}{2 \cdot (4 \cdot \pi)^3 \cdot R^3 \cdot k \cdot F \cdot T_s \cdot V_{st} \cdot \rho_a} \qquad (5.4.1.11)$$

where:

$L_{tot} = L_{sp} + L_{atmos} + L_{tx} + L_{rx} + L_{Beam}$
L_{sp} - signal processor loss
L_{atmos} - two-way atmospheric and ionospheric loss
L_{tx} - transmitter line losses
L_{rx} - receiver line losses
L_{Beam} - loss due to the fact that the antenna gain is not constant over the beamwidth

A little more detail on the beam loss. The gain is actually a function of azimuth and elevation pointing angles of the antenna. If we choose to use the maximum gain of the antenna, then we need to account for the difference (beam "loss") at the edges of the scene. This beam loss occurs in both azimuth and range (elevation) and these two components multiply together (add in dB). The worst case occurs at the outer edges of the patch, so the larger the patch size relative to the beamwidth, the worse this loss term will be. As pointed out in section 5.3.3, if we attempt to achieve $\rho_a = D_a/2$ resolution, we are using the entire beamwidth. In patch processing, we cannot use the entire beamwidth. Also, the mode of operation is important. If strip-map mode processing is used, a convolution with the beamwidth occurs. In other words, the portion of the beam illuminating the target varies during the aperture (i.e., the azimuth angle to the target changes during an aperture). If spotlight mode processing is used, we do not gain this advantage, since essentially the same portion of the beam illuminates the target throughout the entire aperture.

Now we make the following simplified argument for a distributed target. A more complete discussion is given in [21]. The RCS is approximated as follows:

$$\sigma \approx \int \sigma^o \cdot dA \approx \langle \sigma^o \rangle \cdot A \qquad (5.4.1.12)$$

where:

σ^0 - is the normalized RCS as a function of target location
$\langle \sigma^0 \rangle$ - is the mean normalized RCS
$dA = \rho_{rg} \cdot \rho_a$, is a differential element of area of the target on the ground,
A - is the area of the radar return
ρ_{rg} - ground range resolution
ρ_a - azimuth resolution

From now on, the mean normalized RCS will be referred to as just the normalized RCS and the symbol, σ^0, will be used. Then the SAR radar equation for SNR including coherent processing gains for a distributed target is:

$$SNR_1 = \frac{P_t \cdot \lambda^3 \cdot G^2 \cdot \sigma^0 \cdot PRF \cdot \tau_p \cdot \rho_{rg} \cdot L_{tot}}{2 \cdot (4 \cdot \pi)^3 \cdot R^3 \cdot k \cdot F \cdot T_s \cdot V_{st}} \qquad (5.4.1.13)$$

Or written in terms of average transmitter power, it becomes:

$$SNR_1 = \frac{P_{avg} \cdot \lambda^3 \cdot G^2 \cdot \sigma^0 \cdot \rho_{rg} \cdot L_{tot}}{2 \cdot (4 \cdot \pi)^3 \cdot R^3 \cdot k \cdot F \cdot T_s \cdot V_{st}} \qquad (5.4.1.14)$$

Often, it is desirable to calculate the transmitter power required for a target detection. In these cases the noise equivalent σ^0 ($\sigma_n{}^0$) is specified, which is the σ^0 which makes the $SNR_1 = 1$ (i.e., 0dB).

5.4.2 SAR Radar Equation in a Circular Orbit

As revealed in section 5.3.2, there are issues to consider in satellites about which velocity to use ([54]). In reference [55], it is pointed out that the choice between satellite velocity (V_{st}) and beam footprint velocity (V_g) is important. Although the signal duration (see equation 5.3.4.1) is a function of the footprint velocity, the azimuth resolution is a function of the ratio of the footprint velocity to the satellite velocity. The net affect is that equation (5.4.1.6) still holds and the above equations are still valid. Care must be taken if the equation for azimuth resolution is used (e.g., equation 5.3.4.2). In this case, the footprint velocity may be necessary for equation (5.4.1.11).

5.4.3 Power Requirements for Multibeam/Multiphase Center Antennas

Section 5.2 discusses a novel technique for handling the PRF problem by using multi-beam or multi-phase-center phased-array antennas. The purpose of these techniques is to permit larger swath sizes for a given resolution than for traditional methods of using the antenna beam. This section of the report discusses how the SAR radar equation is affected by these techniques.

The basis of these techniques is to use a longer antenna in creative ways to maintain a low PRF and still achieve large Doppler bandwidth for fine azimuth resolution. The following discussion will compare the SNR performance of these methods with the traditional SAR with the same length antenna. This discussion is based upon the reference [24].

There are four different cases to consider. They are:

1) Multi-phase-center technique for a distributed target

2) Multi-phase-center technique for a point target

3) Multi-beam technique for a distributed target

4) Multi-beam technique for a point target

For the multi-phase-center technique, only $1/N_B$ of the antenna in azimuth is used for both transmit and receive, where N_B is the number of beam phase centers in this case. However, the effective number of azimuth samples in equation (5.4.1.6) is increased by N_B due to the sampling at each beam center. The net result is that the SNR in equations (5.4.1.11) and (5.4.1.13) are reduced by $1/N_B$ for the multi-phase center technique. This result is a little misleading, since the equation for the point target, (5.4.1.11), includes the azimuth resolution. One of the purposes of these techniques is to permit the azimuth integration time to be increased by a factor of N_B. Hence, for the point target case the loss can be recuperated if the full azimuth integration time is utilized. Even though equation (5.4.1.11) contains all of this information, it is subtle.

To reiterate, for a multi-phase center distributed target, equation (5.4.1.13) becomes:

$$SNR_1 = \frac{P_t \cdot \lambda^3 \cdot G^2 \cdot \sigma^0 \cdot PRF \cdot \tau_p \cdot \rho_{rg} \cdot L_{tot}}{2 \cdot (4 \cdot \pi)^3 \cdot N_B \cdot R^3 \cdot k \cdot F \cdot T_s \cdot V_{st}} \qquad (5.4.3.1)$$

Note that the PRF used in this equation and in the previous paragraph is the actual transmitter PRF and not the azimuth sampling rate created by the multiple phase centers.

Similarly, equation (5.4.1.14) becomes:

$$SNR_I = \frac{P_{avg} \cdot \lambda^3 \cdot G^2 \cdot \sigma^0 \cdot \rho_{rg} \cdot L_{tot}}{2 \cdot (4 \cdot \pi)^3 \cdot N_B \cdot R^3 \cdot k \cdot F \cdot T_s \cdot V_{st}} \qquad (5.4.3.2)$$

For a multi-phase-center point target, equation (5.4.1.11) becomes:

$$SNR_I = \frac{P_t \cdot \lambda^3 \cdot G^2 \cdot \sigma \cdot PRF \cdot \tau_p \cdot L_{tot}}{2 \cdot (4 \cdot \pi)^3 \cdot N_b \cdot R^3 \cdot k \cdot F \cdot T_s \cdot V_{st} \cdot \rho_a} \qquad (5.4.3.3)$$

Equation (5.4.1.10) is:

$$SNR_I = \frac{P_{avg} \cdot \lambda^3 \cdot G^2 \cdot \sigma \cdot L_{tot}}{2 \cdot (4 \cdot \pi)^3 \cdot N_B \cdot R^3 \cdot k \cdot F \cdot T_s \cdot V_{st} \cdot \rho_a} \qquad (5.4.3.4)$$

For the multi-beam case, only $1/N_B$ of the azimuth antenna is used on transmission; however, the full azimuth antenna is used for reception of all N_B beams. Also, equation (5.4.1.6) is increased by the number of beams, N_B, similar to the multi-phase center above, but for different reasons. The net result in this case is that the equations given in section 5.4.1 are unchanged.

A final word on these equations is that for all of these techniques described in this section there will be additional losses due to design trade-offs. For example, in the multi-beam case, isolation between azimuth beams are important. Receiver beamwidths will have to be broadened to enable the sidelobes to be reduced, and the PRF will increase. This will result in more loss. In an actual design, these considerations will have to be taken into account.

5.4.4 Implications and Examples of SAR Radar Equation

This section will provide plots and examples of the implications of the SAR radar equation to transmitter peak and average power requirements. To do this, the equations in section 5.4.1 will be used and other forms of these equations will be derived. The results presented in section 5.4.3 will not be covered in this section, since the result is that the transmitter power must be multiplied by the factor N_B.

The analysis of the SAR radar equation is complicated by the subtle interdependency of the various parameters. As an example, equation (5.4.1.13) apparently does not depend upon the azimuth resolution. However, the gain, G, (for non-spotlight mode) and the PRF are bounded by azimuth resolution considerations. The gain is related to antenna area of which the azimuth dimension is bounded by (see section 5.3):

$$D_a \leq 2 \cdot \rho_a \qquad (5.4.4.1)$$

where:
D_a - is the azimuth antenna dimension
ρ_a - is the azimuth resolution

The PRF is bounded by (see equation 5.3.3.3):

$$PRF \geq \left(\frac{V_{st}}{\rho_a}\right) \tag{5.4.4.2}$$

In order to fully understand the basic implications of the SAR radar equation, assumptions are made, certain variables are fixed, and bounds are evaluated in an iterative manner. Section 6.0, pertaining to the case study, evaluates the radar equation and some trade-offs for a few specific point designs. This section is meant only to illustrate trends.

Another useful form of equation (5.4.1.11) for understanding the implications of the radar equation for a point target is obtained by using equation (5.4.1.2) and reciprocity to get the SAR radar equation in terms of the effective area of the antenna:

$$SNR_I = \frac{P_t \cdot A_e^{\,2} \cdot \sigma \cdot PRF \cdot \tau_p \cdot L_{tot}}{2 \cdot (4 \cdot \pi) \cdot \lambda \cdot R^3 \cdot k \cdot F \cdot T_s \cdot V_{st} \cdot \rho_a} \tag{5.4.4.3}$$

and similarly for a distributed target from equation (5.4.1.13):

$$SNR_I = \frac{P_t \cdot A_e^{\,2} \cdot \sigma^o \cdot PRF \cdot \tau_p \cdot \rho_{rg} \cdot L_{tot}}{2 \cdot (4 \cdot \pi) \cdot \lambda \cdot R^3 \cdot k \cdot F \cdot T_s \cdot V_{st}} \tag{5.4.4.4}$$

We can make some rough generalizations (ignoring the subtleties) based on the above equations for a fixed SNR_I value. From equations (5.4.1.10) and (5.4.1.14) we notice that the average power required is independent of the pulse duration, τ_p, or *PRF* for either the point target or distributed target case. To a first order, the average power required for a point target is proportional to the azimuth resolution but independent of the range resolution. On the other hand, for a distributed target, the average power required is inversely proportional to the range resolution on the ground and independent of azimuth resolution. Average power is proportional to the satellite velocity and the cube of the range to the target for both kinds of targets. (Actually, the azimuth resolution varies with range so that for the point target case it is really a R^4 variation.) If the antenna area is assumed to be a constant then average power required is inversely proportional to the operating frequency for both kinds of targets. This is reasonable for the azimuth dimension since it is tied to a resolution; however, it is not reasonable for the range dimension, since it is tied to a swath width, which also varies with frequency.

Peak power variation is similar to that of average power, except that peak power is inversely proportional to the product of the *PRF* and the pulse duration. Because of this, only average powers are plotted in this section.

An example case is presented to illustrate the power trends. Assume a distributed target. Assume nominal values as follows:

1) satellite altitude of 500 km
2) broadside pointing antenna
3) range swath width of 10 km on the ground
4) ground range resolution of 3 m
5) azimuth resolution of 3 m
6) noise equivalent σ^o (σ_n^o) of -25 dB
7) center frequency of 15 GHz (Ku band)
8) look angle to the center of the beam of 45°

In this example, one of the above variables will be varied and the others will remain fixed. In general, the antenna area will be fixed to 2 m by 1 m. The antenna area may be varied in elevation to maintain the necessary field-of-view and in azimuth to control azimuth resolution. The worst case, i.e. far-range, values will be calculated.

Figure 5.4.4.1 shows the case where the center frequency is varied. As indicated in equation (5.4.4.4), for everything else held constant, the power varies as the reciprocal of the frequency. In practice, everything else cannot be held constant over a wide frequency range. As indicated in the figure, there are PRF problems at frequencies lower than approximately 2 GHz. These are due to the fact that the antenna width was not allowed to grow beyond 3 meters. Also, the slight curve upwards beyond 10GHz is due to the fact that the antenna was made smaller to maintain the beamwidth for the 10km swath.

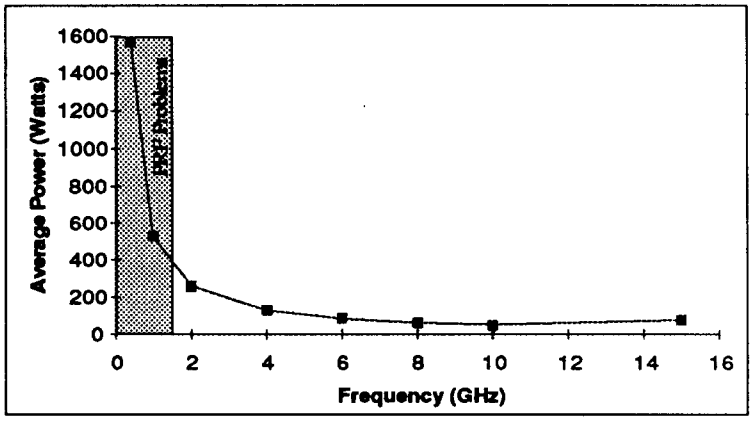

Figure 5.4.4.1: Average Power vs. Frequency

Figure 5.4.4.1 is somewhat misleading because in practice the antenna area design will not be fixed. A more likely situation is that the swath width required will be fixed. Another form of equation (5.4.4.4) is presented which takes into account the range swath. Separating the effective area into:

$$A_e = e_a \cdot D_a \cdot D_r \tag{5.4.4.5}$$

where:

D_r - is the range dimension of the antenna

and approximating the slant range swath width as:

$$W_r \approx \frac{\lambda}{D_r} \cdot R \tag{5.4.4.6}$$

where:

W_r - is the slant range swath width

Then equation (5.4.4.4) can be rewritten as:

$$SNR_1 = \frac{P_{avg} \cdot e_a^2 D_a^{\,2} \cdot \sigma^o \cdot \lambda \cdot \rho_{rg} \cdot L_{tot}}{2 \cdot (4 \cdot \pi) \cdot W_r^2 \cdot R \cdot k \cdot F \cdot T_s \cdot V_{st}} \tag{5.4.4.7}$$

Equation (5.4.4.7) says that for a fixed slant range swath, average power required is linearly proportional to frequency.

Figure 5.4.4.2 presents the relationship between power and altitude. For a constant look angle, range and

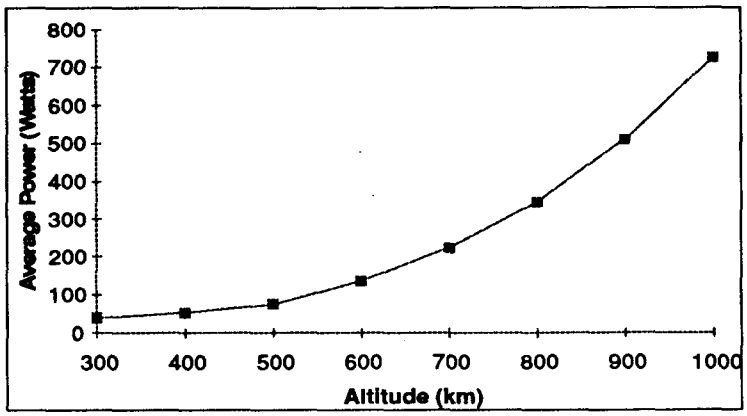

Figure 5.4.4.2: Average Power vs. Altitude

height are linearly related. This curve is essentially cubic with altitude. The field-of-view is also linearly related to the altitude. At lower altitudes the beamwidth needs to be larger to maintain the proper field-of-view, therefore, the antenna area is smaller. At higher altitudes than depicted on this chart, the antenna area may need to be larger to avoid PRF problems.

The relationship between power and look angle is presented in Figure 5.4.4.3. The increase in power is

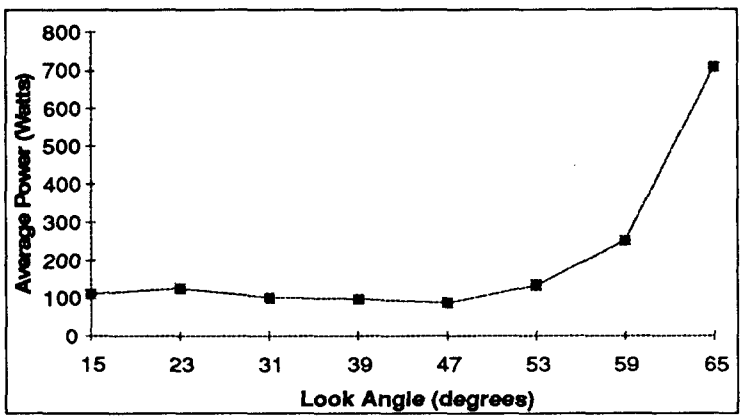

Figure 5.4.4.3: Average Power vs. Look Angle

from the increase in range with look angle. The curve stays approximately level, because the antenna width can slightly increase to maintain the ground swath. The dip in the curve is due to "quantization" in the antenna width specification.

Another problem associated with high look angles is that for typical distributed targets, the radar cross-section drops dramatically for higher incidence angles. This means more power must be used to detect the same distributed target at larger look angles. Equation (5.4.4.4) buries this inside the $\sigma_n{}^0$ parameter, which is a detection or sensitivity parameter. (There is a similar issue associated with frequency not discussed here.)

Figure 5.4.4.4 shows the dependence of power on reciprocal of the ground range resolution.

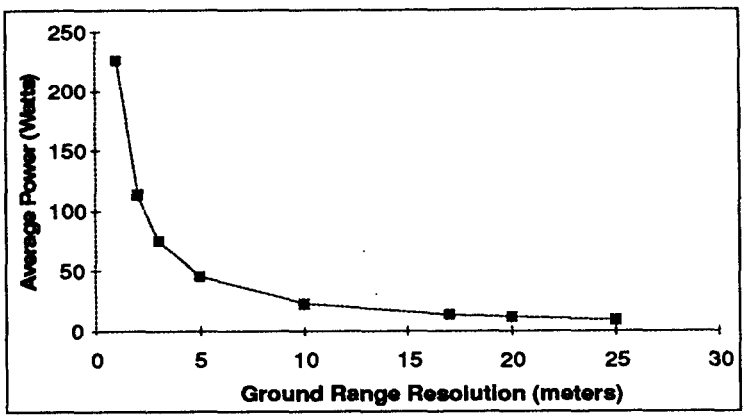

Figure 5.4.4.4: Average Power vs. Ground Range Resolution

Figure 5.4.4.5 is a plot of power versus ground swath width. The dependence on ground swath comes

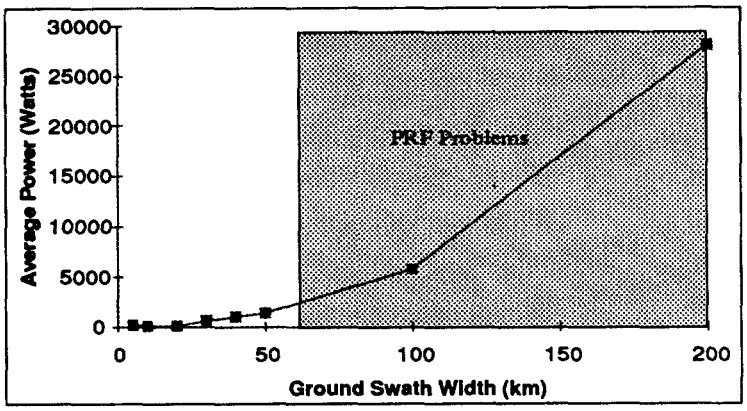

Figure 5.4.4.5: Average Power vs. Ground Swath Width

from both the change in far range and the antenna area adjustments to achieve the swath width field-of-view.

5.5 Propagation Issues

Any space borne radar must look through the earth's ionosphere in order to image objects on or near the ground. The ionosphere consists of an ionized plasma which will interact with any electromagnetic wave propagating through it. This interaction is particularly strong at UHF frequencies but decreases for higher microwave frequencies. The effects caused by this interaction can be classified into three categories:

1) Dispersion effects, which affect usable signal bandwidths,
2) Polarization effects, which will determine how well fully polarimetric measurements can be performed,

and

3) Non-deterministic spatial and time variations, which will complicate the compensation of the effects of 1) and 2).

The dispersion and polarization effects are discussed in some detail in [11] and results from that study will be summarized here. The non-deterministic spatial and time variations have been addressed, for example, in [15], [41], [52].

The effects of the ionosphere will be most pronounced at the lower (UHF and L-Band) frequencies, will limit the usable bandwidth (resolution), and will make achieving high-quality polarimetrics difficult. For example, in order to achieve 1.5 m resolution (~100 MHz bandwidth) with a uniformly weighted chirp for a typical ionospheric condition, a center frequency of about 1 GHz would be needed if quadratic phase errors are to be limited to around 100°.

5.5.1 Dispersion Effects

The wavenumber, k, (and the propagation velocity) of an electromagnetic wave in the ionosphere is a function of frequency $\omega = 2\pi f$ and can be described in a power series

$$k = \sum_{n=0}^{\infty} \alpha_n \left(\frac{\omega - \omega_0}{\Delta\omega} \right)^n \qquad (5.5.1.1)$$

where ω_0 is the center frequency and $2\Delta\omega$ is the signal bandwidth. For a non-dispersive medium, only the constant and linear terms would be present. For the ionosphere, the series converges rapidly and only a few terms (usually $n=2$ or 3) are needed. The coefficients α_n depend on the electron distribution in the ionosphere, the direction of propagation with respect to earth's magnetic field, and the polarization of the wave, in addition to the center frequency ω_0. A derivation of the exact form for k is given in [9].

The electron density in the ionosphere depends on the altitude, the time of day, the time of the year, the condition of the sun, the time during the sunspot cycle, and the latitude of the point of interest. The condition of the sun is described by several measures, one of the simplest of which is the sunspot number. Fig. 5.5.1.1 shows the daily sunspot numbers for a portion of Solar Cycle 22 (the current cycle) [59]. The sunspot number (and the electron density with it) varies erratically from day-to-day and follows a cycle of roughly eleven years. The results summarized here are based on a "typical" ionosphere described by the International Reference Ionosphere IRI 79 [45] for Dakar, Senegal at noon in December when the sunspot number is 100. The electron density profile for this model is shown in Fig. 5.5.1.2 along with the profiles for midnight and sunrise. Significant variation throughout the day is apparent. The main point to be taken from these figures is that the electron density profile (and thus the wavenumber k) is quite variable and erratic and not subject to accurate prediction.

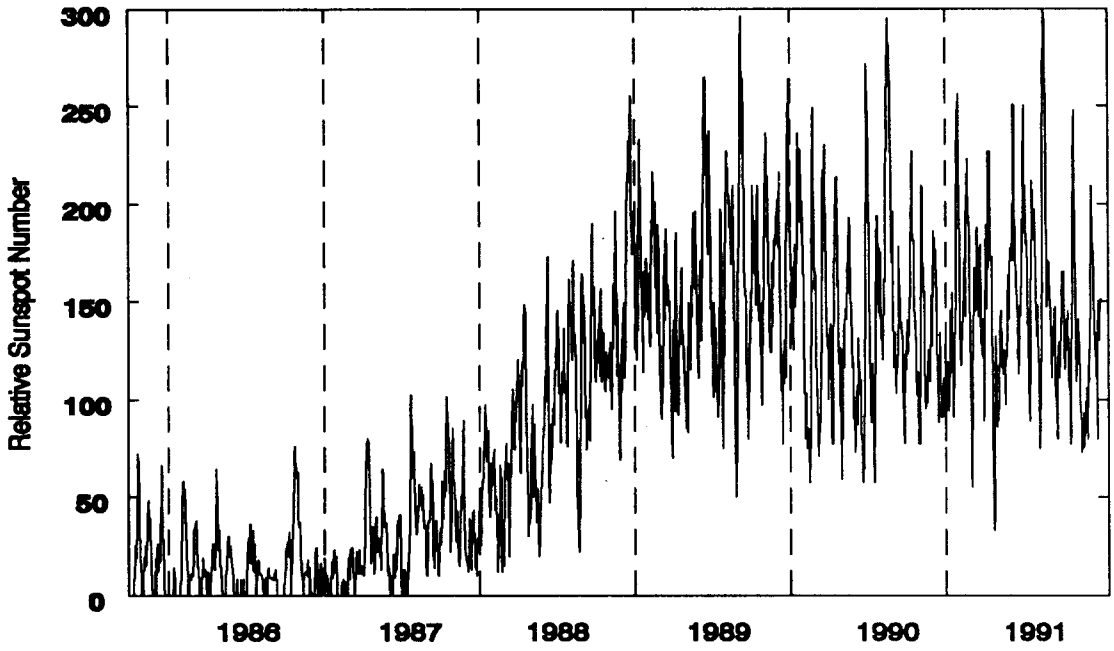

Fig. 5.5.1.1: Daily sunspot numbers as derived by the Sunspot Index Data Center in Brussels, Belgium for a portion of Solar Cycle 22 (1986-1991) [59]

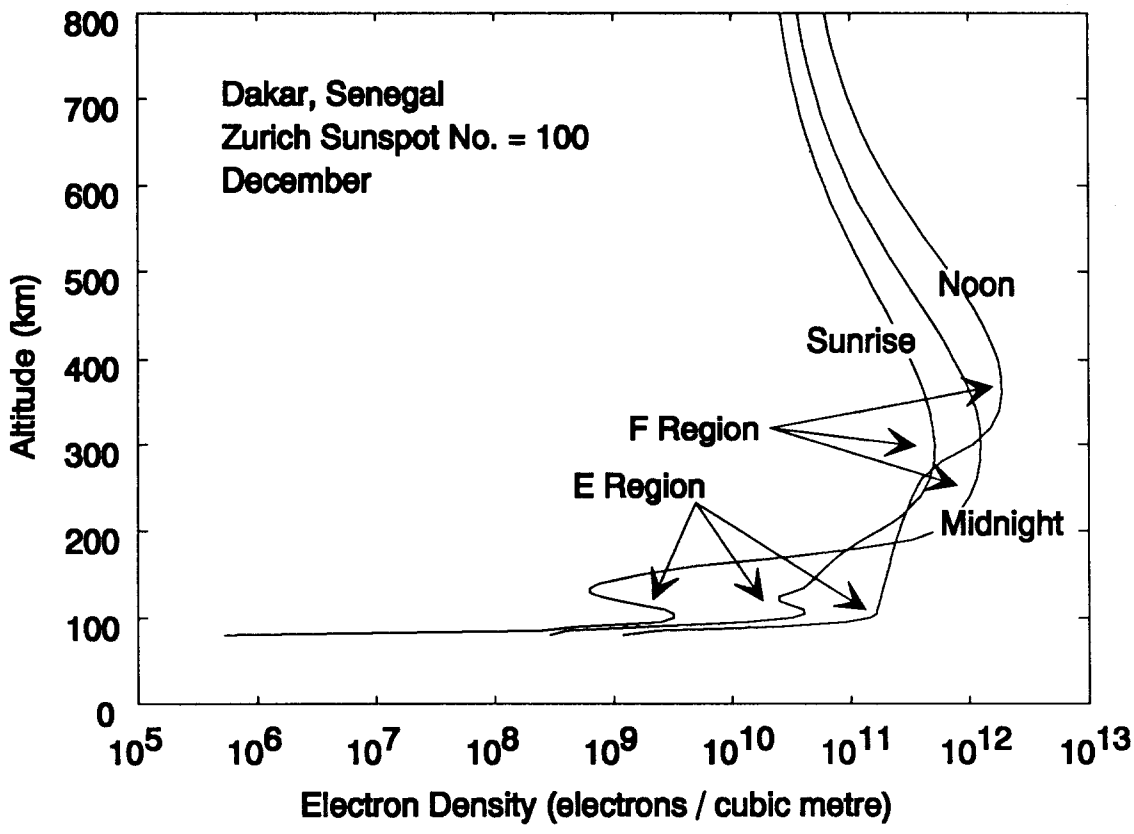

Fig. 5.5.1.2: Typical electron density distribution for a moderately active ionosphere, based on the International Reference Ionosphere IRI 79.

The total phase accumulated by a spectral component of the signal is given by the wavenumber integrated over the two-way path plus the phase contribution of the scatterer at the earth's surface. Because of the large distances involved, small non-linearities in $k(f)$ will result in much larger non-linearities of the phase as a function of frequency. In addition, the total path length increases as the look angle increases, and the problem will be more severe for larger look angles. Table 5.5.1.1 shows the peak quadratic-phase error for various bandwidths at center frequencies from P-band to X-band.

Table 5.5.1.1

Peak Quadratic-Phase Error

Dakar Ionosphere Model, 30° Look Angle, Altitude=500 km

	Chirp Bandwidth (MHz)				
Frequency (MHz)	25	50	100	200	1000
425	81.0°	324.9°	1315.0°	5516.0°	---------
1275	3.0°	12.0°	48.0°	193.0°	5762.0°
5300	0.0°	0.2°	0.7°	2.7°	67.4°
9500	0.0°	0.0°	0.1°	0.5°	11.6°

The primary effect of quadratic phase errors is to broaden the compressed pulse. The amount of quadratic phase which can be tolerated depends on the weighting of the frequencies in the chirp. As the phase error increases, weighted chirps eventually perform better in terms of resolution and contrast than the uniform-weighted chirp. For example, even though the compressed Hamming-weighted chirp is wider than the compressed uniform-weighted chirp when no phase errors are present, it is narrower (at the -10 dB level) when the peak quadratic-phase error exceeds 100°. As the phase error increases, sidelobes also increase and contrast will decrease. Cubic-phase error causes deteriorated sidelobe performance and increases the sidelobes asymmetrically. Table 5.5.1.2 shows the normalized width of the compressed Hamming-weighted chirp for various values of peak quadratic-phase error. The widths are normalized to the -3 dB width of the compressed uniform-weighted chirp with identical bandwidth and no phase error.

Table 5.5.1.2

Normalized Width of Compressed Hamming-Weighted Chirp

	Peak Quadratic-Phase Error				
Amplitude	0°	50°	100°	200°	300°
-3 dB	1.51	1.54	1.66	2.27	3.10
-10 dB	2.67	2.77	3.11	4.22	5.76
-20 dB	3.60	3.89	4.54	6.36	8.38
-30 dB	4.20	4.81	6.03	8.28	10.7

5.5.2 Polarization Effects

The velocity of propagation in a plasma is dependent on the polarization of the wave. There are two preferred or eigen polarizations which propagate at their own distinct velocities. When the direction of propagation is along the direction of the static magnetic field, the eigen polarizations are left- and right-hand circular. When the direction of propagation is perpendicular to the static magnetic field, one eigen polarization (ordinary wave) is linear with the electric field vector in the direction of the static magnetic field. The second eigen polarization (the extraordinary wave) is highly elliptical with a very small component in the direction of propagation. Since these eigen polarizations propagate with slightly different velocities, any wave which is made of a combination of the eigen polarizations will suffer polarization distortion as it propagates through the ionosphere because the relative phase between its components will change. (This effect is known as Faraday rotation.)

In order to achieve good polarimetric measurements, it is desirable to use the eigen polarizations when the phase difference between the two polarizations will be significant. In order to enhance the polarization isolation through calibration techniques [10] or to convert a scattering matrix measured with one polarization basis to a different basis, a coherent measurement is required. Phase accuracy of 5° is required to obtain about 20 dB improvement in polarization isolation after calibration.

Table 5.5.2.1 shows the phase difference for the eigen polarizations at various frequencies and look angles for a typical ionospheric condition. The results represent two-way propagation at an altitude of 500 km. The wave vector is assumed to lie in the plane perpendicular to the geomagnetic equator. Clearly, the phase difference present at UHF is large enough to preclude significant polarization-isolation improvement through calibration even at the small 20° look angle. Also, because of the larger phase differences, it is clear that Faraday rotation will be a problem at UHF for larger look angles. L-Band shows good performance for look angles as large as about 30°, while C-Band has good performance to nearly 60°. At frequencies around X-Band, the eigen polarizations propagate at very nearly the same velocity, and there is little difference between them.

Table 5.5.2.1

Phase Difference Between Eigen Polarizations

Dakar Ionosphere Model, 0° Geomagnetic Latitude, Altitude=500 km

	Look Angle (measured from nadir)				
Frequency MHz	20°	30°	40°	50°	60°
425	13.8°	31.6°	74.8°	203.7°	836.4°
1275	1.5°	3.5°	8.3°	22.6°	93.0°
5300	0.1°	0.2°	0.5°	1.3°	5.4°
9500	0.0°	0.1°	0.1°	0.4°	1.7°

5.5.3 Non-Deterministic Effects

The ionosphere is inhomogeneous and, as the synthetic aperture is produced, the electromagnetic wave will propagate through portions of the ionosphere with different properties. The existence of spatial variations is well known, and considerable study has been devoted to this problem [15], [41]. Because the electrons diffuse along the magnetic-field lines, the ionosphere develops tube-like irregularities along the field lines. Empirical data indicates that the worst variations are in the auroral zone (polar latitudes) and the equatorial zone. Because of the diffusion of electrons along the magnetic-field lines, the irregularity

shows greater spatial-correlation lengths along the magnetic east-west directions than along the north-south directions. The irregularities are particularly strong at UHF and can be strong through C-Band [15]. From observation of radio stars, it has been determined that signals received at locations separated by about 1 km are strongly correlated while signals received at locations 200 km apart show no correlation [41].

Several methods have been proposed and implemented for correcting random phase errors in synthetic-aperture images by Brown, Ghiglia, Eichel and Jakowatz [12], [25], [33]. These methods have been developed to compensate phase errors introduced across the synthetic aperture and have been used traditionally for one-dimensional correction. Because of the dispersion introduced by the properties of the ionosphere, corrections will be needed in the range direction (compressed-chirp direction) as well. Recently, a two-dimensional phase correction algorithm has been proposed and demonstrated [29] by Ghiglia and Mastin.

5.6 Antennas and Beam Steering

Antennas with beams that can be steered fall into two general categories: 1) electrically-steered arrays and 2) mechanically-steered arrays. Electrically-steered arrays can be phased-array antennas which use phase shift and time delay to steer the beam or frequency-steered arrays which take advantage of the change in wavelength as frequency is changed to steer the beam. Mechanically-steered arrays can move the beam by moving the entire antenna or by moving the feed of a fixed reflector or lens antenna. Table 5.6.1 compares these general classes of antennas and lists various advantages and disadvantages of each class.

Table 5.6.1
Comparison of Steerable Beam Antenna Classes

Antenna Class	Advantage	Disadvantage
Phased Array	Near instantaneous beam steering Can support wide bandwidth Can support multiple beams Transmit and receive characteristics can be different	Complex circuitry Expensive Beam characteristics vary with beam direction
Frequency-Steered Array	Near instantaneous beam steering Moderately simple structure and circuitry Can support multiple beams (each beam separated by frequency)	Narrow signal bandwidth (bandwidth proportional to beamwidth) Antenna bandwidth must be much larger than signal bandwidth
Mechanically-Steered Antenna (entire antenna)	Simple structure Beam characteristics independent of beam direction	Slow beam steering
Mechanically-Steered Feed	Moderately simple structure	Moderately slow beam steering Beam characteristics depend on beam direction

Space-based antennas must be lightweight and deployable while still maintaining tight tolerances for surface shape, element position, feed location, etc. The antenna will be subjected to temperature extremes as it moves in and out of the earth's shadow (unless it is in a sun-synchronous orbit) and as its orientation with respect to the sun changes. In addition, the environment near the earth contains a large number of micrometeors; these can collide with the antenna and cause surface damage. Thus, the mechanical design

of the antenna is very critical to the success of the antenna in space-based SAR applications. An overview of the mechanical considerations as well as brief descriptions of proposed and deployed space-based antennas are contained in [15]. However, the mechanical aspects of the design will not be discussed here. This omission should not be construed to mean that the mechanical aspects of the antenna design are trivial and straightforward. The mechanical design is very demanding and requires state-of-the-art analysis, construction techniques, and materials.

5.6.1 Phased-Array Antennas

The design of a phased-array antenna can be a very complex task. Because the array consists of closely spaced radiating elements, the mutual coupling between elements becomes an important consideration. The effects of mutual coupling will change as the beam is steered and as the frequency is varied, and the design of appropriate radiating elements to support broad bandwidths and large steering ranges is challenging. Because of the mutual-coupling effects, the complete and accurate analysis of phased-array performance is also very complex. However, simple design equations are available to aid in determining an array specification and its nominal performance for a specific application. In order to allow the evaluation of phased-array antenna performance as parameters are changed, simple formulae are given. Some of these embody simplifications and assumptions and should not be construed to give a complete and accurate description of the array performance.

In order to provide simple design equations, the array will be assumed to have elements located on an equally spaced rectangular grid with beam scanning along the direction of one of the grid coordinates. Other grid arrangements, such as triangular grids, are useful but will not be addressed here. In order to avoid the appearance of grating lobes (an undesired radiation lobe comparable to the main lobe), the element spacing d along each grid direction should be [58]:

$$\frac{d}{\lambda} < \frac{1}{1+\sin\theta_{max}} \tag{5.6.1.1}$$

where λ is the free-space wavelength and θ_{max} is the maximum scan angle along this grid direction measured from broadside. When the spacing does not satisfy (5.6.1.1), grating lobes will appear at θ_g when the beam is steered to $\theta > \theta_{max}$ [58]:

$$\sin\theta_g = \sin\theta \pm \frac{n\lambda}{d} \tag{5.6.1.2}$$

where n is an integer.

Because an array is a periodic structure, it can support surface waves. If a surface wave is excited, energy will go into it rather than be radiated. Surface waves can be excited when the beam is steered to certain angles if the element spacing is not chosen properly. Since the energy does not go into the radiating mode, the array will be blind at these angles. To avoid array blindness within the region of scan, the spacing should be chosen so that [58]:

$$\frac{d}{\lambda} < \frac{1}{c/v + \sin\theta_{max}} \tag{5.6.1.3}$$

where c is the velocity of light in vacuum and v is the surface-wave velocity along the array.

The array gain when steered to angle θ is given by:

$$G = 4\pi \frac{\eta_a \eta_e A \cos\theta}{\lambda^2} \tag{5.6.1.4}$$

where η_a is the aperture efficiency (determined by the illumination taper), η_e is the element efficiency, and A is the array area. For a uniformly illuminated array containing N elements along one grid direction, the beamwidth along that grid directions when scanned θ from broadside can be estimated from [9]:

$$\theta_{3dB} \cong 51° \frac{\lambda}{Nd \cos\theta} . \tag{5.6.1.5}$$

If the array is steered with constant-phase phase shifters without the use of subarrays, the beam will move from θ to θ' as the frequency is shifted from the design frequency f_c to f according to [9]:

$$\theta' = \sin^{-1}\left(\frac{f_c}{f}\sin\theta\right). \tag{5.6.1.6}$$

For such an array, the operating bandwidth of the array is a function of the scan angle θ and is given by [9]:

$$BW \cong f_c \frac{0.886\delta\lambda}{Nd \sin\theta} \tag{5.6.1.7}$$

where f_c is the design center frequency and δ is the fraction of the beamwidth representing the tolerable beam-steering error:

$$\delta = \frac{|\theta' - \theta|}{\theta_{3dB}} . \tag{5.6.1.8}$$

This bandwidth can be increased by dividing the array into subarrays which have the desired bandwidth given by (5.6.1.7) with $N=N_S$, the number of elements in the subarray. The subarrays must then be fed with time-delay shifters. The subarray dimensions are obtained by specifying the allowable main-lobe amplitude change α (in dB) as the frequency is changed from $f=f_C-\Delta f$ to $f=f_C+\Delta f$ at the maximum scan angle θ_S. The number of subarray elements along the dimension of the scan is:

$$N_s \cong \frac{\sqrt{10\left(1-\sqrt{1-\frac{6}{5}\left(1-10^{-\alpha/20}\right)}\right)}}{|q|} \tag{5.6.1.9}$$

where q is:

$$q = \frac{\pi d}{\lambda_c}\frac{\Delta f}{f_c}\sin\theta_s , \tag{5.6.1.10}$$

and λ_C is the wavelength at the center frequency f_C. The error in the approximation in (5.6.1.9) is less than 10% for $\alpha < 15$ dB.

For an array built with subarrays, the main lobe will scan to:

$$\theta' \equiv \theta + \frac{\frac{f_c}{f} - 1}{N_A^2 + 3} \tan\theta \text{ (radians)} \qquad (5.6.1.11)$$

where N_A is the number of subarrays along the direction of the scan. Frequency-dependent subarray lobes associated with the use of constant-phase phase shifters within the subarrays will occur at:

$$\theta_{gm} \equiv \sin^{-1}\left(\sin\theta_s + \frac{m\lambda_c f_c}{N_s df} \right) \qquad (5.6.1.12)$$

where m is the number of the lobe. The lobes will have an amplitude with respect to the peak of the main lobe given by:

$$G_{gm} \equiv \left| \frac{\sin(-N_s q \pm m\pi)}{N_s \sin\left(-q \pm \frac{m\pi}{N_s}\right)} \right| . \qquad (5.6.1.13)$$

An example of the subarray-lobe phenomena is illustrated in Fig 5.6.1.1 for a uniformly-illuminated linear array of 64 subarrays containing 6 elements each when the array is scanned to $\theta = 60°$.

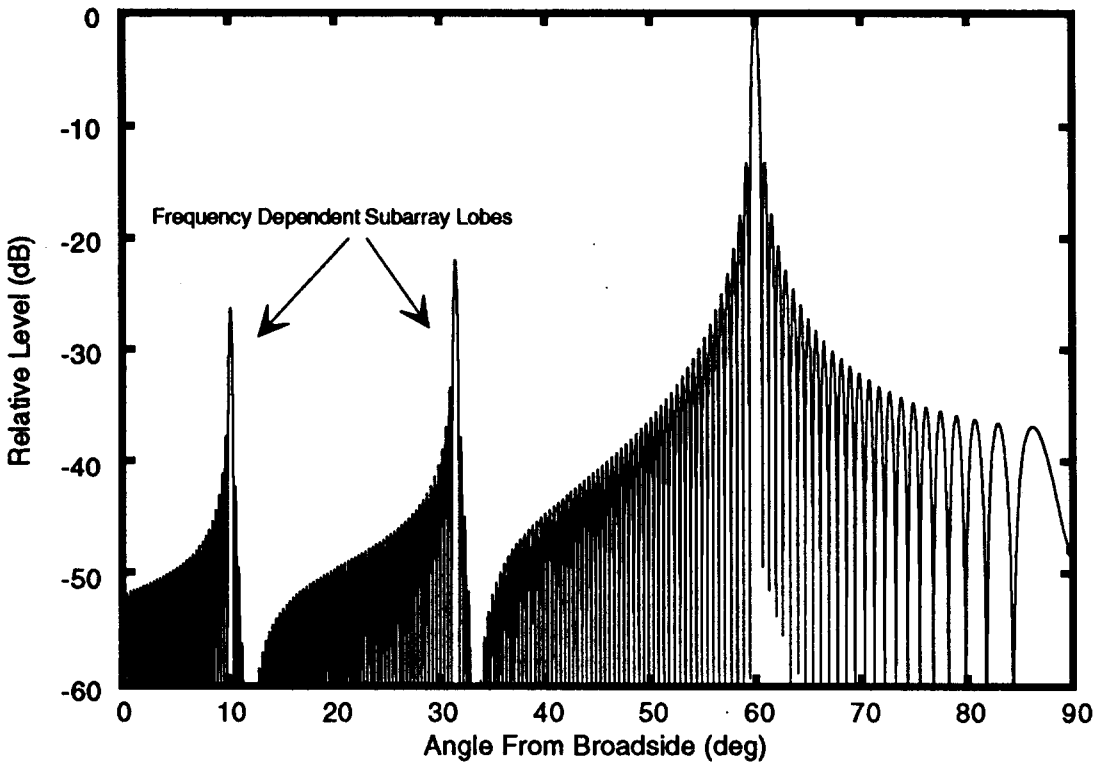

Fig. 5.6.1.1 Radiation pattern of a uniformly illuminated linear array comprised of 64 subarrays each containing 6 elements when scanned to $\theta = 60°$.

Quantization errors in the steering phase will affect the array performance. If phase shifters with p bits are used, the gain will be reduced by [58]:

$$\Delta G \cong \frac{1}{3}\frac{\pi^2}{2^{2p}} . \tag{5.6.1.14}$$

The rms sidelobe level will be [58]:

$$Sidelobe_{rms} \cong \frac{5}{2^{2p}N} . \tag{5.6.1.15}$$

The beam can be steered in increments of $\delta\theta$ [58]:

$$\frac{\delta\theta}{\theta_{3dB}} \cong \frac{9}{2^{p}N} . \tag{5.6.1.16}$$

Unwanted lobes in the radiation pattern, called phase-quantization lobes, can occur at θ_q [58]:

$$\theta_q = \sin^{-1}\left(\sin\theta - \frac{\lambda}{r}\right) \tag{5.6.1.17}$$

where r is the length of the period of the phase ripple (in same units as λ). The peak phase-quantization lobe amplitude is [58]:

$$Lobe_{phase-quantization} \cong \frac{\pi}{2^{p+1}} \sqrt{\frac{\cos\theta_q}{\cos\theta}} \,. \qquad (5.6.1.18)$$

The phase-quantization lobes can be reduced by making the phase error across the array uncorrelated.

The number of active elements (T/R modules) in a large array can be reduced by only feeding some elements and terminating others [58]. The distribution of active elements should be chosen randomly. Such an array will have a beamwidth corresponding to the full aperture but the gain will be reduced by the ratio of the number of excited elements to the number of total elements in the array. Since the beamwidth does not change while the gain is reduced, the side lobe level must increase by a corresponding amount.

5.6.2 Multiple-Beam Phased-Array Antennas

Multiple beams for signal reception can be achieved in two ways: 1) multiple thinned arrays and 2) multiple-port feed networks. For multiple transmit beams, the multiple thinned-array concept is most efficient because it evenly distributes the power requirements among the T/R modules. The use of a multiple-port feed network for transmit can result in the requirement that some T/R modules provide many times the nominal module RF output power while others produce very little power. The power distribution would depend on the directions to which the beams are steered.

The multiple thinned-array concept provides m beams from an array of N elements by associating m non-overlapping sets of N/m uniformly distributed, randomly selected elements with m independent arrays. Each array could be steered to independent locations and each array would have a beamwidth consistent with the full dimensions of the array. However, each of the m beams would have lower gain than if the entire array were utilized (by a factor of $1/m$). The reduced gain is caused by increased side lobe levels as compared to the side lobes achievable with the entire array. A complicating aspect of this approach (which has not been addressed) is the effect of mutual coupling between the elements used to produce one beam and the elements used to produce another.

Multiple-port feed networks can be designed to utilize all elements in the array for each beam while still forming multiple beams. This approach is illustrated in Fig. 5.6.2.1 which illustrates an eight-element subarray designed to provide a single beam for transmit and three offset beams for receive. The receive beams can be steered independently to directions slightly different from the direction of the transmit beam.

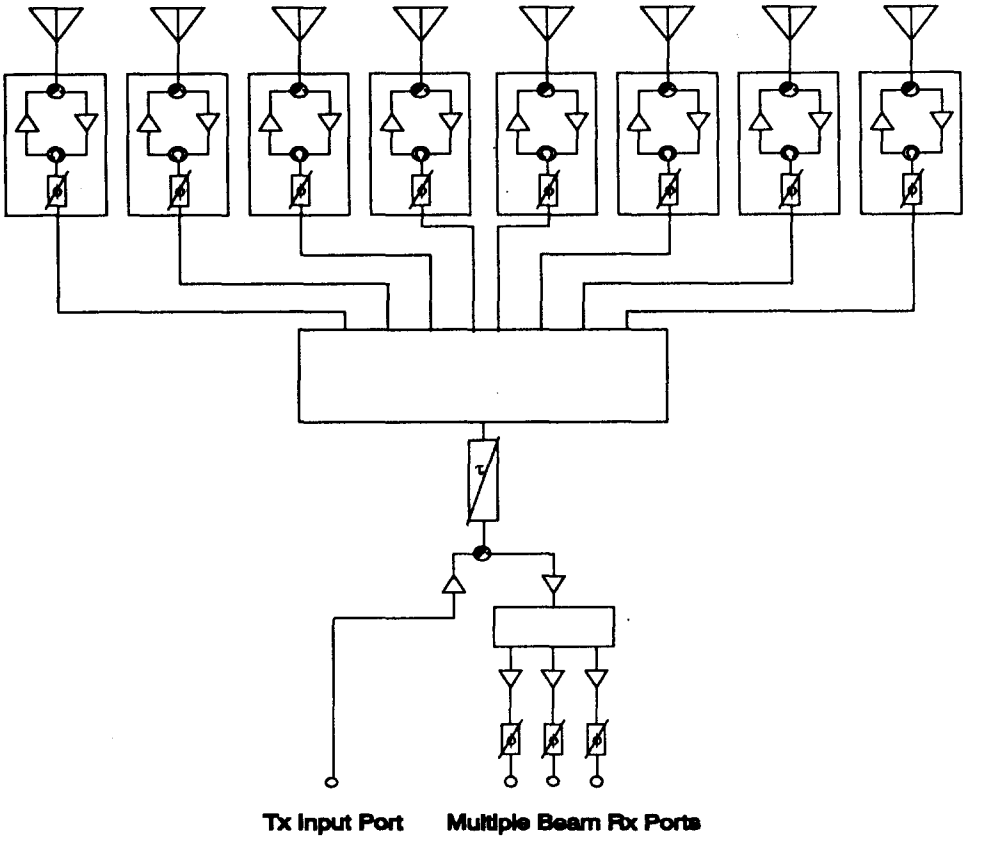

Fig. 5.6.2.1 Block diagram of an eight-element subarray designed to provide one beam for transmit and three independent beams for receive. The receive beams can be independently placed near the direction of the transmit beam.

A subarray of the type illustrated in Fig. 5.6.2.1 will support a system where a single, broad transmit beam is formed from a portion (for example, the center third) of the array while multiple, overlapped receive beams are formed using the entire array. The receive beams will be much narrower than the transmit beam and by overlapping them, the entire region illuminated by the transmit beam can be covered.

The multiple thinned-array concept can be utilized to provide a method of utilizing all of the active array elements of the full array during transmit while producing a much broader beamwidth than usually obtained by the full-sized array. The broad beam is formed by steering multiple narrow beams to slightly different positions so that they overlap slightly while ensuring that they are precisely in phase with each other. Fig. 5.6.2.2 illustrates the average pattern (ensemble average over all arrays) obtained from a 15 m linear array organized as ten uniformly distributed random arrays (no overlapping elements). The array is operated at 9.5 GHz (X-Band). Each beam is steered 0.1° from its nearest neighbor. This array has a nominal beamwidth of about 1.0° rather than the 0.1° beamwidth which would be obtained if all elements were fed uniformly and in phase.

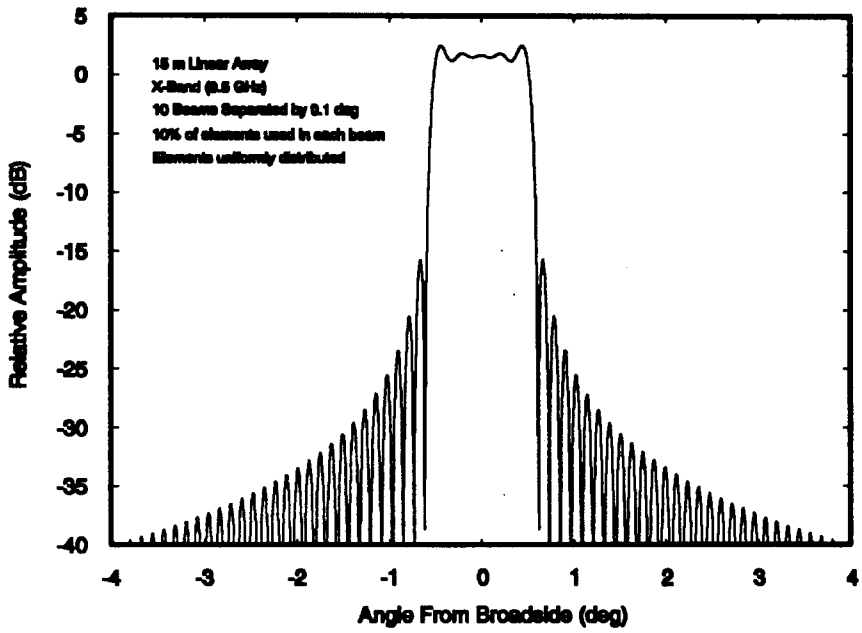

Fig. 5.6.2.2 Radiation beamwidth obtained from a 15 m linear array at X-Band when partitioned into 10 uniformly distributed, randomly thinned, non-overlapping arrays. The individual beams ($\approx 0.1°$ beamwidth) are steered $0.1°$ apart so that they overlap, forming the $1.0°$ beam shown here.

5.6.3 Frequency-Steered Antennas

If the elements of a linear array are series-fed as illustrated in Fig. 5.6.3.1, then the beam will move as the frequency is changed. This is because the phase difference between the excitation at each element increases as the frequency increases. The beam will point in the direction θ measured from broadside:

$$\theta = \sin^{-1}\left(\frac{s}{d}\lambda\left(\frac{1}{\lambda_g} - \frac{1}{\lambda_{gm}}\right)\right) \tag{5.6.3.11}$$

where d = the element spacing,

s = the length of the transmission line between elements,

λ_g = the wavelength in the transmission line,

λ_{gm} = the wavelength in the transmission line when the beam points to broadside,

and λ = the wavelength in free space ($\lambda = c / f$).

The 3 dB beamwidth in the direction of scan is given by (5.6.1.5). If the allowable beam drift, $\Delta\theta$, is specified, then the signal bandwidth of the array when non-dispersive transmission line is used to connect the elements is:

$$BW \cong \frac{1.77\lambda_{gm}}{Ns} f \frac{\Delta\theta}{\theta_{3dB}}. \tag{5.6.3.2}$$

The bandwidth becomes smaller as the size of the array, N, increases and as the length of the transmission line, s, between the elements increases. The rate at which the beam steers can be controlled by the length of the transmission line, s :

$$\frac{d\theta}{df} = \frac{1}{\cos\theta}\frac{s}{d}\left(\frac{c}{f^2\lambda_{gm}} + \frac{d}{df}\left(\lambda/\lambda_g\right)\right) \qquad (5.6.3.3)$$

which applies for both dispersive and non-dispersive transmission lines. Increasing s will increase the rate at which the beam steers but it will also decrease the bandwidth.

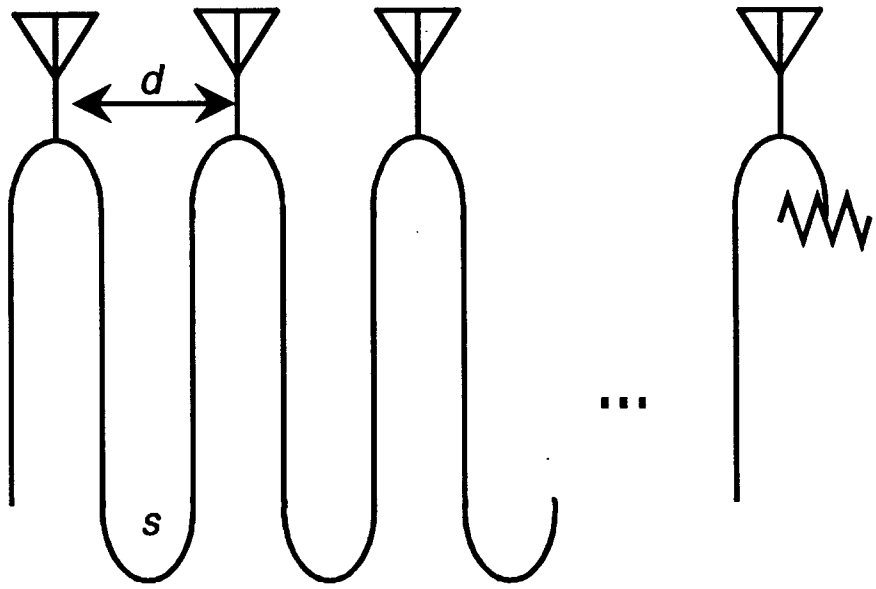

Fig. 5.6.3.1 Schematic representation of a linear-fed frequency-steered array.

5.6.4 Mechanically-Steered Antennas

Large passive arrays, large lens antennas, or parabolic-reflector antennas can be used when steering rates are not critical. These antennas can be steered either by moving the antenna independently of the satellite or by re-positioning the entire satellite. Because of the inertia involved, this method of steering will naturally be slow. The advantages, of course, are a simpler antenna and a beam shape and side lobe levels which do not change as the beam is steered.

Lens and reflector antennas can be steered somewhat by moving the feed away from the focal point. Since the feed structure will be smaller, its inertia will be less than that of the entire antenna or satellite. Thus, steering the beam by moving the feed will be somewhat faster than steering the entire antenna. However, the beam shape and sidelobe levels deteriorate as the feed is moved away from focus. The range over which the antenna can be steered is thus limited. The degradation of the radiation pattern is dependent on the F/D ratio (focal length / diameter) of the reflector or lens. Larger scan angles are possible with larger F/D ratios. Practical scan ranges for offset-feed steering range from about 6 beamwidths for F/D = 0.4 to about 16 beamwidths for F/D = 1 [46]. In these cases, the sidelobe ratio degraded more than 10 dB from broadside scan to maximum scan. In the case of the short focal-length reflector, the peak sidelobe was less than 10 dB below the main beam when scanned to 6 beamwidths from broadside. Offset-feed steering is only practical for very limited scan ranges.

6.0 Case Studies

This section presents two spaceborne SAR parameter case studies. One case is for Ku-band, and the other is P-band. The basic assumptions for this section are:

1) The total launch weight is under 2000 kg for low-earth orbit (roughly, a Taurus class launch vehicle).

2) The total launch to payload ratio is 4:1 (a good "rule-of-thumb"). This means that we are limiting the SAR payload to about 500 kg total weight, including the antenna.

3) The SAR weight is estimated as 3 kg/W of average transmitter power. The antenna weight is estimated as 10 kg/m^2.

4) Prime DC power required is estimated to be 10 times the average transmitter power required.

5) The numbers derived in this study assume that matched filter range processing and line-by-line azimuth processing are performed, even though this is computationally expensive. Other SAR image formation techniques may be possible in some cases, but these case studies do not address this issue.

6) No on-board image formation is assumed.

7) No data compression technique is assumed.

8) Only traditional SAR techniques are considered (i.e., not the techniques described in section 5.2).

9) Resolutions are assumed to be "square" in the slant-plane.

10) Prudent design margins were not necessarily used in this study.

Certainly, the actual values used for all of these parameters could be argued. In addition, many of the parameters need to be examined in more detail. For example, the issues covered in sections 5.3.1 and 5.3.5 need to be considered in an actual design. Only a detailed design study will reveal the actual weights and parameters. This study focuses mainly on revealing trends and relationships rather than detailed designs.

6.1 Ku-Band Case Study

Table 6.1.1 presents the nominal design for the Ku-band case study. Section 6.1.1 discusses varying the resolution. Section 6.1.2 examines varying the look angle.

6.1.1 Ku-Band Case Study - Varying Resolution

The affects of varying the resolution, can be seen from figures 6.1.1.1, 6.1.1.2, 6.1.1.3, and 6.1.1.4. These are plots of the weight, swath, data rate, and power, respectively, for different resolutions at Ku-band.

In figure 6.1.1.2, the ground swath width curve levels off at 10 m resolution. This is because the minimum antenna width was set at 0.5 m. In theory, the antenna width would become smaller and smaller to achieve a larger and larger swath width. In addition, in theory the antenna length could become longer and longer. For this study, the maximum antenna length is frozen at 10m. In practice, the

Table 6.1.1: Base System - Ku-Band

Subject	Item	Units	Value
Orbit:			
	Orbit Inclination	degrees	97.4
	Altitude	km	500
	Satellite Velocity	m/sec	7616
	Ground Track Velocity	m/sec	7039
Scene:			
	Look Angle - mid	degrees	45
	Slant Range Res.	m	3
	Ground Range Res. - near	m	3.9
	Azimuth Res.	m	3
	Swath Width (ground)	km	7.6
	Swath Width (slant)	km	5.8
	Range - mid	km	737
	Squint Angle to Scene Center	degrees	90
Radar:			
	Frequency	GHz	15
	Pulse Width	μs	30
	Bandwidth	MHz	50
Ambiguity Information:			
	Maximum PRF	Hz	8373
	Minimum PRF	Hz	2539
	Actual PRF	Hz	3000
	Yaw Angle/PRF Ambiguity	degrees	0.16
	Pitch Angle/PRF Ambiguity	degrees	0.16
Processing Info:			
	Aperture Length	km	2.5
	Aperture Time	sec	0.32
Target Info:			
	Target type	Point/Distributed	Distributed
	Noise equivalent, $\sigma_n{}^0$	dB	-25
Antenna/Receiver Parameters:			
	Length	m	6
	Azimuth Beamwidth - 3 dB	degrees	0.19
	Width	m	1.95
	Elevation Beamwidth - 3 dB	degrees	0.59
	Efficiency		0.65
	Receiver Noise Factor	dB	2.8
	System Noise Temperature	degrees Kelvin	290
Power Losses:			
	Total Losses Assumed	dB	8.8
Tx Power Requirements:			
	Average Txmitter Power - Far Range	W	124
	Peak Txmitter Power - Far Range	W	1380
Weight Estimate:			
	Total Weight	kg	490
Data Rate:			
	Bits per Sample	bits	5
	Data Rate	Mbps	119

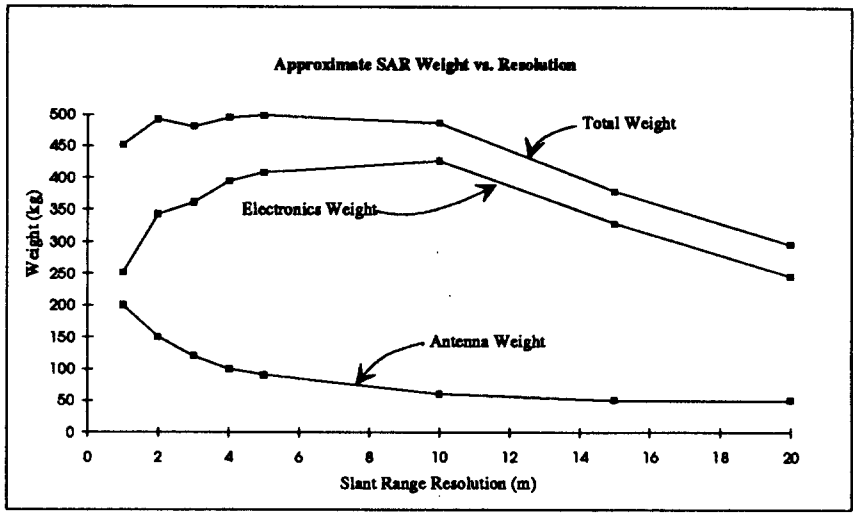

Figure 6.1.1.1: Total SAR Weight vs. Resolution

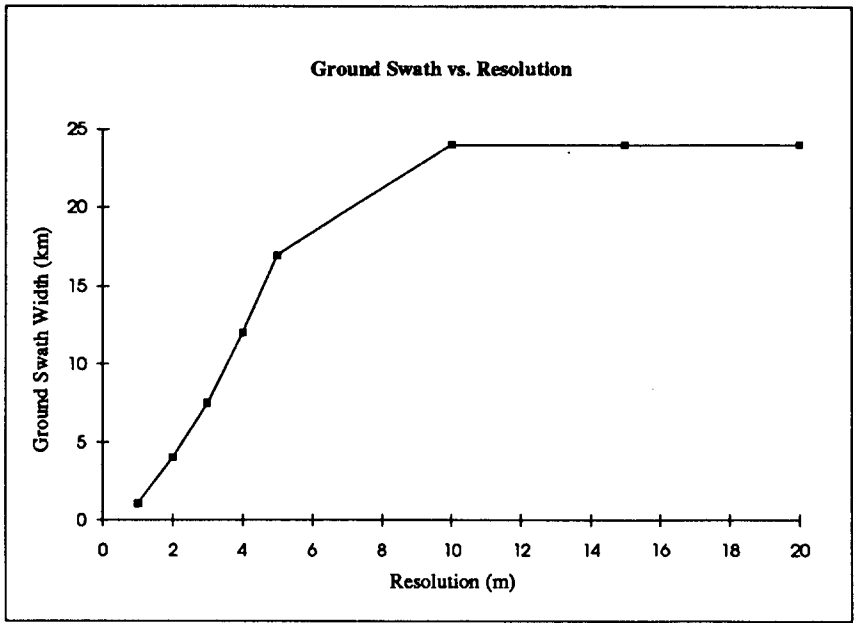

Figure 6.1.1.2: Ground Swath Width vs. Resolution

antenna lengths and widths will be limited by structural and electronic considerations. From Chapter 4 in [47], antenna lengths of up to approximately 450 wavelengths are reasonable with current technology and antennas having lengths up to 600 wavelengths are under development, so the 10 m antenna length (500 wavelengths) is reasonable. The 0.5 m minimum antenna width is maybe somewhat more arbitrary.

Figure 6.1.1.3 is a plot of the estimated raw data rate versus the resolution. Based upon section 4.3, the data rates for 2 m resolution and larger appear to be feasible. For resolutions less than about 1.5 m, something has to be done. There are many options to reduce the data rate. One option is to buffer data at times and drop data at other times (i.e., non-continuous coverage). Another option is to reduce the dynamic range from 5 bits to 2 bits at a price of SNR in the resulting image. Another is to perform on-board image processing at a cost of increased weight and system complexity and loss of flexibility. Yet another option is to reduce the video bandwidth by using deramp processing (see section 5.1.3) and possibly reducing scene size. Certainly a combination of these techniques is also possible.

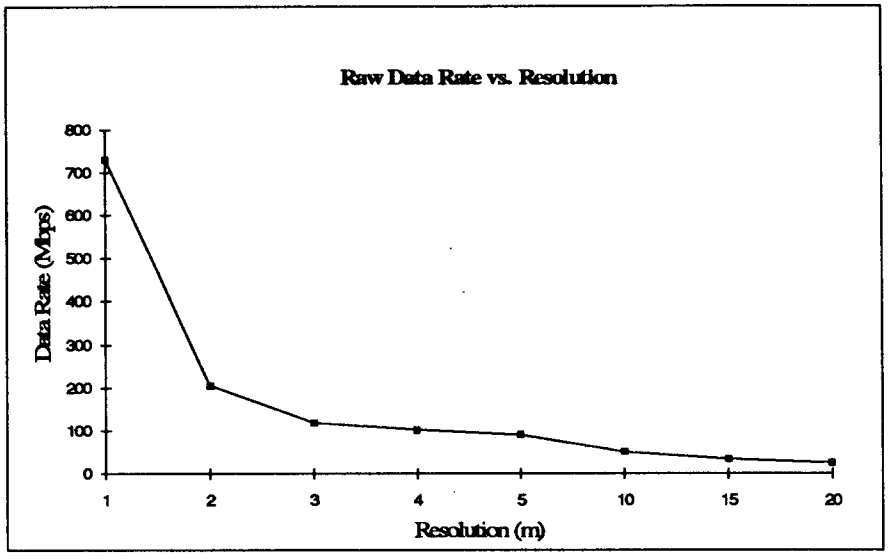

Figure 6.1.1.3: Raw Data Rate vs. Resolution at Ku-band

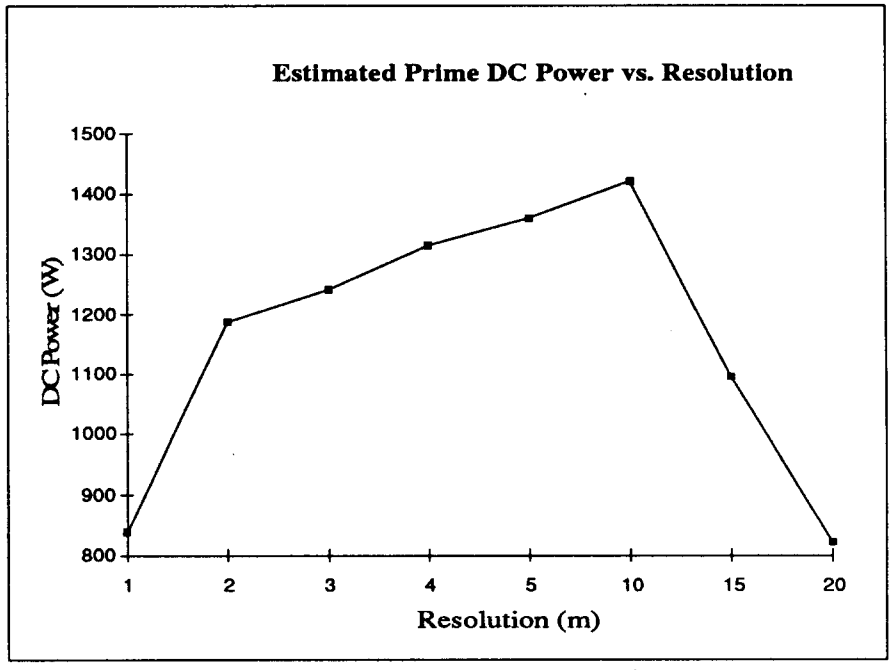

Figure 6.1.1.4: Estimated DC Power vs. Resolution at Ku-Band

Figure 6.1.1.4 is a plot of the estimated prime DC power required for the spaceborne SAR. Obviously, this plot is related to figure 6.1.1.1 due to the assumption made in this study. The apparent dip in power for the 1 m resolution case is due to the fact that PRF considerations are starting to limit the available range swath. This limits the power according to equation (5.4.4.7).

6.1.2 Ku-Band Case Study - Varying Look Angle

The effect of varying the look angle is illustrated in figures 6.1.2.1, 6.1.2.2, 6.1.2.3, and 6.1.2.4. Again, in figure 6.1.2.1, the main influence is the power requirements. Increasing the look angle in turn increases the range. To counteract this, the gain of the antenna must be increased accordingly. This means that the size of the antenna increases and the swath width coverage decreases. The only reason

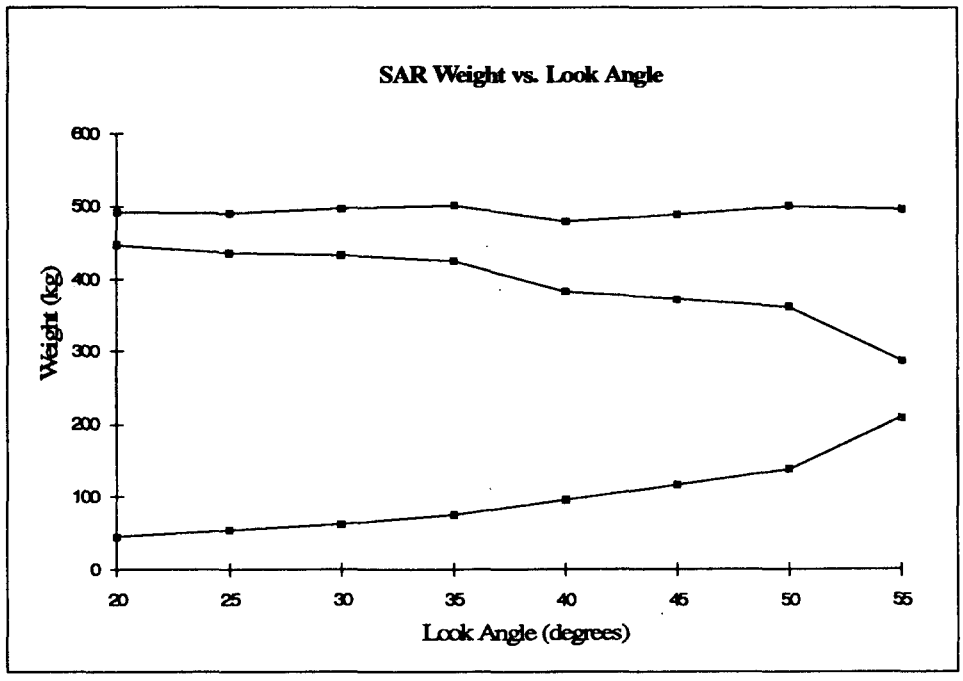

Figure 6.1.2.1: Estimated SAR Weight vs. Look Angle at Ku-Band

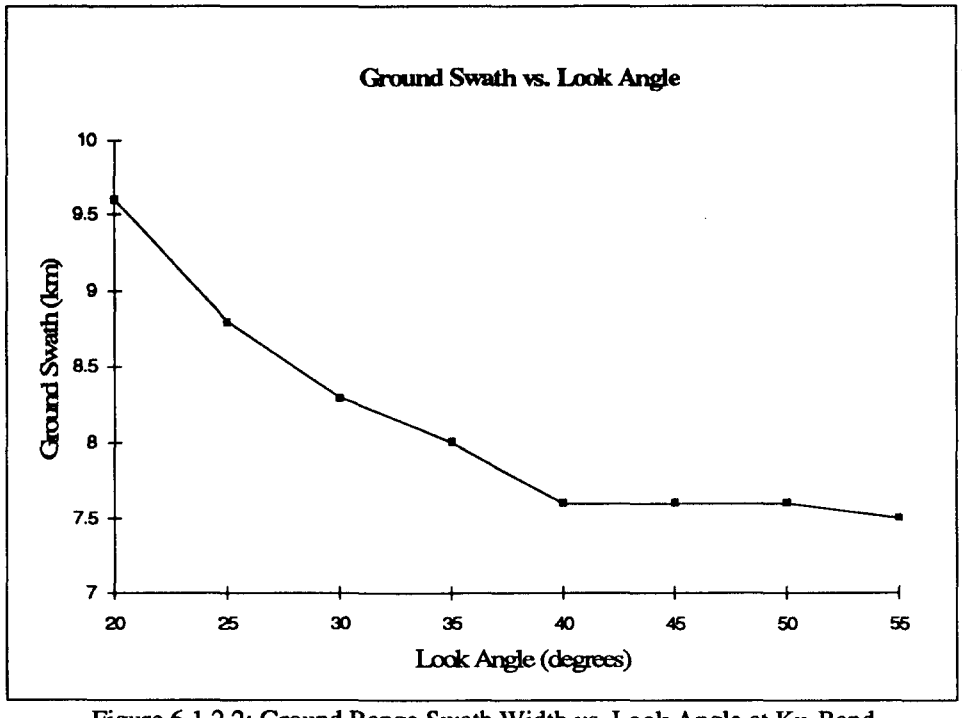

Figure 6.1.2.2: Ground Range Swath Width vs. Look Angle at Ku-Band

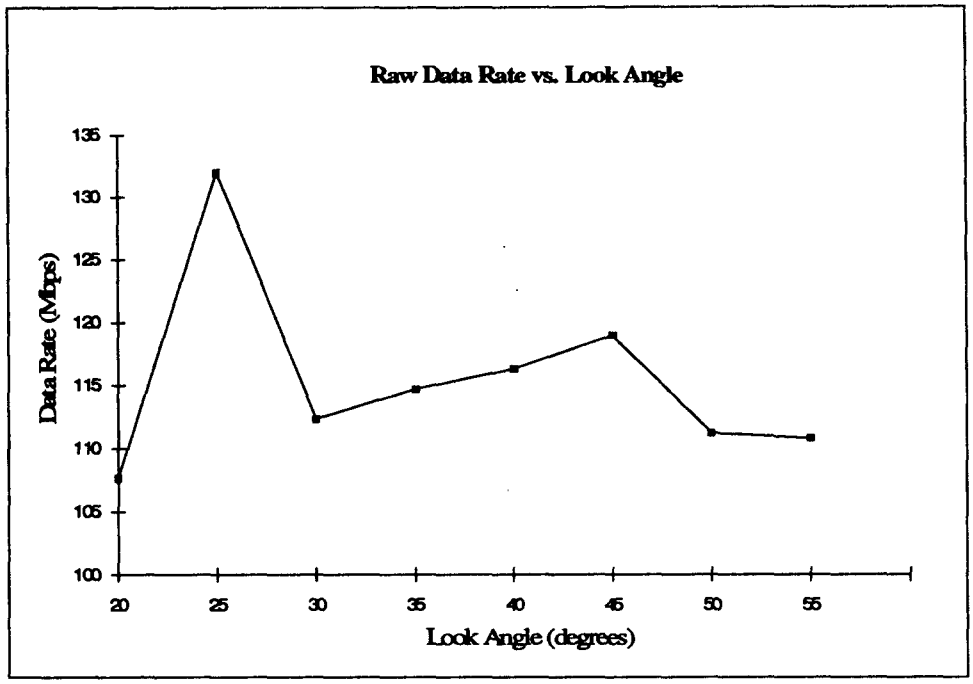

Figure 6.1.2.3: Raw Data Rate vs. Look Angle at Ku-Band

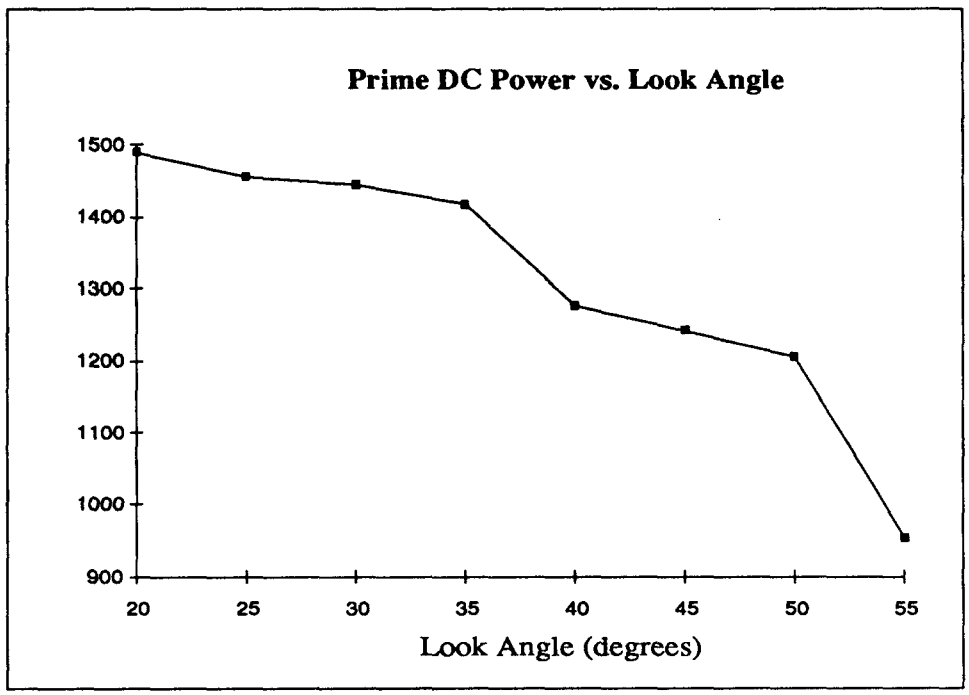

Figure 6.1.2.4: Estimated Prime DC Power vs. Look Angle at Ku-Band

that power is decreasing in figure 6.1.2.4, is that we have tied power directly to weight and have put a ceiling on total weight. Since the weight of the antenna is increasing, the power is forced to decrease.

6.2 P-Band Case Study

The assumption of a 500 kg SAR limit is not reasonable for the P-band case. This is because the estimated weight for the antenna alone at P-band must exceed 500 kg to avoid PRF problems. This

Table 6.2.1: Base System - P-Band

Subject	Item	Units	Value
Orbit:			
	Orbit Inclination	degrees	97.4
	Altitude	km	500
	Satellite Velocity	m/sec	7616
	Ground Track Velocity	m/sec	7039
Scene:			
	Look Angle - mid	degrees	45
	Slant Range Res.	m	10
	Ground Range Res. - near	m	13.5
	Azimuth Res.	m	10
	Swath Width (ground)	km	55
	Swath Width (slant)	km	41.9
	Range - mid	km	737
	Squint Angle to Scene Center	degrees	90
Radar:			
	Frequency	GHz	0.45
	Pulse Width	μs	30
	Bandwidth	MHz	15
Ambiguity Information:			
	Maximum PRF	Hz	1834
	Minimum PRF	Hz	1523
	Actual PRF	Hz	1525
	Yaw Angle/PRF Ambiguity	degrees	2.8
	Pitch Angle/PRF Ambiguity	degrees	2.8
Processing Info:			
	Aperture Length	km	25.3
	Aperture Time	sec	3.3
Target Info:			
	Target type	Point/Distributed	Distributed
	Noise equivalent, σ_n^0	dB	-25
Antenna/Receiver Parameters:			
	Length	m	10
	Azimuth Beamwidth - 3 dB	degrees	3.8
	Width	m	8
	Elevation Beamwidth - 3 dB	degrees	4.8
	Efficiency		0.65
	Receiver Noise Factor	dB	2.8
	System Noise Temperature	degrees Kelvin	290
Power Losses:			
	Total Losses Assumed	dB	9
Tx Power Requirements:			
	Average Txmitter Power - Far Range	W	91
	Peak Txmitter Power - Far Range	W	891
Weight Estimate:			
	Total Weight	kg	891

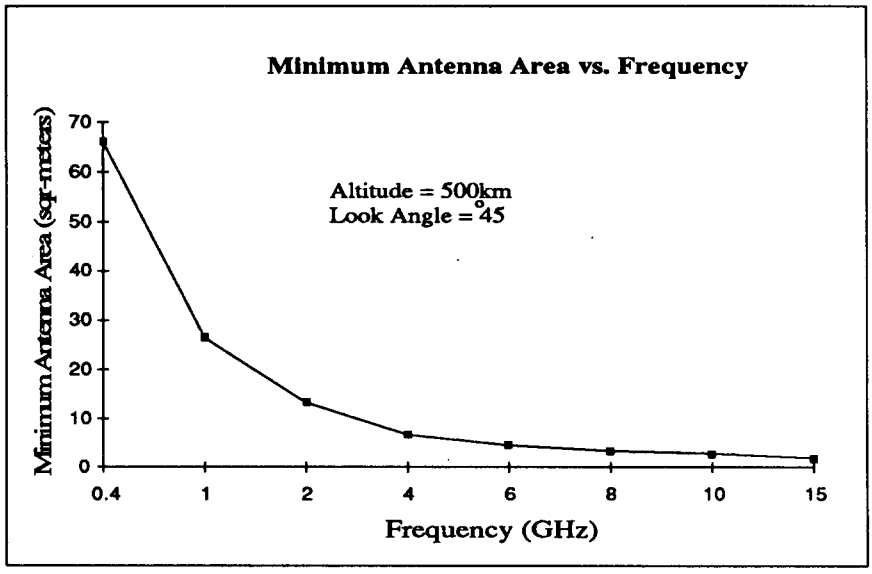

Figure 6.2.1: PRF Limitations - Minimum Antenna Area vs. Frequency

problem can be presented in terms of the minimum antenna area given in equation (5.1.5). Figure 6.2.1 illustrated the problem.

Figure 6.2.1 shows that in order to keep the antenna weight down below about 300 kg (allowing 200 kg for electronics weight) with the assumption of 10 kg/m^2, the frequency must be at least 1 GHz (L-band). Since this is the case, for the P-band study the weight limit is increased to 1000kg. This gives an 4000kg payload putting us into a higher class of launch vehicles. In addition, since the antenna will be larger, folding, storing , and deploying the antenna will be a more difficult mechanical problem. Table 6.2.1 gives the base line design for the P-band study.

6.2.1 P-Band Case Study - Varying Resolution

The affects of varying the resolution for the P-band case are illustrated in figure 6.2.1.1. For this case the antenna size and swath were fixed for all of the resolutions considered.

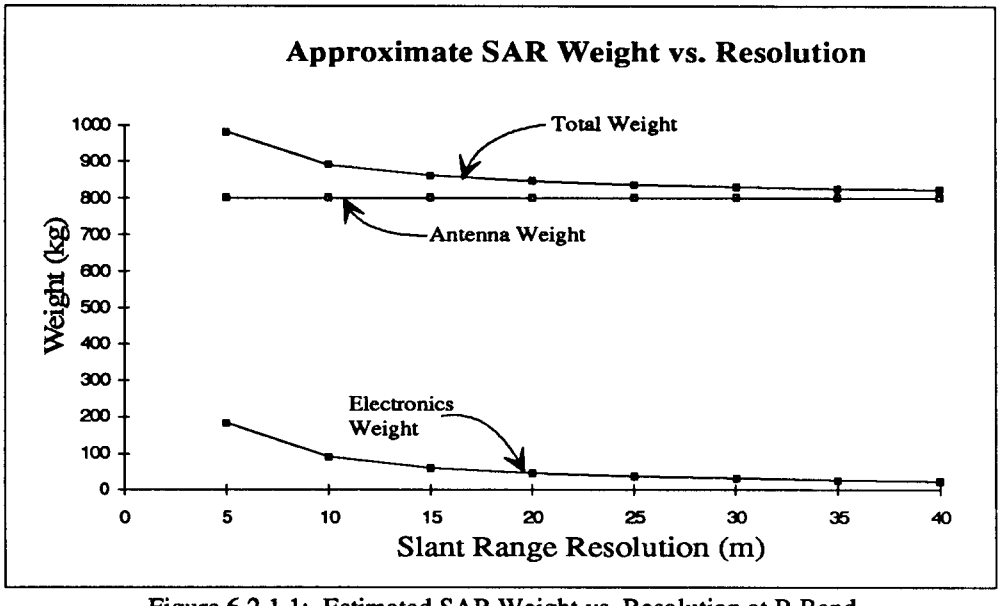

Figure 6.2.1.1: Estimated SAR Weight vs. Resolution at P-Band

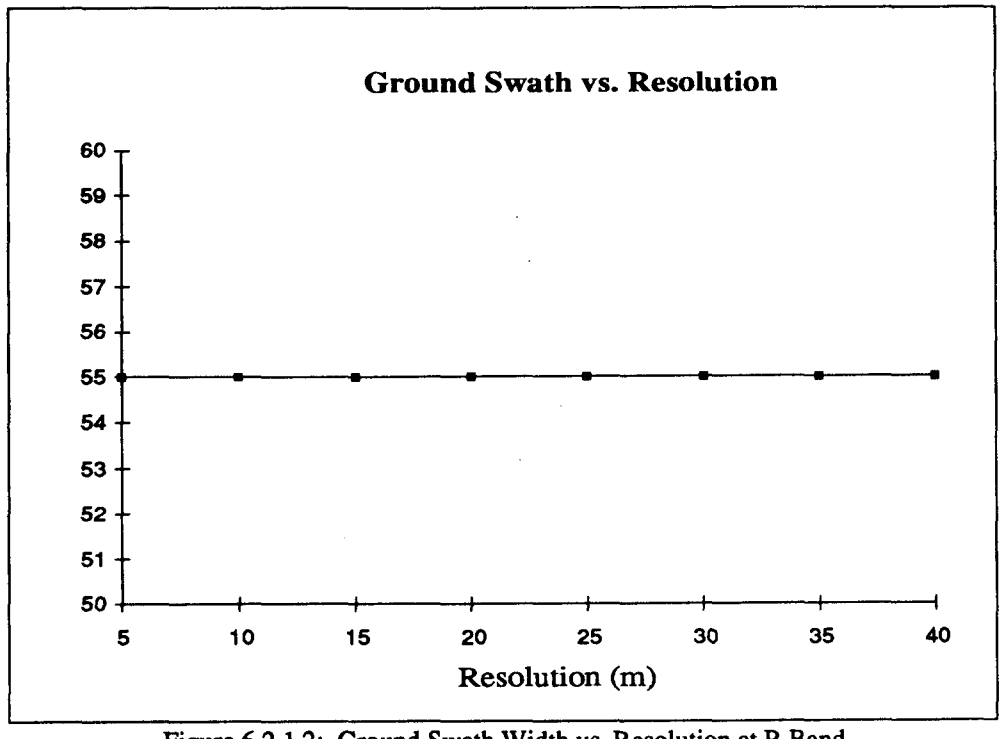

Figure 6.2.1.2: Ground Swath Width vs. Resolution at P-Band

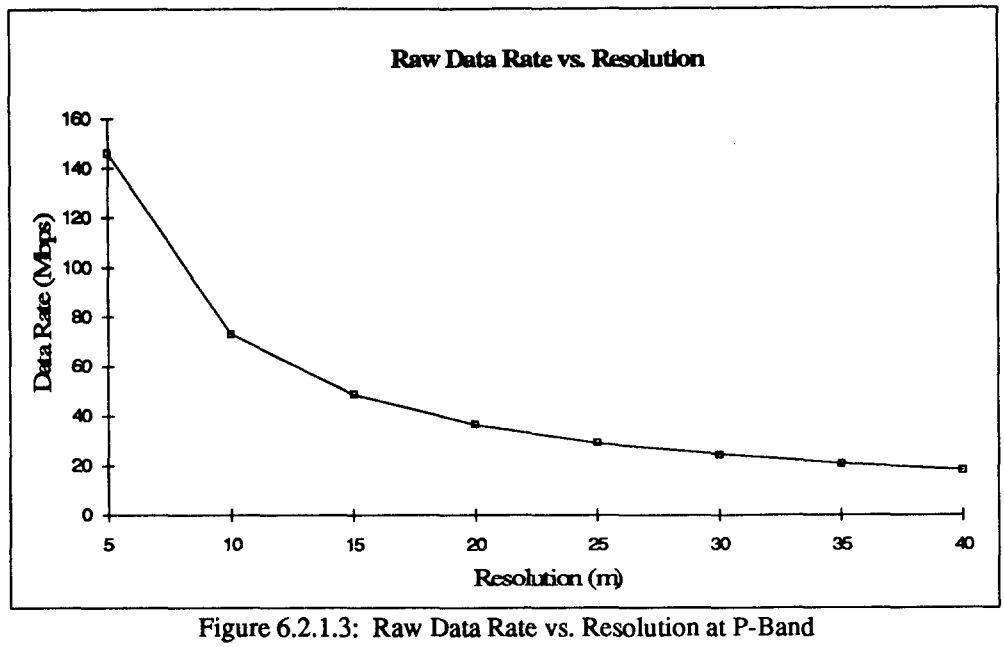

Figure 6.2.1.3: Raw Data Rate vs. Resolution at P-Band

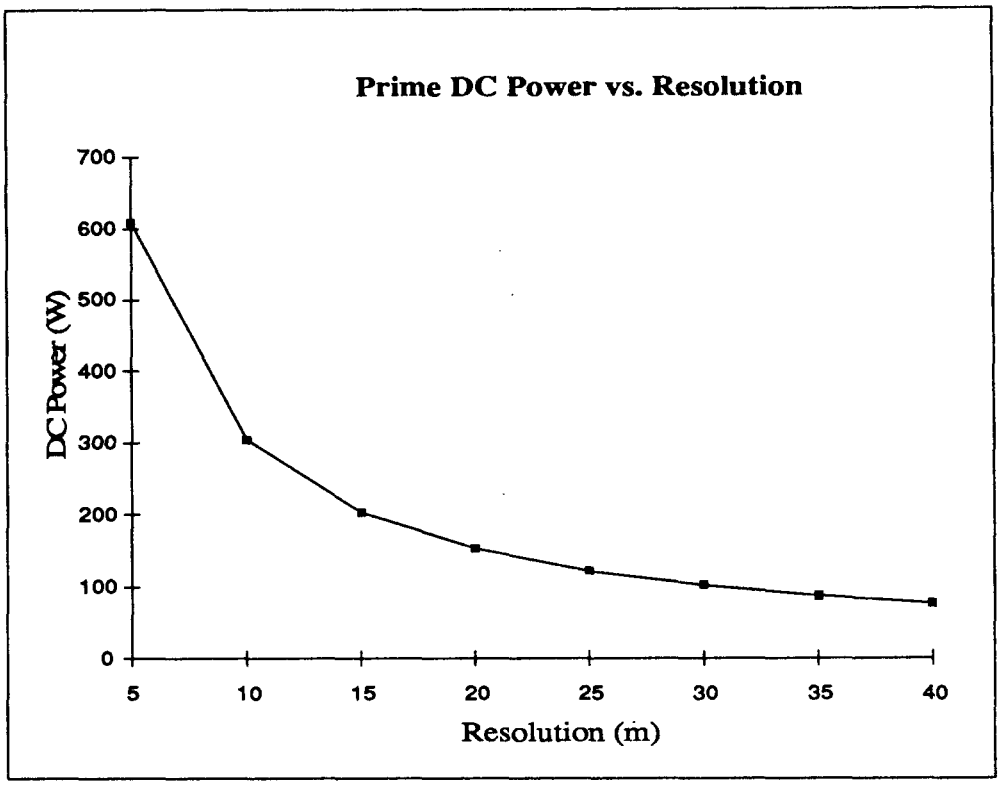

Figure 6.2.1.4: Estimated Prime DC Power vs. Resolution at P-Band

6.2.2 P-Band Case Study - Varying Look Angle

The affects of varying the look angle for the P-band base case are investigated in this section. Figures 6.2.2.1 and 6.2.2.2 show the influence of look angle on the estimated weight and ground swath covered.

Again, in this section, the PRF is a very important issue. For example, the dip that is observed in figure 6.2.2.2 is due to PRF limitations. These same limitations make it necessary to increase the antenna size, and hence the weight in figure 6.2.2.1. Also, no PRFs were available above a look angle of 45° without increasing the antenna size and exceeding the assumed weight limit.

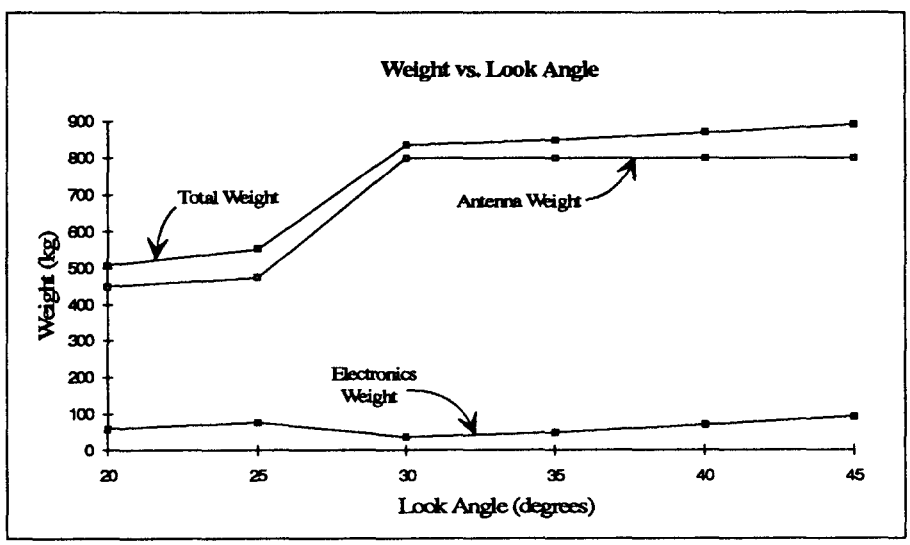

Figure 6.2.2.1: SAR Weight vs. Look Angle at P-Band

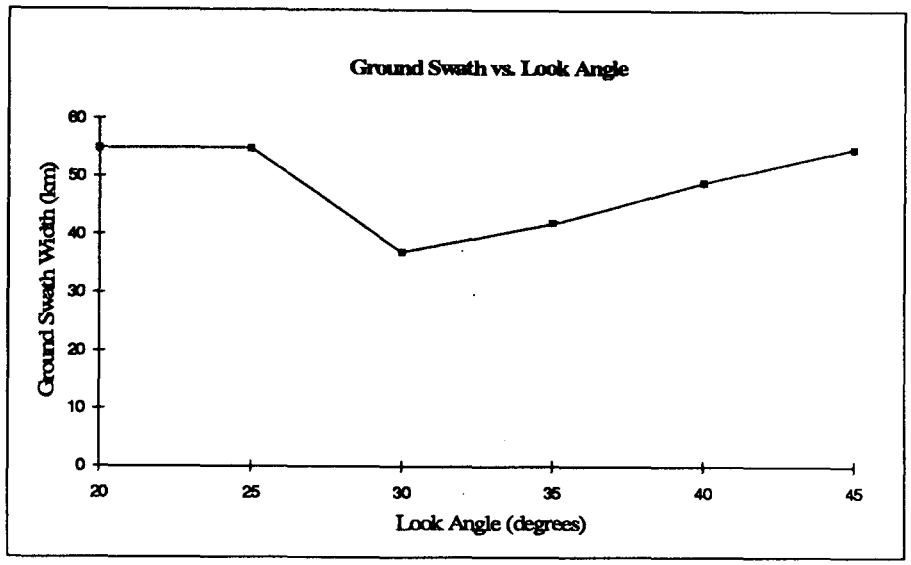

Figure 6.2.2.2: Ground Swath vs. Look Angle at P-Band

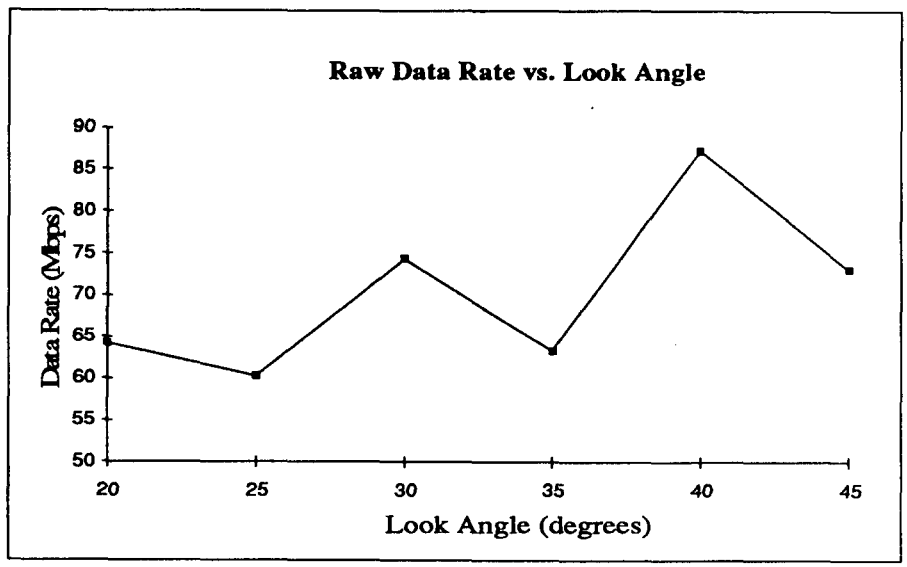

Figure 6.2.2.3: Raw Data Rate vs. Look Angle at P-Band

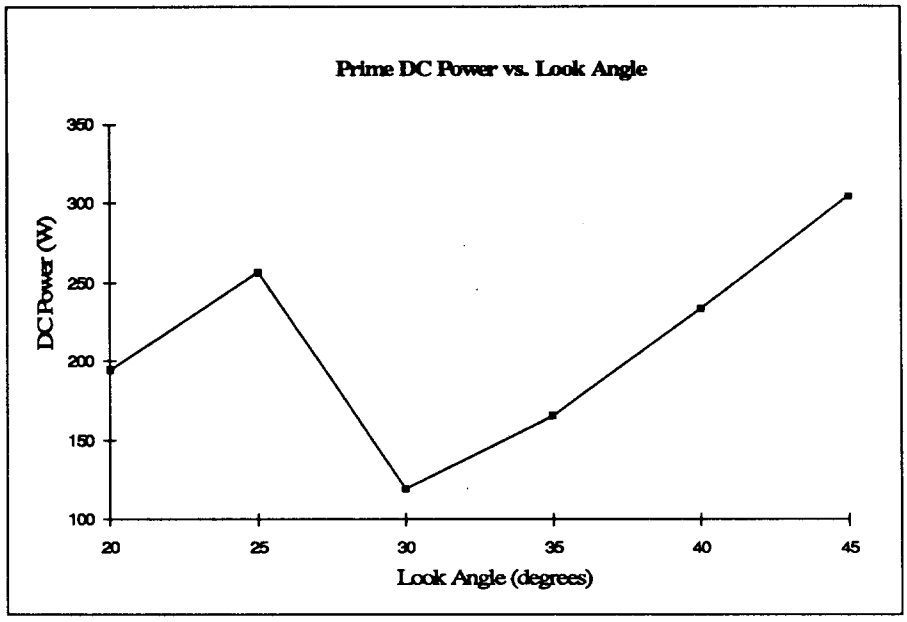

Figure 6.2.2.4: Estimated Prime DC Power vs. Look Angle at P-Band

6.3 Summary of the Case Studies

The two cases presented represent the two extremes of the frequency spectrum for SAR. Comparing figures 6.1.1.1 and 6.2.1.1, it is apparent that power (hence the electronics weight in this model) is the problem for Ku-band. However, the antenna size (PRF constraints) is the problem for P-band. These case studies give some indicaiton why the spaceborne SAR systems in section 4.1 are at frequencies between P-band and Ku-band. They avoid the extremes illustrated in the graphs above.

In summary, the power requirements of the P-band are less for the resolutions that we are talking about and hence, in this study at least, the estimated electronics weights are less. However, for the longer wavelength, the antenna grows too large to maintain available PRFs. The net affect is that antenna size becomes a limiting factor for a P-band satellite SAR. Note that even the techniques for mitigating PRF problems presented in section 5.2 require large antennas. The techniques described in that section are only to permit higher azimuth resolution and larger ground swath coverage.

One thing that is not apparent from the figures above is the problem of the ionosphere for higher resolution (bandwidths of 25 MHz and above) at P-band. This was addressed in section 5.5 and needs to be considered in an actual design.

7.0 Summary

In summary, designing and building a synthetic aperture radar (SAR) for spaceborne application is a much more challenging accomplishment than for airborne application. PRF and power are very important for spaceborne SAR because of the higher platform velocities and longer ranges. These considerations and additional mechanical issues (such as antenna flatness) make the antenna design more critical for spaceborne SAR. Total system weight relates to launch cost. Obviously, high-reliability is essential for spaceborne SAR. The space environment is more difficult due to radiation, SEPs, plasma charging and space particles. Finally, the circular orbit, circular earth, earth motion, and large range swaths must be accounted for in image processing.

8.0 Recommendation for Future Studies

There are many more items which were not investigated in this report. Some of the items that warrant further investigation include:

1) It seems that motion compensation techniques could be used in spaceborne SAR, particularly if on-board image formation is desirable as suggested in [25]. These techniques could remove the effects of earth motion and ellipticity of the orbit to a central reference. Since these effects are predictable, they could be pre-calculated. Also, the motion characteristics of low-earth orbit satellites need to be better understood. Can the motion be predicted and some corrections pre-calculated?

2) Other terms due to the motion of the earth and non-straight-line orbit need to be accounted for in the image formation algorithms. Also, current algorithms need to be investigated for their applicability to spaceborne systems.

3) Calibration is more challenging due to the atmosphere and ionosphere and fluctuations in the antenna pattern caused by the antenna flexing.

4) Techniques for compensating for ionosphere affects for low frequency SARs is another possibly important area of research.

5) Mechanical, electrical (e.g., arcing), and environmental issues, all of which limit technologies that can be used in space, need to be addressed.

6) A more in-depth examination of techniques for obtaining large range swaths and fine azimuth resolution could be performed.

7) The antenna is a critical element of the spaceborne SAR. Antenna issues should be investigated, such as: how is the proper flatness achievable; what T/R modules are available; what configurations are practical from space; and how is calibration maintained?

8) Another potential area to pursue is on-board image processing.

9) Current known spaceborne SARs do not operate in the Ku-band and P-band frequencies because of the challenges mentioned in section 6.0. Overcoming these challenges in a technically feasible manner could be important.

10) Spaceborne SARs (and the components that comprise the system) of the future need to be more compact, lighter, and more flexible in terms of operating configurations and parameters (e.g., frequency, polarization, etc.). These areas should be analyzed, also.

9.0 Bibliography

The following references contributed to the content of this document:

[1] Anonymous, "Controllers Struggle With Radar Antenna on JERS-1 Satellite", *Aviation Week & Space Technology*, Feb. 17, 1992, pp. 21.

[2] E. P. W. Attema, "The Active Microwave Instrument, On-Board the ERS-1 Satellite", *Proceedings of the IEEE*, v. 79, n. 6, 1991, pp. 791-799.

[3] R. Bamler and H. Runge, "A Novel PRF-Ambiguity Resolver", *Proc. of IGARRS '91*, pp. 1035-1038.

[4] R. Bamler and H. Runge, "PRF-Ambiguity Resolving by Wavelength Diversity", *IEEE Trans. on Geoscience and Remote Sensing*, Vol. 29, No. 6, Nov. 1991, pp. 997-1003.

[5] B. C. Barber, "Theory of Digital Imaging from Orbital Synthetic-Aperture Radar", *Int. J. Remote Sensing*, 1985, Vol. 6, No. 7, pp. 1009-1057.

[6] D. L. Bickel, Memo to C. T. Allen titled, "Simplified Equation for Radar Range with Curved Earth", June 16, 1992.

[7] W. Birmingham, B. Miller and W. Stein, "Experimental Results of Using the GPS for Landsat 4 Onboard Navigation", *Global Positioning System*, Vol. II, pp. 231-238.

[8] D. L. Brandel, W. A. Watson, and A. Weinberg, "NASA's Advanced Tracking and Data Relay Satellite System for the Years 2000 and Beyond." *Proceedings of the IEEE*, v. 78, n. 7, July 1990, pp. 1141-1152.

[9] B. C. Brock, *The Frequency Response of Phased-Array Antennas*, SAND88-2667, February 1989.

[10] B. C. Brock, *Polarimetric Calibration of a Coherent Measurement Radar*, SAND91-2150, December 1991.

[11] B. C. Brock, *Ionospheric Effects on a Wide-Bandwidth, Polarimetric, Space-Based, Synthetic-Aperture Radar*, SAND92-1967 UC-706, January, 1993.

[12] W. D. Brown, D. C. Ghiglia, "Some methods for reducing propagation-induced phase errors in coherent imaging systems. I. Formalism", *J. Opt. Soc. Am. A*, Vol. 5, No. 6, June 1988, pp 924-941.

[13] C. Cafforio, C. Prati, E. Rocca, "SAR Data Focusing Using Seismic Migration Techniques", *IEEE Transactions on Aerospace and Electronic Systems*, Vol. 27, No. 2, March 1991, 194-207.

[14] S. J. Campanella and R. K. Garlow, "RF/optical design for optical intersatellite links", *Microwave Journal*, v.34, n. 10, Oct 1991, pp. 85-86, 88, 90, 93-94, 101, 103, 106.

[15] L. J. Cantafio, (editor), *Space-Based Radar Handbook*, Artech House, Norwood, MA., 1989.

[16] M. Cohen, E. Fornoles and T. Mahefkey, "Requirements and Technology Trends for Future Military Space Power Systems", *Proc. of the 16th Intersociety Energy Conversion Engineering Conference*, Aug. 1981, pp. 2122-2125.

[17] J. T. Cordaro, *Range Performance of a Linear-FM Synthetic-Aperture Radar*, SAND87-1863, 1987.

[18] J. T. Cordaro, *Signal-Processor Performance of a Linear-FM Synthetic-Aperture Radar*, SAND88-0931.

[19] J. T. Cordaro, *Description of the Signal-Processing Algorithm for the Strip Radar*, SAND89-3119.

[20] J. T. Cordaro, "SAR Operation Near Nadir", Memorandum dated Dec. 12, 1992, contained in *NAASW Modular Radar Research Testbed Study Results*, SAND91-2495, Vol. 1, Dec. 1991.

[21] J. C. Curlander, and R. N. McDonough, *Synthetic Aperture Radar - Systems and Signal Processing*. John Wiley & Sons, 1991.

[22] A. Currie and C. D. Hall, "A Synthetic Aperture Radar Technique for the Simultaneous Provision of High-Resolution Wide-Swath Coverage", *Proceedings Military Microwaves '90*, Microwave Exhibitions and Publishers Ltd, July 1990, pp. 539-544.

[23] A. Currie, "Synthetic Aperture Radar", *Electronics & Communication Engineering Journal*, v. 3, August 1991, pp. 159-170.

[24] A. Currie and M. Brown, "Wide-Swath SAR", *IEE Proceedings-F*, Vol. 139, No. 2, April 1992, pp. 122-135.

[25] P. H. Eichel, D. C. Ghiglia, C. V. Jakowatz, Jr., "Speckle Processing Method for Synthetic-Aperture-Radar Phase Correction", *Optics Letters*, Vol. 14, No. 1, January 1, 1989, pp 1-3.

[26] C. Elachi, *Spaceborne Radar Remote Sensing: Applications and Techniques*. IEEE Press, 1988.

[27] P. R. Escobal, *Methods of Orbit Determination*, Wiley, 1965.

[28] J. Fischer, "Optical Data Communication for Earth Observation Satellite Systems", *Proceedings of the Second European Conference on Satellite Communications*, ECSC-2 (ESA Sp-332) 1991, pp. 405-415.

[29] D. H. Ghiglia and G. A. Mastin, "Two-Dimensional Phase Correction of Synthetic Aperture Radar Imagery", *Optics Letters*, Vol. 14, No. 20, October 15, 1989.

[30] C. M. Hart, "FY92 LDRD Proposed Work - Spaceborne SAR", 1991.

[31] R. C. Haymes, *Introduction to Space Systems*, Wiley, 1971.

[32] B. L. Honeycutt, "Spaceborne Imaging Radar-C Instrument", *IEEE Transactions on Geoscience and Remote Sensing*, v. 27, n. 2, March 1989, pp. 164-169.

[33] C. V. Jakowatz, Jr., P. H. Eichel, D. C. Ghiglia, "Autofocus of SAR imagery degraded by ionospheric-induced phase errors", presented *SPIE*, March 27, 1989 Orlando, FL.

[34] W. T. K. Johnson, "Magellan Imaging Radar Mission to Venus", *Proceedings of the IEEE*, Vol. 79, No. 6, June, 1991, pp. 777-790.

[35] R. L. Jordan, "Synthetic Array Radars in Space", *WESCON 1980 Conference Record*,1980, pp. 1-8.

[36] [JOR80b] *ineering*, v. OE-5, no. 2, April 1980, pp.154-164.

[37] R. L. Jordan, B. L. Honeycutt and M. Werner, "The SIR-C/X-SAR Synthetic Aperture Radar System", *Proceedings of the IEEE*, v. 79, n. 6, 1991, pp. 827-838.

[38] P. Jorgensen, "Navigating Low Altitude Satellites Using the Current Four NAVSTAR/GPS Satellites", *Global Positioning System*, Vol. II, 1983, pp. 112-121.

[39] JPL SAR Class Notes, 1991.

[40] H. Kashihara, K. Tanaka, M. Fukai, etal., "A Case Study of Space-Borne Synthetic Aperture Radar System Design for the Earth Resources Satellite", *Proc. of IGARRS '84*, Aug. 1984, pp. 815-820.

[41] R. S. Lawrence, C. G. Little, H. J. A. Chivers, "A Survey of Ionospheric Effects Upon Earth-Space Radio Propagation", *Proceedings of the IEEE*, Vol. 52, January 1964, pp 4-27.

[42] F. K. Li and W. T. K. Johnson, "Ambiguities in Spaceborne Synthetic Aperture Radar Systems", *IEEE Trans. Aerospace and Electronic Systems*, Vol. AES-19, No. 3, May 1983, pp. 389-396.

[43] F. Li, D. Held, J. Curlander and C. Wu, "Doppler Parameter Estimation for Spaceborne Synthetic-Aperture Radars", *IEEE Trans. on Geoscience and Remote Sensing*, Vol. GE-23, No. 1, Jan. 1985, pp. 47-56.

[44] F. K. Li. and R. K. Raney, "The Special Section on Spaceborne Radars for Earth and Planetary Observations", *Proceedings of the IEEE*, v. 79, n. 6, 1991, pp. 773-776.

[45] J. V. Lincoln, *International Reference Ionosphere: IRI 79, (Upper Atmosphere Geophysics Report 82)*, World Data Center, Boulder, Colorado, 1981.

[46] Y. T. Lo, S. W. Lee, *Antenna Handbook, Theory Applications, and Design*, Van Nostrand Reinhold Co., New York, 1988.

[47] S. W. McCandless, Jr., "SAR in Space - The Theory, Design, Engineering and Application of a Space-Based SAR System", in *Space-Based Radar Handbook*. L. J. Cantafio (editor), Artech House, 1989.

[48] S. W. McCandless, "Worldwide Remote-Sensing Analysis Program (WRAP)", User Systems Inc., 1992.

[49] E. Meier, C. Graf and D. Nuesch, "Generation of Geocoded Spaceborne SAR Image Products", *Proc. of IGARSS '89*, 1989, pp. 2473-2477.

[50] Y. Nemoto, H. Nishino, M. Ono, H. Mizutamari, K. Nishikawa and K. Tanaka, "Japanese Earth Resources Satellite-1 Synthetic Aperture Radar", *Proceedings of the IEEE*, v. 79, n. 6, 1991, pp. 800-809.

[51] T. Pratt and C. Bostian, *Satellite Communications*, John Wiley & Sons, 1986.

[52] S. Quegan, J. Lamont, "Atmospheric Effects on SAR Performance", *Int. J. Remote Sensing*, Vol. 7, No. 4, 1986, pp 525-539.

[53] R. K. Raney, "Conceptual Design of Satellite SAR", *Proceedings of IGARSS '84*, August 1984, pp. 801-807.

[54] R. K. Raney, "Doppler properties of radars in circular orbits", *Int. J. Remote Sensing*, 1986, Vol. 7, No. 9, pp. 1153-1162.

[55] R. K. Raney, "SNR Considerations for an Orbital SAR", *Proceedings of IGARSS '90*, 1990, pg. 1125.

[56] R. K. Raney, A. P. Luscombe, E. J. Langham and S. Amhed, "RADARSAT", *Proceedings of the IEEE*, v. 79, n. 6, 1991, pp. 839-849.

[57] H. Runge, "Benefits of Antenna Yaw Steering for SAR", *Proc. of IGARSS '91*, 1991, pp. 257-261.

[58] M. I. Skolnik, *Radar Handbook*, McGraw-Hill, New York, 1970.

[59] *Sky & Telescope*, Vol. 73 through Vol. 81, No. 1-6 (1987-1991), Vol. 82, No. 1-4, 1992.

[60] G. W. Stimson, *Introduction to Airborne Radar*, Hughes Aircraft Company, 1983.

[61] W. T. Thomson, *Introduction to Space Dynamics*, Wiley, 1963.

[62] T. W. Thompson and A. Lederman, "SEASAT-A Synthetic Aperture Radar: Radar System Implementation", *Oceans '76 Conference, IEEE*, Washington D. C., 1976.

[63] F. T. Ulaby, R. K. Moore and A. K. Fung, *Microwave Remote Sensing - Active and Passive, Vol. II.* Artech House Inc., 1986.

[64] F. T. Ulaby, R. K. Moore and A. K. Fung, *Microwave Remote Sensing - Active and Passive, Vol. III.* Artech House Inc., 1986.

[65] J. L. Walker, "Range-Doppler Imaging of Rotating Objects", *IEEE Trans. on Aerospace and Electronic Systems*, Vol AES-16, No. 1, Jan. 1980.

[66] J. Way and E. A. Smith, "The Evolution of Synthetic Aperture Radar Systems and Their Progression to the EOS SAR", *IEEE Trans. on Geoscience and Remote Sensing*, v. 29, no. 6, 1991, pp. 962-985.

[67] J. Wertz and W. Larson (editors), *Space Mission Analysis and Design*, Kluwer Academic Publishers, 1991.

[68] T. Yunck, W. Melbourne and C. Thornton, "GPS-Based Satellite Tracking System for Precise Positioning", *IEEE Trans. on Geoscience and Remote Sensing*, Vol. GE-23, No. 4, July 1985, pp. 450-457.

Appendix A: Space Geometry and Orbital Issues

This Appendix gives a simplified description of the geometry from space and orbital mechanics. This section is by no means complete. It is intended as an introduction for those who are more familiar with airborne SAR. More complete discussions can be found in [61], [31], [27]. A good overview can be found in Chapter 2 of [15]. For spaceborne SAR, Appendix B of [21] provides a very good reference. We will make the simplified assumption that the earth is a sphere and that the satellite trajectory is a circle.

The important result from orbital mechanics for the case of a circular satellite trajectory, is that the velocity of the satellite is related to the altitude by:

$$V_{st} = \sqrt{\frac{G}{h + R_e}} \tag{A.1}$$

where:

V_{st} - is the satellite velocity
G - is the gravitational constant, $\cong 3.986 \times 10^5$ km^3/sec^2.
h - is the altitude
R_e - is the radius of the earth

The coordinate system used in this appendix is the equatorial inertial coordinate system (same as [21] - it's similar to the earth-centered inertial system). The important features of this coordinate system are that the origin is located at the center of the earth, the equator lies in the x-y plane, and that the x-axis points to a fixed point in space (i.e., the first point in Aries). Figure A.1 illustrates the geometry.

From Figures A.1 and A.2 the following definitions are given (see also [21], [54]):

Ascending node - the location where the satellite passes directly over the equator (cuts through the x-y plane) in passing from the lower to upper hemisphere (ascending)
R - the range from the antenna to the target on the earth
R_s - the distance from the satellite (antenna) to the center of the earth
R_e - the radius of the earth
Ω - the longitude of the ascending node
ψ - the inclination angle (angle from the x-y plane to the orbit plane)
β - the argument of the latitude
l - is the latitude of the target on the earth
a - the yaw angle (squint angle)
γ - is the look or nadir angle
α - is the (earth) interior angle, from the satellite to the target on the earth

The earth is really an oblate sphere. This causes a pertubation in the satellite's orbit. In other words, the longitude of the ascending node changes. This is called "precession" or "regression" depending upon the direction of rotation. This pertubation can be taken advantage of to permit the sun synchronous orbit. The sun-synchronous orbit is a near-polar orbit (for low-earth orbit satellites) which maintains an almost fixed angle of the orbit plane with respect to the sun. An important special case of the sun-synchronous

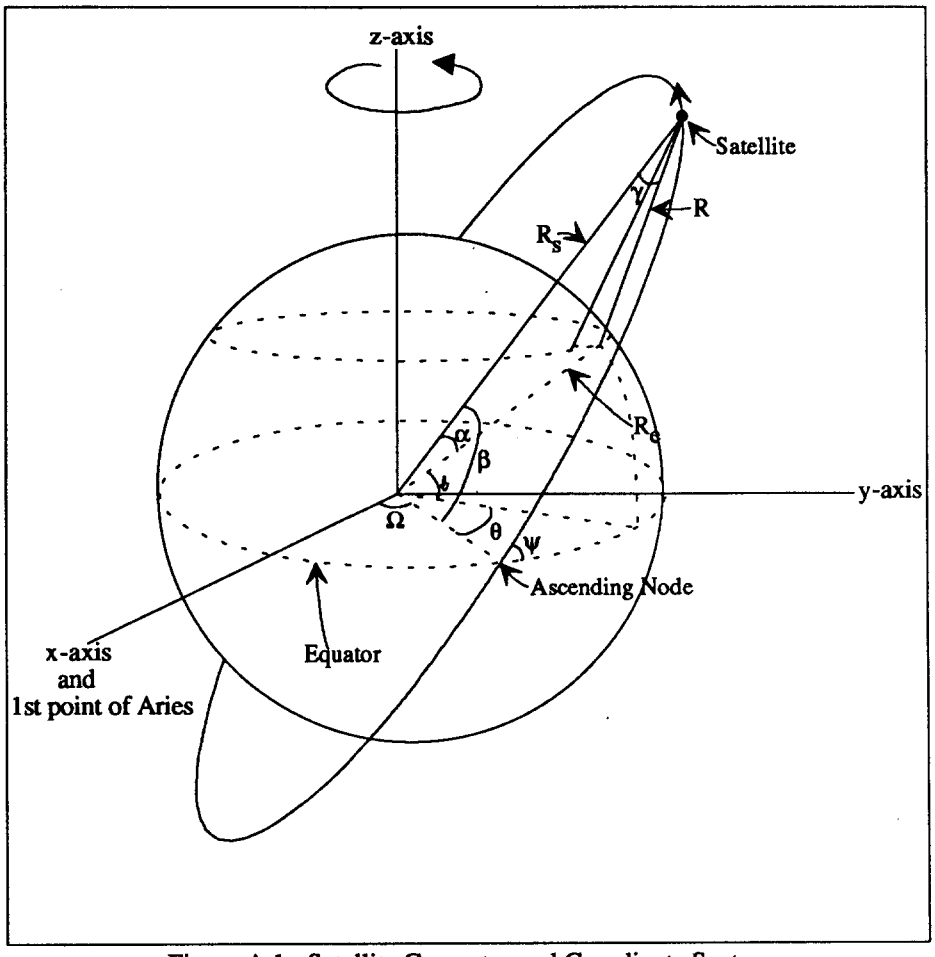

Figure A.1: Satellite Geometry and Coordinate System

orbit permits the solar-panels to be constantly facing the sun. The equation for the inclination of such an orbit is given as:

$$\psi_{sunsynch} = \cos^{-1}\left[0.0989 \cdot \left(\frac{R_e}{R_e + h}\right)^{-3.5}\right] \tag{A.2}$$

For a circular orbit at an altitude of approximately 500km, this gives $\psi_{sunsynch} \cong 97.4°$.

An interesting aside concerning the oblate earth is that SEASAT was flown at a slightly elliptical orbit to try to account for the oblateness of the earth. In other words, the ellipticity of the SEASAT orbit was purposely chosen to try to maintain a constant altitude to a first order [5].

A few important trigonometric relationships are presented here concerning the range to a target and the target location. The first involves the incidence angle, θ_i, the altitude, h, and the earth radius, R_e, [53]:

$$R = R_e \cdot \left[\sqrt{\left(\frac{h}{R_e}\right)^2 + 2 \cdot \left(\frac{h}{R_e}\right) + \cos^2(\theta_i)} - \cos(\theta_i)\right] \tag{A.3}$$

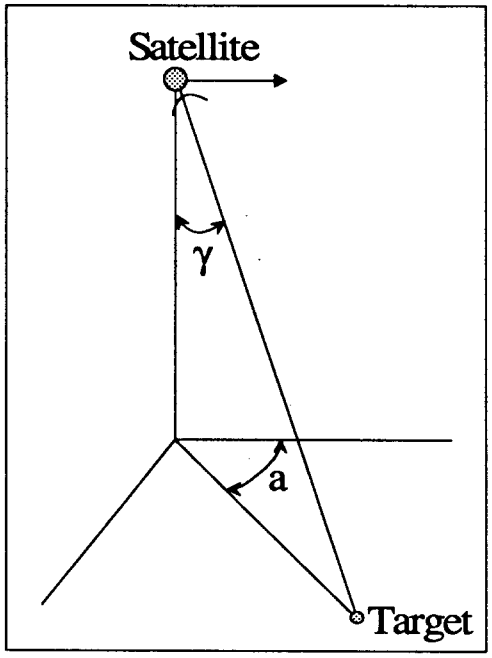

Figure A.2: Radar Beam Geometry

The second involves the look (nadir) angle, γ, radius of the satellite to the center of the earth, R_S, and the earth radius, R_e, [6]:

$$R = R_s \cdot \left[\cos(\gamma) - \sqrt{\cos^2(\gamma) - 1 + \left(\frac{R_e}{R_s}\right)^2} \right] \tag{A.4}$$

In addition, the latitude and longitude (actually, the angle from the x-axis as defined in Figure A.1) of the target can be found from the following equations:

$$\sin(\ell) = \frac{R_s \cdot \sin(\beta) \cdot \sin(\psi)}{R_e} - \frac{R \cdot \left[\cos(\beta) \cdot \sin(\psi) \cdot \cos(a) \cdot \sin(\gamma) + \sin(\beta) \cdot \sin(\psi) \cdot \cos(\gamma) + \cos(\psi) \cdot \sin(a) \cdot \sin(\gamma)\right]}{R_e} \tag{A.5}$$

and

$$\cos(\Omega + \theta) = \frac{R_s \cdot \cos(\beta) - R \cdot \left[\sin(\beta) \cdot \cos(a) \cdot \sin(\gamma) + \cos(\beta) \cdot \cos(\gamma)\right]}{R_e \cdot \cos(\ell)} \tag{A.6}$$

Figure A.3 is exaggerated to illustrate the relationship between the depression, grazing, incidence, and look angles.

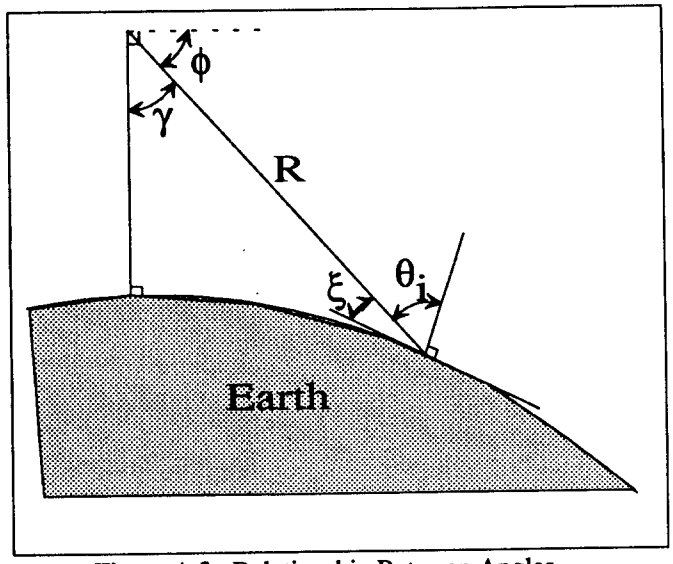

Figure A.3: Relationship Between Angles

From Figure A.3 the angles are defined as:

- γ - is the look or nadir angle
- ξ - is the grazing angle
- θ_i - is the incidence angle
- ϕ - is the depression angle

Figure A.4 shows the relationship between these angles for a satellite at 500 km altitude.

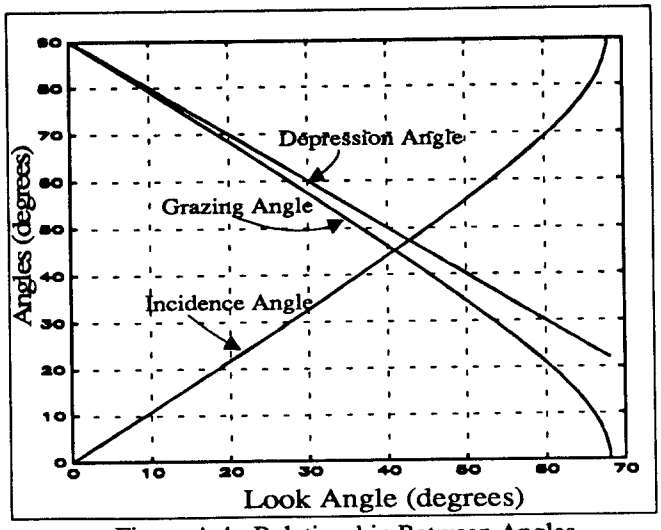

Figure A.4: Relationship Between Angles

Appendix B: Table of Symbols

This appendix presents the symbols used in this report:

A_e	the effective area of the antenna
A	the actual area of the antenna
a	the yaw angle or squint angle (from the spacecraft velocity vector to the target on the ground)
a_{equiv}	the squint angle from an airborne SAR which would yield the same Doppler as the spaceborne SAR
a_0	the yaw (squint) angle to zero Doppler
B_n	the noise bandwidth
BW	the operating bandwidth of the antenna array
BW_{Dop}	the Doppler bandwidth covered by the antenna beam
BW_{DR}	the transmitter bandwidth after deramping the signal
BW_{MF}	the transmitted signal bandwidth (also, the processing bandwidth for matched filter range processing)
c	the speed of light
D_a	the azimuth dimension of the antenna
D_r	the range (elevation) dimension of the antenna
d	the distance between displaced phase centers
d	the element spacing along the antenna array (section 5.6)
dA	the differential element of area of the target (or scene on the ground)
e_a	the efficiency of the antenna, the ratio of incident power on antenna to power transfered to the receiver
F	the noise factor to account for receiver noise
f_c	the Doppler frequency of the center of the image
f_c	the center frequency of the radar (section 5.6)
f_{Dop}	Doppler frequency or required maximum Doppler frequency
$\dot{f}_{Dop}$	the Doppler rate (derivative of the Doppler with respect to time)
G	the gravitational constant, $\equiv 3.986 \times 10^5$ km^3/sec^2.
G	the antenna gain on transmission/reception (section 5.4)
G_T	the antenna gain on transmission
ΔG	the quantization loss due to phase shifters used in the antenna array
h	the altitude of the satellite
k	Boltzman's constant
k	wavenumber (section 5.5)
L_{atmos}	the two-way atmospheric and ionospheric loss
L_{Beam}	the loss due to the fact that the antenna gain is not constant over the beamwidth
L_a	the length of the synthesized aperture
L_{rx}	the receiver line losses
L_{sp}	the signal processor loss
L_{tot}	the total power loss
L_{tx}	the transmitter line losses
l	latitude of the target on the earth

N	the noise power
N	the number of elements along the antenna array (section 5.5)
N_A	the number of subarrays along the antenna beam scan direction
N_a	the number of azimuth samples processed for an aperture
N_B	the number of beams/phase centers in a multi-beam/multi-phase-center antenna
N_p	the presum integer
N_R	the number of range samples processed
P_a	the azimuth patch size of the image formed
P_{avg}	the average power transmitted
P_R	the power at the receiver
P_t	the peak power transmitted
PRF	the pulse-repetition frequency
PRF_{max}	the maximum pulse-repetition frequency
PRF_{min}	the minimum pulse-repetition frequency
p	the number of bits used in the phase shifter for the antenna array
R	the range from the antenna to the target on the earth
R_e	the radius of the earth
R_f	the far range
R_n	the near range
R_s	the distance from the satellite (antenna) to the center of the earth
r	the length of the period of the phase ripple caused by phase-quantization in the antenna array
SNR_I	the SNR including the coherent gain
s	the length of the transmission line between antenna elements
T_a	the aperture integration time
T_{ap}	the aperture dwell time using the full azimuth beamwidth of the antenna
T_F	the A/D sample spacing for Nyquist-rate sampling
T_s	the source equivalent noise temperature
V_g	the footprint velocity of the spaceborne SAR antenna beam
V_{st}	the satellite velocity
V_x	the radar velocity
W_{gr}	the ground range swath width
W_r	the slant range-swath width
α	the (earth) interior angle, from the satellite nadir to the target on the earth
α	the antenna mainlobe amplitude change (section 5.6)
α_f	the interior angle from satellite nadir to the far edge of the swath
α_m	the interior angle from satellite nadir to the midpoint of the range-swath
α_n	the interior angle from satellite nadir to the near edge of the swath
α_n	the series expansion coefficient for the wavenumber (section 5.5)
α_s	the interior angle from the near edge of the swath to the far edge of the swath
β	the argument of the latitude (see Appendix A on orbit and coordinate systems)
β_{az}	3-dB azimuth beamwidth of the antenna
γ	the look or nadir angle (elevation angle at the satellite from nadir to the target on earth)

γ_r	the chirp rate of the radar
ε	is -1 if the radar is looking out the left side of the satellite (from velocity vector), otherwise 1
ε_y	the satellite yaw angle error
ε_p	the satellite pitch angle error
λ	the radar wavelength
λ_g	the antenna transmission line wavelength
λ_{gm}	the antenna transmission line wavelength when the antenna points to broadside
θ	the angle along broadside to which the beam is steered (scan angle)
θ_g	the scan angle at which grating lobes appear
θ_i	the incidence angle
θ_{max}	the maximum scan angle
θ_q	the scan angle to phase-quantization lobes
ρ_a	the azimuth resolution
ρ_{rg}	the ground range resolution
σ	the radar cross-section (RCS) of the target
σ^o	the normalized radar cross-section
$\sigma_n{}^o$	the noise equivalent normalized radar cross-section
τ_D	the two-way propagation delay from the antenna to a target on earth and back
τ_{far}	the time it takes the transmitted pulse to travel to the far edge of the beam and return
τ_I	the integration time for processing a signal in range
τ_n	the time that noise only is integrated into the signal processed in range
τ_{nadir}	the time it takes the transmitted pulse to travel to the nearest point on earth (directly below the satellite) and return
τ_{near}	the time it takes the transmitted pulse to travel to the near edge of the beam and return
τ_p	the pulse length
τ_w	the swath time
ϕ	the depression angle
Ω	the longitude of the ascending node
ν	the surface-wave velocity along the antenna array
ξ	the grazing angle
ψ	the orbit inclination angle (angle from the equatorial plane to the orbit plane - refer to Appendix A)
ω_e	the angular rotation rate of the earth
ω	the angular rotation rate of the satellite
ω	the radar frequency in radians per second (section 5.5)
ω_0	the radar center frequency in radians per second
$\Delta\omega$	the radar bandwidth in radians per second

DISTRIBUTION:

2300	R. D. Andreas
2343	W. H. Schaedla
2343	B. C. Brock
2344	R. M. Axline
2344	J. T. Cordaro
2344	G. K. Froehlich
2344	W. H. Hensley
2344	D. A. Jelinek
2344	J. J. Mason
2344	R. C. Ormesher
2345	B. C. Walker
2345	T. P. Bielek
2345	B. L. Burns
2345	A. W. Doerry
2345	D. F. Dubbert
2345	R. T. Knudson
2345	B. L. Remund
5802	M. W. Callahan
5900	C. W. Childers
5909	R. E. Spalding
5912	C. V. Jakowatz
5912	P. H. Eichel
5912	P. A. Thompson
7141	Technical Library (5)
7151	Technical Publications
7613-2	Document Processing for DOE/OSTI (10)
8523-2	Central Technical Files
9100	C. M. Hart
9102	L. D. Hostetler
9102	M. L. Heinrich
9131	J. R. Fellerhoff
9132	A. C. Watts
9134	D. H. Cress
9135	L. T. James
9203	G. H. Mauth
9204	L. S. Walker
9205	D. A. Reynolds
9211	T. G. Taylor
9225	C. A. Boye
KCD	C. T. Allen, D/852
2344	D. L. Bickel (10)